IS-T 1800

Laser: a tol for optimization and enhancement of analytical methods

by

Preisler, Jan

PHD Thesis submitted to Iowa State University

Ames Laboratory, U.S. DOE

Iowa State University

Ames, Iowa 50011

Date Transmitted: January 10, 1997

PREPARED FOR THE U.S. DEPARTMENT OF ENERGY

UNDER CONTRACT NO. W-7405-Eng-82.

DISCLAIMER

AVAILABILITY:

To DOE and DOE contractors: Office of Scientific and Technical Information
P.O. Box 62
Oak Ridge, TN 37831

prices available from: (615) 576-8401
FTS: 626-8401

To the public: National Technical Information Service
U.S. Department of Commerce
5285 Port Royal Road
Springfield, VA 22161

To my parents

TABLE OF CONTENTS

ABSTRACT

In this work, we use lasers to enhance possibilities of laser desorption methods and to optimize coating procedure for capillary electrophoresis (CE). We use several different instrumental arrangements to characterize matrix-assisted laser desorption (MALD) at atmospheric pressure and in vacuum. In imaging mode, 488-nm argon-ion laser beam is deflected by two acousto-optic deflectors to scan plumes desorbed at atmospheric pressure via absorption. All absorbing species, including neutral molecules, are monitored. Interesting features, e.g. differences between the initial plume and subsequent plumes desorbed from the same spot, or the formation of two plumes from one laser shot are observed. Total plume absorbance can be correlated with the acoustic signal generated by the desorption event. A model equation for the plume velocity as a function of time is proposed. Alternatively, the use of a static laser beam for observation enables reliable determination of plume velocities even when they are very high. Static scattering detection reveals negative influence of particle spallation on MS signal. Ion formation during MALDI was monitored using 193-nm light to photodissociate a portion of insulin ion plume. These results define the optimal conditions for desorbing analytes from matrices, as opposed to achieving a compromise between efficient desorption and efficient ionization as is practiced in mass spectrometry.

In CE experiment, we examined changes in a poly(ethylene oxide) (PEO) coating by continuously monitoring the electroosmotic flow (EOF) in a fused-silica capillary during electrophoresis. An imaging CCD camera was used to follow the motion of a fluorescent neutral marker zone along the length of the capillary excited by 488-nm Ar-ion laser. The PEO coating was shown to reduce the velocity of EOF by more than an order of magnitude compared to a bare capillary at pH 7.0. The coating protocol was important, especially at an intermediate pH of 7.7. The increase of pH in the cathodic (detection-end) buffer reservoir beyond pH ~ 8.0, e.g. as a result of electrolysis, had a large impact on the stability of the coating. This phenomenon may be used for the efficient and reliable fast regeneration of the column surface.

GENERAL INTRODUCTION

"Give me a fixed spot in the space and I will move the Earth." - was a bold promise made by a Greek scientist many centuries ago. I share his optimism; the sentence is an expression of the role of science for me. A scientist at the end of the twentieth century is assisted by unprecedently powerful friends. It does not take much effort to calculate the third side of a triangle when one has a calculator in hand. Much less than moving the Earth with a lever, for sure.

The development of the laser has been one of the greatest accomplishments of science in the twentieth century. The theoretical foundations were laid by Einstein in 1917.[1] The light amplification based on the proposed *stimulated emission* could be reached only under a condition known as *population inversion.* The prediction had to wait for several decades before it was fulfilled, but then the development was fast. The population inversion was first demonstrated between nuclear magnetic energy levels by Purcell and Pound in 1951;[2] the idea of amplification of microwave radiation was presented by Weber in 1952 and the first maser (Microwave Amplification by the Stimulated Emission of Radiation) was built one year later. Finally, in 1960, T.H Maiman constructed the first "optical maser", or laser (Light Amplification by the Stimulated Emission of Radiation), using ruby as the active material.[3] The discovery was followed by construction of numerous lasers in a variety of media.

Similarly to other science disciplines, the discovery of the laser has had a tremendous impact on analytical chemistry. Laser can deliver light at high irradiances, which significantly improves the sensitivity of traditional analytical methods, e.g. methods based on luminescence. Other methods, such as photoacoustic spectroscopy and thermal lens spectroscopy are subsequently becoming more popular. Some methods, e.g. Raman spectroscopy, would find only a limited number of applications without lasers. Spatial properties of the laser beams make the lasers compatible with microcapillaries or nanodevices. Monochromaticity of laser light can bring desired selectivity to all analytical methods based on interactions of light and matter.

This dissertation consists of two parts. Each part deals with use of a laser in a different area of analytical chemistry. In the first part, lasers were used not only for the desorption of a material, but also for the monitoring of the desorption and for improvements of the existing method. Use of a laser in the second part greatly simplified the experimental setup and lead to a better understanding of some phenomena in capillary electrophoresis. Each part begins with a general introduction of the area under study and continues with experimental arrangements relevant to the entire part. The results and discussion in part one are divided into three easy-to-survey separate chapters. Each of the three chapters also contains the experimental details specific to particular experiments. Both parts conclude with summaries. Finally, there is a general conclusion at the end of the dissertation.

PART 1.

LASER DESORPTION METHODS

CHAPTER 1. INTRODUCTION

Ionization of Large Organic Molecules for Mass Spectrometry

During the last two decades, important extensions of mass spectrometry to the study of involatile or high mass molecules were achieved. The general problem to be solved was how to generate intact ions of these molecules in the gas phase. Many of the compounds are thermally labile and decompose after heating. This problem may be reduced to two subproblems: first, it is necessary to volatilize the molecules and then to ionize them. Both steps quite often occur simultaneously. Several methods addressed the issue: field desorption,[4] laser desorption (LD),[5] plasma desorption,[6] secondary ion mass spectrometry (SIMS),[7,8] thermospray,[9] fast atom bombardment (FAB).[10] The most recent methods, elecrospray (ESI)[11] and matrix-assisted desorption/ionization (MALD/I),[12] are also the most successful ones.

ESI produces charged submicron droplets at atmospheric pressure by the action of a strong electric field. The droplets decrease their size by solvent evaporation and disintegration. Multiply charged ions are then produced from very small, highly charged droplets. ESI appears to be unlimited in the size of the molecules that can be ionized. The ability of ESI to generate multiply charged ions is perhaps as important as its ability to ionize the molecules without fragmentation. Analyses of ions with sufficiently low mass-to-charge ratios may be done with ESI coupled to an existing mass spectrometer. Molecules with masses of up to 100 000

Da are now analyzed routinely and single ions of megadalton DNA were detected by ESI combined with Fourier transform ion cyclotron resonance mass spectrometer (FT-ICR-MS).[13] Another advantage of ESI is its inherent compatibility with flow systems, such as LC or CE.[14,15] The main disadvantages of ESI is the production of more than one peak for a single compound, which reduces sensitivity and complicates analysis of polymer distributions. Also, the actual masses of polymers often cannot be determined because the mass spectrometers used lack the resolution to identify a series of adjacent peaks corresponding to consecutive charged states.

Development of Laser-based Ionization Methods

The efforts to volatilize larger organic compounds by simple thermal desorption are not successful because the heated molecules usually decompose prior to the evaporation. The principle of simple laser desorption (without any matrix) is to heat the molecules rapidly so that they can vaporize before they have time to decompose in the condensed phase. The use of a short laser pulse (less than 100 ns) is therefore essential. Two main types of lasers were successfully used for LD: infrared (e.g., CO_2 laser emitting at 1.06 μm) and ultraviolet (UV) lasers. Excimer and frequency-multiplied Nd:YAG lasers were among the most popular UV lasers used for LD. The establishment of LD meant significant improvement in mass spectrometry of more complex biomolecules. In 1978,

Posthumus et al. desorbed quasimolecular ions of stachyose and digitonin.[16] The method, originally designed for elemental analysis (LAMMA, LIMA), may also serve as a tool for the study of organic molecules. LD, however, cannot be used for larger molecules. The high-mass limit depends on the structural parameters of the analyzed molecules and the laser; it is about 1000 Da for biopolymers and 9000 for synthetic polymers. In addition, even the use of very short pulses cannot prevent significant fragmentation of analytes.

The discovery of MALD was directly related to LD experiments. Strong resonance absorption of UV light was found to promote desorption of intact aminoacids and dipeptides.[17,18] The ion signal appeared once a certain threshold level was exceeded and its intensity steeply increased with laser power density. The intact analyte molecules were observed only within a small power density region above the threshold value. Further increase of laser irradiation resulted in an increased photofragmentation and production of unspecific low-mass ions. The next logical step was to use a strongly absorbing compound to couple the laser energy necessary for vaporization of the analyte. Nonresonant absorption of the laser energy was excluded, because high power densities would have led to total destruction of the analyte. The idea was tested on small peptides or other biomolecules dispersed in a solid or liquid matrix.[12] Tanaka et al. successfully desorbed 100 000-Da protein from its mixture in ultrafine cobalt in glycerol matrix one year later.[19] A brief summary of major MALDI characteristics will be given in

this introduction. MALDI is a fast-growing area of analytical chemistry and it is behind the focus of this work to provide comprehensive coverage on this topic. In order to obtain a more complete list of the works on MALDI, the reader is referred to several excellent reviews.[20,21]

Matrices and Sample Preparation

An effective matrix should meet two major requirements. First, it should exhibit a strong absorption at the desorption laser wavelength. Second, it should serve as a "solvent" for analyte molecules. This is sometimes referred as "isolation" of analyte molecules.[21] Efficient matrices are often easily sublimable, which is a good prerequisite for easy desorption. Formation of low volatile salts of some acid matrices may be the reason why the matrices do not work when used from solutions with high pH.[22] Matrix molecules are likely to play an important role in the ionization of analytes.[21-23] The choice of matrix was found to affect the extent of the analyte fragmentation.[24] The matrix should also be soluble in desired solvents and its mixtures with analyte should form uniform films. The molar matrix-to-analyte ratios used range from 10 to 100 000 Da. The best results are obtained from samples with 1000-fold molar excess of matrix. With smaller ratios, fragmentation of analytes is promoted. With higher ratios, the limit of detection increases. Despite all known requirements on proper matrix, it is not yet clear, why some molecules may act as a

good matrix and others do not. Thus, the choice of the matrix is still largely empirical.

Extensive searches for good matrices have been conducted.[22, 25, 26] There are two main groups, solid and liquid matrices. The molecules of solid matrices often consist of an aromatic ring with a variety of substituents (often with a free electron pair or another double bond). Most common matrices used are nicotinic acid,[12] vanillic acid,[25] cinnamic acid derivatives,[27, 28] benzoic acid derivatives,[29, 30] or even ice.[31] 3-hydroxypicolinic acid seems to be particularly promising for complex analyses, such as DNA sequencing.[30,32] Liquid matrices include the slurry of ultrafine metal powder in glycerol[19] and 3-nitrobenzyl alcohol.[12] Matrices might also be roughly divided into two major groups according to the laser used for the desorption. For UV wavelengths around 250 nm, frequency quadrupled ND:YAG (266 nm) or KrF-excimer (248 nm) lasers are used. For wavelengths above 300 nm, the most frequent choices are nitrogen (337 nm), frequency-tripled Nd:YAG (355 nm), XeCl-excimer (308 nm) and XeF-excimer (351 nm) lasers.

Sample preparation plays a key role in MALDI analysis. A common sample preparation method, simple deposition of the mixture of analyte and matrix, produces inhomogeneous films. Such a film often contains the majority of the analyte in its center and the resulting MS signal varies with the desorption spot position. To improve sample film quality, use of two-component matrices or comatrices was reported.[33, 34] Addition of nitrocellulose to the matrix improved the

signal reproducibility for measurement of small peptides analysis.[35] The additives may serve as nucleation centers and simultaneously suppress the nucleation on imperfections of the metal probe. Preparation of a microcrystalline surface prior to application of the analyte solution may enhance the sensitivity, resolution and mass accuracy.[36] Mass discrimination effects stemming from sample preparation procedures complicate analysis of peptide mixtures; optimal results require parallel analyses with different matrices.[37] MALDI is very tolerant of sample matrix. Furthermore, impurities may be removed by immersing the dry sample film in distilled water.[38]

Applications

While original LD is limited to relatively simple organic molecules, the introduction of MALDI has led to a significant extension of the analyzed compound on large biomolecules such as vitamins, peptides, proteins, oligosaccharides or DNA fragments and synthetic polymers.[20, 21] MALDI is probably the best analytical tool for the determination of mass or mass distributions of organic polymers. Accuracy of 0.01% in mass determination was achieved with an internal standard on a time-of-flight mass spectrometer.[38] Relative simplicity of spectra, short analysis times, sensitivity and accuracy makes MALDI a method of choice for analysis of simple mixtures of biopolymers. The method also seems to find more and more utility in the analysis of oligonucleotides[30, 39] and protein sequencing.[40]

Desorption Mechanism

Although the original discovery of MALDI was made almost a decade ago, the mechanism is still not clear. There may exist several mechanisms, depending on experimental conditions. Nonequilibrium models of desorption include shock wave,[41] explosive desorption[42] or pressure pulse (implosive desorption).[43-45] According to the last model, absorption of the laser pulse results in a large number of mini-events, which cause ejection of the bulk of the material. Another model of layer-by-layer ejection neglects the transport of the heat caused by desorption.[46] Thermal models assume that the desorption of the sample is controlled by its temperature. The sample is heated as a result of absorption of the laser pulse and cooled due to heat conduction and evaporation (or sublimation)[47-49]. Bottleneck theory[50] was applied to MALD also.[48, 49] It explains why rapid heating of the matrix does not have to lead to overheating of the analyte and its subsequent fragmentation. In addition, significant molecular cooling during expansion of the plume was observed.[49, 51] Although a systematic effort was made to compare all three basic concepts,[45, 52] it may be impossible to find one comprehensive solution since conditions of MALDI experiments vary tremendously (e.g., matrices, analytes, laser wavelength, pulse length, frontside versus backside desorption geometry, "substrate-assisted laser desorption").[53]

An important characteristic of MALDI is the velocities of the matrix and the analyte molecules. This determines the energy spread (thus mass resolution) of the

desorbed material. It also allows proper coupling of a second laser beam to promote ionization independent of the desorption process. Beavis and Chait found the velocity of three proteins of different masses to be the same, about 750 m/s, and the velocity of the matrix somewhat higher, about 1150 m/s.[54] Pan and Cotter reported a similar velocity for matrix molecules, and different velocities for two proteins (of similar mass) of 500 and 1000 m/s.[55] The velocities estimated by other workers [56-58] are close to the velocities above.

The mechanism of ion formation by LD includes: direct photoionization and photofragmentation by the desorption laser, protonation and deprotonation reactions of excited and groundstated molecules and decay of clusters.[59] In MALDI, the excess matrix may form adducts with analyte molecules or serve as a source of protons for the analyte molecule[23]. Matrix molecules are likely to play an important role in ionization through their intermediate radical molecular ion.[21] Extensive classification of matrices according to their ionization characteristics was published.[22] On the other hand, this explanation cannot be used in cases of infrared desorption. Adducts of analyte molecules and sodium or potassium ions are also frequently present in spectra. Despite many possible mechanisms of ion formation, only a fraction of the analyte molecules desorbed by either LD or MALD methods are ionized.[60, 61] There is evidence a large amount of the analyte is desorbed intact.[62] An increase of ionization efficiency cannot be achieved by simply increasing the desorption power density because it promotes fragmentation. In fact,

the best results are always achieved with power densities slightly above the power density threshold. Another flaw of the ionization step is that some of the desorbed species might be ionized more efficiently than others. Furthermore, the extensive production of ionized fragments of matrix may saturate the detector and complicate mass spectra.

Photoionization for Laser Desorption Methods

To increase the ionization yield of the desorbed species, several postionization schemes are available: electron impact, glow discharge, chemical ionization or photionization. Wang et al. reported an increased ionization yield of gramicidin S when a plume of sodium cations was generated by a second laser next to the plume of the peptide.[63] He also noticed the abundance of quasimolecular ions generated by MALDI may increase, if the ion extraction is delayed, enabling more chemical reaction in the desorbed plume. Our attention is focused on photoionization which has already been proven to be both a highly efficient and versatile ionization method.[64-66] Photoionization has been successfully coupled to secondary ion mass spectrometry or sputtered neutral mass spectrometry (SIMS or SNMS),[64, 65] LD[66] and MALD.[67] Direct photoionization of the desorbed plume[67-77] or photoionization of the plume injected by a supersonic jet[78-85] was used. Photoionization techniques may be divided into two main groups according to the

number of photons needed for ionization: single photon ionization (SPI) and multiphoton ionization (MPI).

In SPI, absorption of a single photon is sufficient for ionization of the molecule.[66, 71, 77] Since the ionization potential of the molecules of interest ranges between 7 and 13 eV, it is necessary to work in the vacuum ultraviolet region, e.g. 118-nm light (10.49 eV). The method may be relatively "soft" if only a little excess energy of the photon is available for a bond cleavage. Another characteristic of SPI of sufficiently large molecules is its universality, because the cross sections of SPI are more uniform than those for MPI. A disadvantage may be the relatively low ionization efficiency, about 1%. The efficiency cannot be improved by simply increasing laser power density because of the higher probability of absorption of more photons and fragmentation.

MPI may be further divided according to its mechanism.[74] Nonresonant MPI is a nonselective method with nearly uniform selectivity for all elements. Absorption of two photons is usually sufficient for ionization of all species in the focal plane of high-power density (up to 10 GW/cm^2). It is a method of choice for analysis of inorganic samples. However, it does not provide useful structural information because absorption of additional photons leads to extensive fragmentation. Resonant multiphoton ionization (RMPI) is characterized by very high ionization efficiency and selectivity.[66] A molecule is excited to an intermediate state by absorption of the first photon. During the lifetime of the intermediate state, the

molecule can be ionized by absorption of the second photon. The absorption of the second photon can sometimes produce analytically useful fragments and fragment ions. Molecular ions may be further ionized and undergo another fragmentation in its excited state. These two fragmentation pathways are competitive; the former predominates at low power densities, the latter at high power densities.[75, 76] Thus, tuning the laser power may control the extent of fragmentation. The high probability for absorption of the first photon does not require use of large power densities for photoionization (1-10 MW/cm^2). The resonant absorption is also a prerequisite for high sensitivity, selectivity and low background of RMPI.

Two-photon resonant ionization was found to have extensive applications. In order to ionize common organic compounds, a variety of laser sources can be used, such as excimer lasers (193, 248, 308, 351 nm), frequency-multiplied Nd:YAG (266, 355) or tunable dye lasers. Light of 222 - 290 nm is excellent for ionization of small aromatic molecules, such as serotonin, tryptamine, benzimidazole, indole, tyramine, small peptides containing tyrosine, tryptophan, phenylalanine and others.[67, 68, 71, 72-76, 80-86] Photoionization is not, however, efficient in ionization of large molecules. Only molecular ions with maximal mass of several thousands were observed.[78, 79] Recombination of the ion pair created by ionization and fragmentation of the large molecule is believed to be more likely than release of a free electron.[87]

193-nm radiation is an interesting choice of wavelength for photoionization. No dye laser is needed, ArF-excimer can serve as the light source. The energy of 193-nm light is 6.46 eV. This is not enough for SPI, although some compounds with low ionization potentials[88] may exhibit laser enhanced ionization. 193-nm photoionization is not limited only to aromatic molecules; interaction of this light is reported from solution chemistry of biological compounds, such as aminoacids,[89] or nucleosides.[90] The high absorption coefficient related to the delocalized π-electron of the peptide bond ($7x10^3$ $Lmol^{-1}cm^{-1}$) was measured.[91] Absorption of the second photon generates specific fragments of peptides[91, 92, 76] and aminoacids.[74, 76] The entire process is very efficient. Reported dissociation efficiency reaches 100%. The sequence of oligopeptide obtained can be determined from its fragmentation pattern.[70, 93-95]

The ability to ionize only a specific class of compounds may enable one to distinguish them from a sample matrix. Analytically interesting systems are peptides and proteins in polyacrylamide (PA) gels. Polyacrylamide gel electrophoresis (PAGE)[96] is a popular method for protein separation and purification. Proteins can be separated in their native or denatured states. Most applications involve the use of denaturing anionic surfactants such as sodium dodecyl sulfate (SDS).[97] Under denaturing conditions, proteins are separated according to their size with the small proteins migrating faster than the large ones. Resolution of gel electrophoresis can be increased by separation in two dimensions under different conditions. Detection

of the proteins separated on gel slabs usually involves staining, autoradiography or immunoreactions, which potential is limited. The power of gel separation can be further enhanced by mass spectroscopy, enabling the identification of separated zones. Extensive effort was devoted to the development of an interface between gel electrophoresis and MS.[98] Classical identification of a protein consists of its postelectrophoretic elution, cleavage, purification and its mass analysis.[99] Alternatively, the digestion directly in the gel may precede the elution step.[100] Proteins may also be electroblotted from the gel to a membrane and analyzed from the membranes after necessary treatment.[101] The most promising approach avoids any transfer of the protein. Proteins are analyzed by MALDI directly from gels after washing the gel and addition of a matrix.[98] LD-RMPI of proteins and oligopeptides from untreated gels may be the simplest approach to protein identification. LD-RMPI does not substitute MALDI in determination of molecular ions, but it may provide sensitive and structurally-informative MS signals.

Time-of-flight Mass Spectrometry

The pulsed character of laser desorption methods makes them ideal ionization methods for time-of-flight mass spectrometers (TOF MS) although other types of mass spectrometers, especially FT-ICR-MS,[102] were successfully used too. Other types include magnetic sector MS,[103] quadruple ion trap MS[104] and combinations of two MS's.[105]

The principle of simple linear TOF MS is straightforward. The ions formed between electrodes in the source chamber are accelerated by an electric field into a longer field-free drift region and finally hit the detector. After their stay in the acceleration region, the ion's kinetic energy would ideally be equal to the energy of the electric field:

$$\frac{1}{2}mv^2 = zeEs,$$

where m is the mass of ion, v is the ion velocity, z is the number of the ion charges, e is the charge of an electron, E is the intensity of electrical field in the source and s is the distance traveled by the ion in the source region. The time t required to pass the drift region of length l can be expressed as

$$t = \left(\frac{m}{2zeEs}\right)^{\frac{1}{2}} l.$$

Direct proportion of m/z to t^2 can be seen from the last expression. Note, that the time t is not the entire time between the ion formation and its detection, but only its major part. Ions will also spend a certain time in the acceleration and detection regions. Actual construction of TOF MS may differ from case to case. The most

popular design of the linear TOF MS is probably the dual-grid design published in 1955 by Wiley and McLaren.[106]

Several attractive properties characterize the TOF MS. An entire spectrum can be recorded using a fast digitizer within only few μs. Theoretically, there is no upper mass limit. Theoretically all ions formed in the source chamber after the desorption may be collected and detected. The instrument is very simple, small and inexpensive.

The detector deserves important consideration. It has to be fast enough so that the resolution at a low mass range is not sacrificed. On the other hand, it should exhibit sufficient sensitivity for the high-mass ions. Microchannel plates (MCP), electron multipliers or postacceleration dynodes rely on production of secondary electrons released after an impact of an ion on the detector surface. Emission of the secondary electrons is inefficient below a certain threshold velocity of incident ions. Because the acceleration voltage is usually restricted to 30 kV, heavy ions of biological molecules can move with a limited velocity. Properties of existing detectors and design of sensitive detectors for heavy molecules are discussed in the literature.[107-109]

Resolution in TOF Mass Spectrometry

The disadvantage of TOF MS is limited mass resolution. Ideally, ions with a uniform velocity are instantaneously formed on an equipotential plane in the

acceleration (or extraction) field. Time of flight of such ions would only be dependent on their *m/z* ratio and the instrument would show infinite resolution. However, there are numerous factors which reduce the resolution of real TOF MS. These factors include inhomogeneous electrical field, space charge effects, insufficient speed of ion detector and signal recorder, finite time of ion formation, postsource decay of ions, velocity (energy) and spatial distributions of ions. Proper construction and alignment of ion optics (plates, grids) can make the electric field homogeneous. Space charge effect can be minimized by formation of only limited number of ions; this means using laser power as low as possible in the case of the laser desorption methods. The time response of commonly used detectors for TOF MS, such as MCP, is subnanosecond. Fast (1 Gs/s) A/D converters or high-frequency pulse counting techniques are available. The time of ion formation can be reduced if picosecond laser sources are used. If the postsource ion decay is excluded, the dominating factors limiting the resolution of analytical TOF MS are the spatial and velocity distribution of ions. Under normal experimental conditions, the velocity distribution of ions may be characterized by one-dimensional Maxwell-Boltzmann distribution with a mean of offset plume velocity, v_a, and standard deviation given by $(kT/m)^{1/2}$, where k is Boltzmann constant and T is absolute temperature. [110-112] The normal initial velocity distribution is added to the velocity gained by electrical acceleration and reflected in different arrival times of ions to the detector. Ionization occurs over a finite spatial volume of the sample. Because

electrical potential varies linearly with distance, different positions of ions result in their different velocity at the end of the acceleration region.

Several methods have been proposed to reduce the effect of initial spatial and velocity distributions. Wiley-McLaren's dual-grid design creates two regions of electrical field, extraction and acceleration field.[106] This enables one to achieve a compromise between spatial and velocity focusing. The same authors also introduced the concept of time-lag energy focusing,[68] which consists of insertion of a time delay between the ion formation and the application of the extracting pulse. During the lag period, the ions travel toward or away from the detector. After the electrical field is turned on, the ions which moved toward the detector are closer to it and receive smaller amount of acceleration and vice versa. Thus, the spatial resolution in the time of the electrical pulse corrects for the initial velocity distribution. This approach works well if the original spatial distribution is negligible. An alternative way of increasing the resolution is to eliminate the velocity distribution and correct for the spatial resolution.[112] Time-lag focusing is only one example of the methods using time-dependent acceleration fields.[113] Another popular way to correct the initial velocity distribution is reflectron TOF MS.[114, 115] An ion mirror is arranged such that the ions with larger velocities have to travel greater distances than the slower ones. The instrument may work also as a linear TOF MS and serve for studies of postsource decay.

In laser desorption methods, ion formation is supposed to take place in the condensed phase or in a dense phase formed near the sample. The velocity of the ions may be described by a broad Maxwell-Boltzmann distribution with an offset velocity of approximately 700 m/s.[54-58] This means that the resolution is limited by the velocity distributions. Classical dual grid TOF MS with time-invariant electrical fields does not provide sufficient resolution; the best resolution is achieved at high extraction and acceleration electrical intensities. A disadvantage of the reflectron TOF MS is its lower ion transmission, although a gridless instrument could be used.[116] In this situation, several groups successfully applied the original idea of time-lag focusing. Spengler and Cotter used an orthogonal pulsed extraction voltage to measure kinetic distribution of proteins. [55, 56] However, they do not report any improvement of resolution. Other groups applied the time-lag focusing successfully to increase the resolution for analysis of proteins and DNA.[39, 117-119] Special attention to the correlation between ion position and velocity is given in ref. 119. The authors put accent on the fundamental difference between the laser desorption/ionization method and conventional gas phase methods. The spatial and velocity distributions are independent in gas phase MS, while they are correlated in the LD MS. Thus, the larger the velocity of an ion, the further its distance from the repeller plate in the time of application of the pulse.

Our Goal

In spite of the achievements of MALDI, the method still has some limitations. Low ionization efficiency requires certain magnitude of the desorption power density and sensitive detectors. Typically, more than 10 single-shots experiments have to be averaged to achieve acceptable signal-to-noise ratio. Another source of poor reproducibility is sample inhomogeneity. Sometimes, many trials are necessary to find a surface spot which produces the desired signal. The signal may also appear only after several laser pulses are applied on the selected spot.[120] The most common lasers used in MALDI, nitrogen lasers, suffer from poor beam profiles and astigmatism. Recently, the importance of focusing[121, 122] and the incidence angle[45] of the desorption laser was shown.

Some difficulties accompanying the desorption methods could be overcome by separate optimization of the ionization from the desorption step. A secondary ionization scheme such as photoionization could be employed to improve the ion yield. Other advantageous side effects could be higher resolution, removal of matrix ions, altered ionization selectivity. Deeper knowledge of the desorbed plume dynamics would be useful for the design of a secondary postionization scheme, implementation of the "postsource decay" and for better understanding the desorption step. One way to learn more about the laser generated plumes is to monitor the desorbed species with an optical beam. There have been many attempts to image the plumes in the past. The data collected from many plumes at

specific sites may be combined to form an entire picture. Such an approach anticipates high reproducibility of plume formation since the image is a composite of many plumes. Although CCD detectors have undergone fast development in the past two decades, the readout is not sufficient yet. Thus, CCD is limited to the acquisition of one image.

In our group, an absorbance imaging system was used to study laser generated plumes of atoms,[123] diatomics[124] and larger molecules.[125] In order to increase the sensitivity of the measurements, fluorescence detection was developed and tested on model dye samples.[126] This was successfully applied to the study of plumes of proteins and DNA generated by MALD.[127] Optical probes are able to monitor all absorbing, fluorescing or scattering species, including neutral molecules, directly at the site of desorption and without interfering interactions with the electrical field. So, unlike mass spectrometric approaches, they are useful for providing insights into the mechanisms of desorption and ionization separately.

In this work, we use several different instrumental arrangements to characterize MALD at atmospheric pressure and in vacuum. We are able to improve the sensitivity of absorbance detection for the imaging system. The methods are sensitive enough to monitor single events, thus differences between plumes may be related to changes in various experimental conditions. Alternatively, the use of a static laser beam for observation enables reliable determination of plume velocities even when they are very high. Static scattering detection reveals negative impact of

particle spallation on MS signal. Large enhancement of sensitivity and selectivity in detection of aminoacids, aminoacid derivatives and dipeptides from polyacrylamide gels was accompished by secondary photoionization combined with laser desorption. Finally, 193-nm photodissociation is used to characterize the ion formation in MALDI process.

CHAPTER 2. CHEMICALS

Matrix and Analyte Selection

4-hydroxy-3-methoxycinnamic (ferulic) acid (Aldrich Chemical, Milwaukee, WI) was used as a model matrix on the basis of its proven utility in MALDI.[127] 0.1M matrix solution was prepared in a 50 : 50 ethanol : water mixture. All other chemicals were purchased from Sigma Chemical Co., St. Louis, MO.

Bovine serum albumin, BSA, was chosen as a representative protein. The absorption maximum of BSA labeled with tetramethylrhodamine isothiocyanate (TRITC) is 514 nm; suggesting it also absorbs at 488 nm. Previous work[127] has shown that the label remains attached to the protein throughout the MALD process.

Bovine insulin labeled with fluorescein isothiocyanate (FTIC) was used because of the unavailability of insulin labeled with TRITC. Excitation and emission maxima of FITC (495 and 525 nm) together with its molecular weight (approx. 6000) make it a suitable protein for simultaneous optical and mass study.

Bovine insulin, BI, was used as a common protein for testing MALDI-TOF MS. 1 mM solution of BI was prepared by dissolving in 0.1% trifluoroacetic acid.

Valine, phenylalanine, valine naphtylamide (VNA), valine nitroanilide, dansyl-valine, phenylthiohydantoin valine (PTH-Val), Val-Leu, Val-Phe, Phe-Val, guanosine, adenosine, cytidine, guanosine monophosphate and benzopyrene were used in the photoionization experiments. 1 to 5 mM solutions of these chemicals were

prepared in a 50 : 50 ethanol : water mixture. Use of rather concentrated stock solutions enabled preparation of thicker sample films.

5% PA gels were prepared from 10% aqueous solution of PA gel (M.W. 700,000 - 1,000,000) supplied by Polysciences, Inc., (Warrington, PA) by an addition of phosphate buffer (pH = 7.0, 20 mM ionic strength).

Sample Preparation

Considerable attention was devoted to the preparation of sample films. Concentration of both analyte and matrix, contents of ethanol or methanol and volume of deposited solution were optimized. Several sample preparation techniques were tested, such as evaporation at atmospheric and reduced pressures, evaporation at room or elevated temperatures, removal of solvent by sublimation from frozen films and utilization of a nebulizer. The best results were achieved by simple evaporation of the solvent at room temperature and atmospheric pressure. Optimal contents of ethanol in solutions were found to be approximately 50%. Deposition of larger than necessary volumes of sample resulted in an uneven coverage of designated area.

A desired amount of BSA was dissolved in water, mixed with an appropriate volume of the matrix solution and was brought to a final volume of 400 µl with water. This volume was deposited on a clean quartz plate so that the resulting film would cover a 10-cm^2 circular area. The deposited solution was dried slowly at room

temperature. The best films of BSA with ferulic acid were prepared from solutions with matrix-to-analyte ratios of 100 to 200. The film was homogeneous and only slight contours (of thicker and narrower regions) resulting from uneven rate of evaporation were observable. The films prepared from solutions of lower matrix-to-analyte ratios were homogenous, but the solution did not cover the entire area on sample plate. Many crystals were present at higher matrix-to-analyte ratios and the film coverage was uneven. Film thickness also had an effect on plume appearance. This effect was not examined in detail here.

Samples for mass spectroscopy experiments were prepared on stainless steel tips. Aluminum tips were used in photoionization experiments. In order to improve the coverage of the tip with sample films, the deposition area of the tip was roughened (sand-blasted). The diameter of the deposition area was 6.35 mm. 10 μl of analyte solution or a solution of analyte with ferulic acid was deposited on the probe tip and dried at room temperature. Larger amounts of deposited solutions caused uneven coverage and made films less homogenous. As much as 40 μl of the solution of (labeled or unlabeled) insulin with ferulic acid could be deposited to prepare a thick film. Gentle cooling of the solution and the probe tip by evaporation of solvent contributed to even coverage. For this reason, placing the probe tips into a metal holder during crystallization could lead to uneven coverage. Films were crystalline and relatively uniform with a thicker ring formed at the edge.

Mixture of VNA with 5% PA was made by simple addition of 5 - 50 μl stock solution of VNA gel to the PA gel. Approximately 10 μl of 5% PA gel or its mixture with analyte was deposited on the probe tip. Such a sample was analyzed after drying ("dry" sample) or within one minute after its exposure to the vacuum ("wet" sample).

CHAPTER 3. ATMOSPHERIC-PRESSURE STUDIES

Acousto-optic Devices

The function of acousto-optic devices (AOD) is based on diffraction of light by an acoustic wave.[128, 129] The devices are known as Bragg cells and are used as modulators, deflectors or monochromators. The Bragg cell[130, 131] consists of a piezoelectric transducer attached to an acoustic medium transparent to the light of desired wavelength. High frequency sound waves launched by the transducer into the transparent medium produce periodic change in the density of the material. Because refractive index is a function of density, constant frequency sound waves produce a moving transmission grating.

In the Bragg regime ($L > \Lambda^2/\lambda$, where L is the light-sound interaction length, Λ is the sound wavelength and λ is the light wavelength) an incident laser beam enters the cell at an angle of $\lambda/2\Lambda$. Most of the light will be diffracted to the first order. The diffraction angle Θ can be calculated from the relationship:

$$\sin\Theta = \frac{n\lambda}{2\Lambda}$$

where n is the order. By varying the frequency of the acoustic signal, the diffraction angle is changed. In this manner, a laser beam can be scanned through space at very high rates (hundreds kHz in our case).

Deflector resolution N, the number of resolvable elements across the total scan angle is given by:

$$N = \frac{\pi \Theta_T D}{4\Lambda}$$

where Θ_T is the maximum deflection angle and D is the focused beam diameter. The maximum deflection angle is given by the transducer bandwidth.

Another limitation of the AOD is known as a cylindrical lens effect.[128, 130] Essentially, a fast change in the frequency of the sound wave results in nonuniform wavelength of the sound wave along the direction of its proliferation. The focal length f of the cylindrical lens is given by:

$$f = \frac{VT}{\Theta_T}$$

where V is acoustic wave velocity and T is total scan time. Increasing the scan rate leads to a decrease of the focal length. For this reason, a compromise between the scan rate and the resolution had to be made in our work.

The scanned probe laser beam may be used for imaging in a variety of detection modes, e.g. fluorescence, absorbance or scattering. In all modes, the probe laser beam is directed to a discrete location which size is given by quality of the beam focusing. As mentioned above, the scanning is limited by the maximum

deflection angle, resolution and cylindrical lens effect. For a given optical configuration and a scan rate, a scan consists of a certain number of resolution spots.

Adding a second AOD orthogonal to the first one and to the laser beam enables scanning of the laser beam through two dimensions. The first AOD is used to scan through space in the horizontal dimension, the beam moves from left to right and back. During this movement, the second AOD deflects the beam in a second dimension; from the bottom of the scanned region to its top and back. The period of the vertical movement is twenty times shorter than the period of the horizontal one. In other words, to obtain a single image of the scanned area the beam moves once in the horizontal dimension and twenty times in the vertical dimension. The acquisition system has to record enough data points during the vertical movement in order to retain the spatial resolution achieved by AODs.

The piezoelectric transducers of each AOD are driven by a voltage controlled generator. By varying the input voltages for the generators in a precise manner with another oscillator, the beam can be moved very reproducibly in space. The speed of AODs is sufficient for submilisecond 2D - scans. This allowed us to take several consecutive images of a plume generated by a single desorption pulse (Fig. 1).

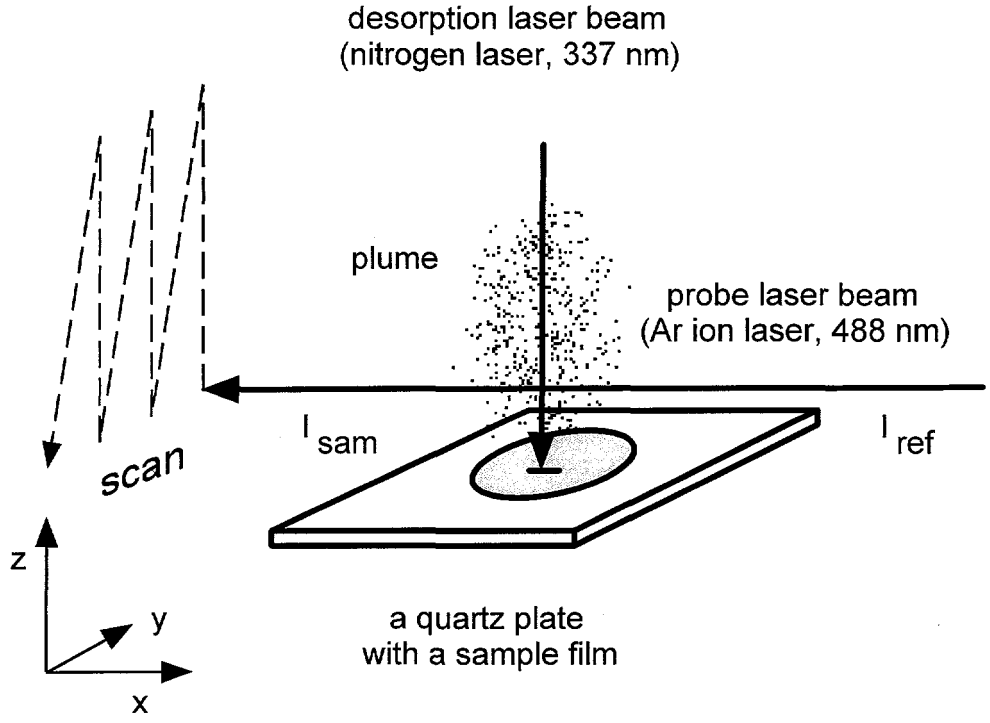

Figure 1. Two-dimensional imaging of a desorbed plume.

Instrumental

A pulse (337 nm, 9 mJ, 10 ns) from a nitrogen laser (Laser Photonics, Orlando, FL, Model UV24) was used for desorption of the sample. The laser was run at 6 Hz synchronized with line frequency and single pulses were chosen with a mechanical shutter (Melles Griot, Boulder, CO, Model 04 IES 003) by an electronic controller circuit. The schematic of the electronic controller circuit and its timing diagram is shown in Appendix A. In brief, the controller divides line frequency by 10 to obtain the trigger for the desorption laser pulses. At the same time, it waits for a manual trigger and opens the electromagnetic shutter to transmit just one pulse out of the 6-Hz pulse train. The resulting pulse-energy fluctuations were better than ± 2% (90% between ± 1%). The nitrogen laser was focused by a quartz spherical lens (178 mm f.l.) and reflected at 90 degrees to a sample plate by a mirror. A quartz cylindrical lens (127 mm f.l.) was added if the beam shape was to be changed. The sample film was on the upper side of the quartz plate (frontside desorption). Typical foci had a shape of a line parallel to the probe laser beam in order to increase absorption pathlength. The energy of each laser pulse was monitored by measuring the natural reflection off a quartz plate with a pyroelectric energy probe (Molectron, Campbell, CA, Model J3-09) and recorded with an A/D converter (DataTranslation, Marlboro, MA, Model DT 2827). The desorbed plumes were interrogated by an argon ion laser (Laser Ionics, Orlando, FL, Model 554A) at 488 nm. Two different modes of imaging were employed.

For 2-D scanning (Fig. 2), the probe laser beam was directed by two mirrors into two AODs. One (Isomet, Springfield, VA, Model 1205C-2) scanned the beam in the horizontal direction and another (IntraAction, Belwood, IL, Model ADM-150, driver DE-150) scanned the beam in the vertical direction. The AODs were driven by asymmetric triangular waves at 10 kHz (horizontal) and 200 kHz (vertical) from two function generators (Wavetek Corp., San Diego, CA, Models 182A and 162, respectively). The beginning of the first scan was triggered by the same signal which triggered the desorption laser, and ten scans were typically recorded. The entire area was scanned in 100 μs. An aperture was used to block the zero- and second-order beams from the deflectors. A lens (100 cm f.l.) was placed behind the aperture to improve spatial resolution in the plume region. The beamwaist (50% intensity) was about 0.7 mm vertical and 0.3 mm horizontal. The typical scan area has a width of 8 mm and a height of 9 mm. Two wedge prisms were used to sample a (naturally reflected) fraction of the probe beam before and after the plume region. The reflected reference and signal beams were collected by two lenses (50 mm f.l.) and focused onto two phototubes.

It was necessary to make the paths of the reference and signal beams as similar as possible (incidence angles on the wedge prisms and lenses, distances between the elements). The key difference between the signals from the two channels was optical interference at the entrance windows of the detectors. This had to be removed by opal diffusers placed directly on the entrance windows of the

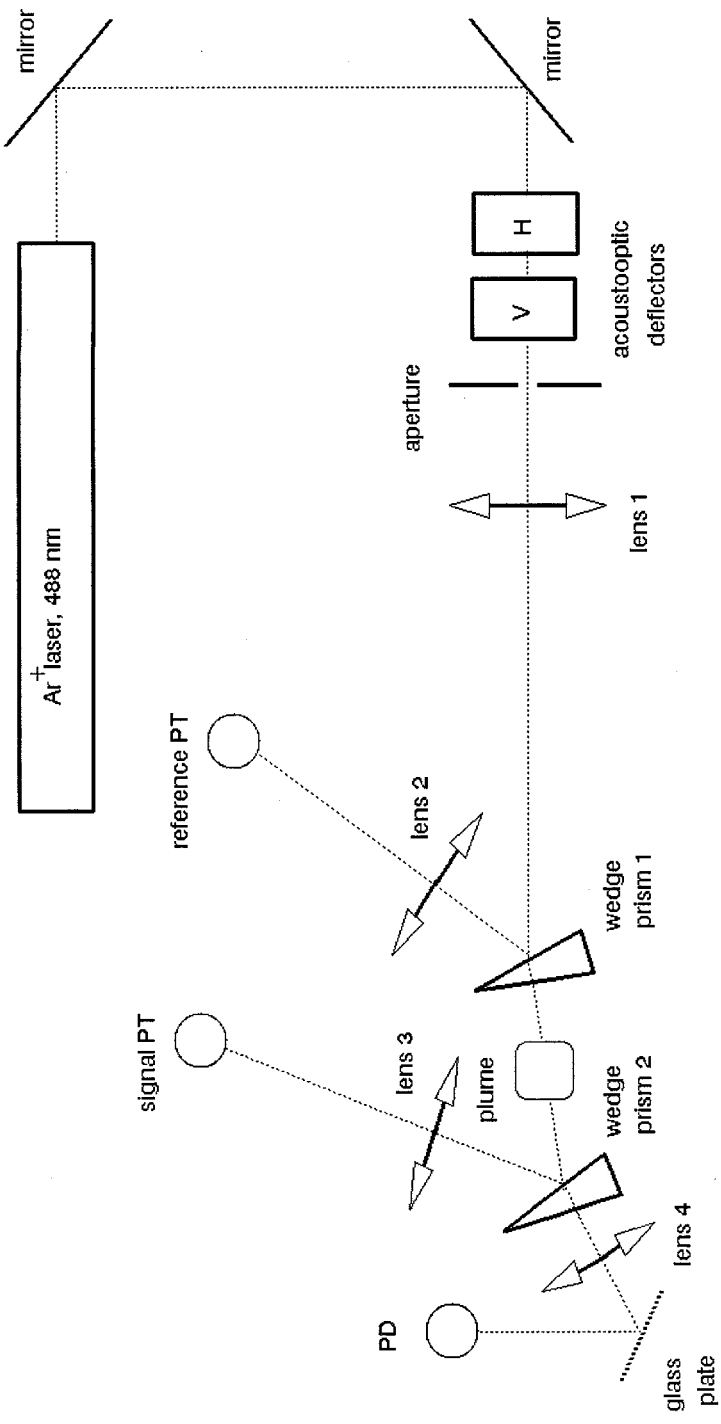

Figure 2. Experimental arrangement for 2-D absorbance scanning.

phototubes. Phototubes (Hamamatsu, Model R645) were used because of the large transparent photocathode and the small capacitance (allowing sufficient bandpass). Extensive precautions were taken to minimize any differences between the reference and the signal photocurrents, but even with the most careful alignment, some small systematic deviations were observed during measurement of the blank (no plume). All measurements were thus corrected by digital subtraction.

The two photocurrents were amplified by home-built current/voltage converters (Fig. 3). The difference voltage was amplified by an additional summing junction inverter, which also corrected for the relative intensities in the two channels (the intensity of the signal beam is lower than that of the reference beam because of two preceding reflections at the first wedge prism). The output voltages corresponding to the difference in photocurrents and to the reference photocurrent were recorded by a digital oscilloscope (LeCroy, Chestnut Ridge, NY, Model 9410) and transferred to a computer. The signal of photodiode (PD) was used for data processing. The glass plate is positioned in such a way that the photodiode senses the light only if the probe laser beam is in its top position. The computer programs used to create figures from raw data are shown in Appendix B.

The acoustic signal associated with each desorption event was monitored by a condenser microphone element (Radio Shack, No. 270-092B) positioned approximately 3 cm from the desorption spot close to the surface normal. The acoustic signal together with the signal from the energy probe was recorded with the A/D

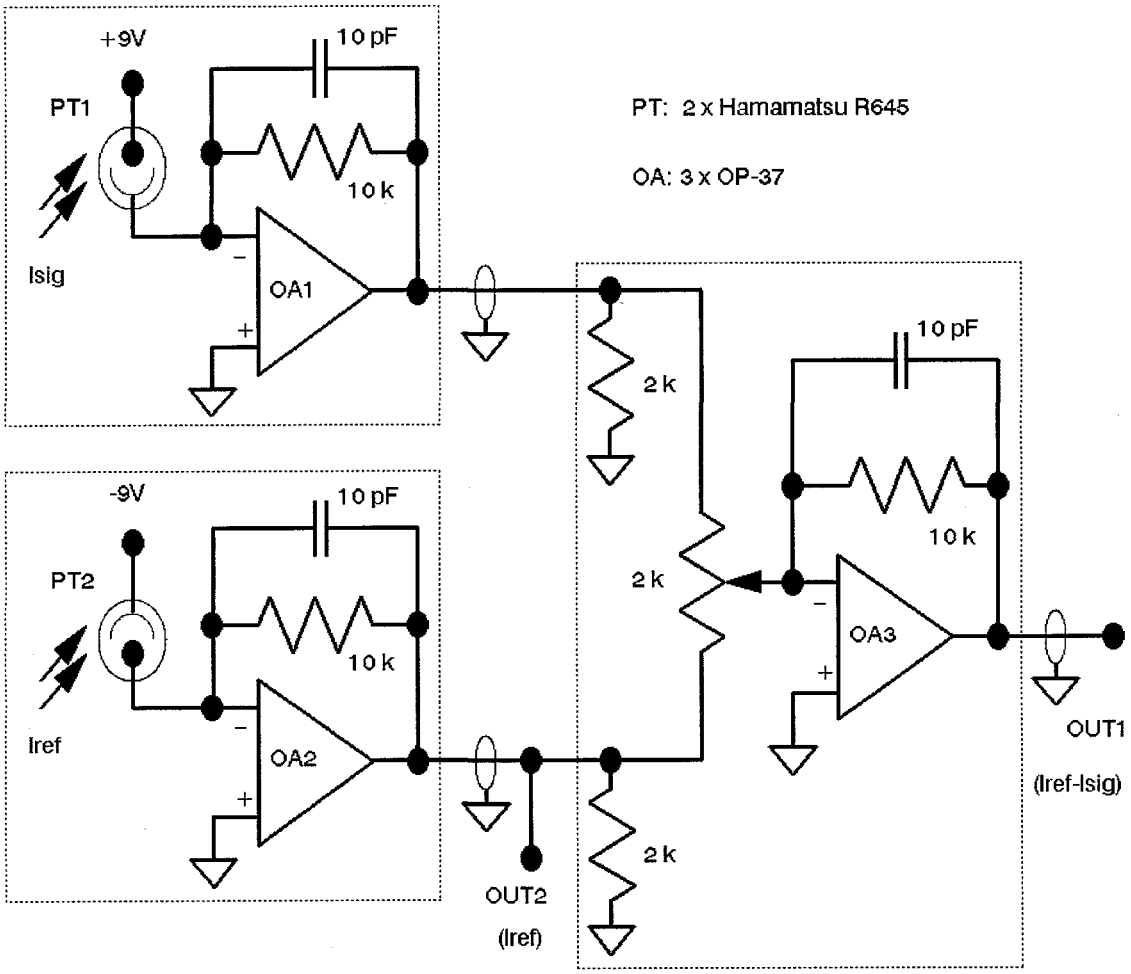

Figure 3. The schematic of the circuit used for absorbance detection. Two signals (OUT1 and OUT2) were recorded.

converter running at 130 kHz. The acoustic signal of interest, the first positive wave, arrives approximately 150 μs after the desorption laser pulse, while the signal from the energy probe, is almost instantaneous (Fig. 4). A high speed, electronic relay circuit (with DMOSFET SD5000) was built to switch the input of one A/D channel from the energy probe to the microphone and to obtain the important portions of both signals. Software switching of input channels of the AD converter was too slow (miliseconds) and use of two separate AD channels simultaneously would have reduced time resolution.

For 1-D scanning the optical setup and data acquisition remained the same, except that the first AOD was removed. The probe laser beam was deflected perpendicular to the sample plate above the desorption spot with a period of 5 μs. The purpose of the 1-D scanning mode of observation was to obtain more information about the position of the plumes during the first 200 μs, especially the plume velocity. The bottom of the scan region was brought as close as possible to the sample plate. The sample plate can create false absorbance due to refraction, which had to be subtracted out. The distance of the center of the beam from the plate at the point of closest encounter was estimated to be 0.5 mm.

Optimization of Absorbance Detection

Absorption mode of detection was chosen rather than fluorescence because relative measurements offer better reproducibility and quantitative accuracy.

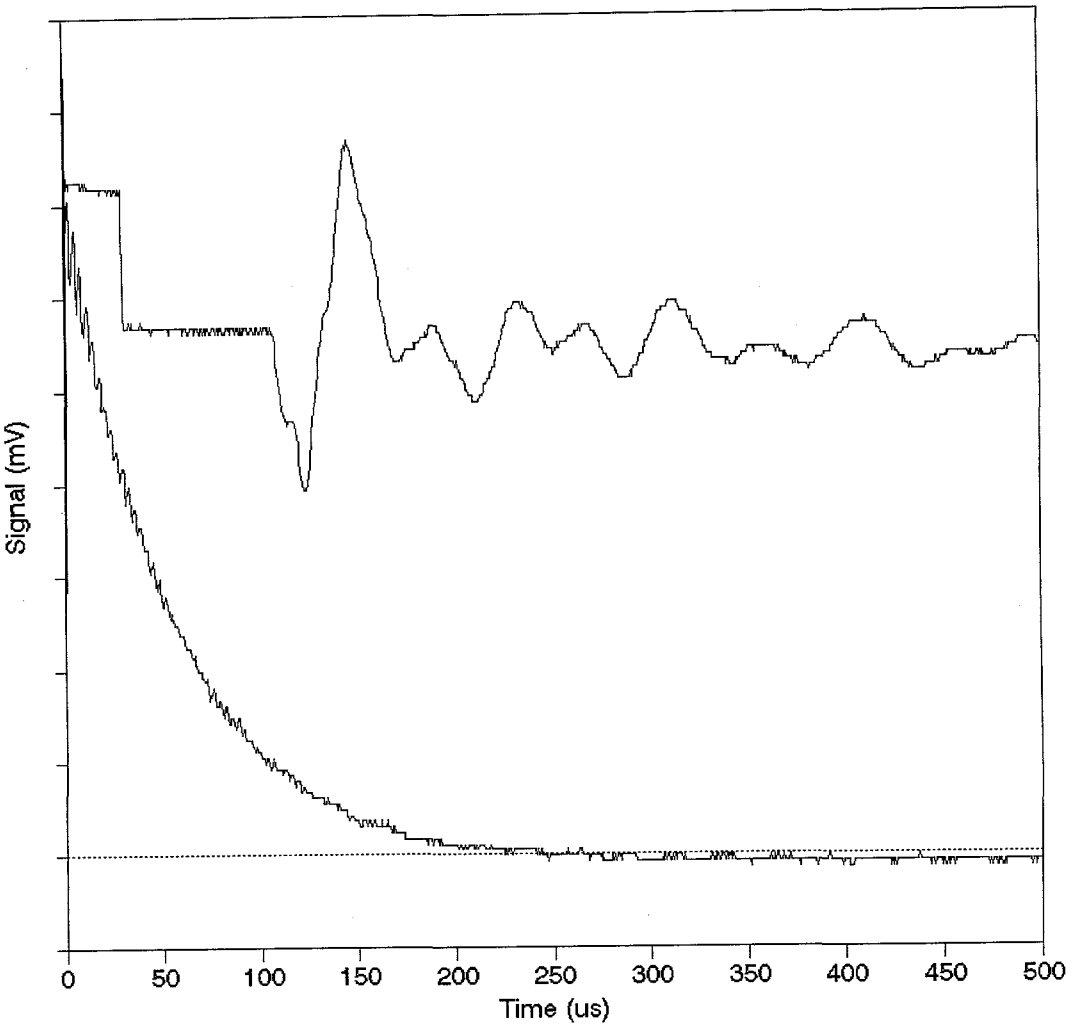

Figure 4. Acoustic signal produced by a desorption event (upper trace) and a signal from the desorption energy probe. The first step in acoustic signal corresponds to switching between the channels.

Besides, it was possible to bring the probe laser beam closer to the sample film without interference from light scattering or fluorescence of the sample film. However, there are still many limitations one needs to deal with. For example, the size of the probe laser beamwaist must be small compared to the plume size. To reduce errors in the measured absorbance because of beamwaist variations, parameters affecting the size of beamwaist such as the position of the long focal-length lens and the frequency of deflection were kept constant and the probe laser power was maintained to within ± 10%.

The period of the line frequency was long in comparison with the data acquisition period and line interference resulted in a "dc" shift. It was reduced by digital subtraction and synchronization of the entire experiment with the line frequency. The optimum rate of the desorption laser was 6 Hz. At this rate, the fluctuations of the pulse energy were minimized and pulses were synchronized with the line frequency. In order to apply only one laser pulse to the sample, an electromagnetic shutter with an electronic controller had to be used.

As mentioned above, digital subtraction of blank (no plume) absorbance had to be used to prevent false absorbances resulting from the systematic differences between the two channels. The use of the digital subtraction imposes strict requirements on the quality of the generators driving the movement of the probe beam. A frequency change of 0.01% or a time shift of 100 ns resulted in an imperfect subtraction. The effectiveness of the subtraction could be improved by

replacing the analog waveform generators with digital ones. Another way to reduce the systematic noise is with digital filtration. Fig. 5 shows the FFT of a signal (upper trace) and blank (lower trace) raw data suggesting the noise may be significantly reduced by low-pass (1.3 MHz) digital filtering after the subtraction. The low-pass FFT filtering was not routinely used since it did not have any effect on the values of integrated absorbance. The digital subtraction significantly reduced the systematic false absorbances and dc offset errors despite occasional imperfect subtraction due to the analog generators. Other noise sources such as electronic noise or noise due to vibrations of optical components were small in comparison with errors due to the imperfect subtraction.

The standard deviation of the blank absorbance integrated over the entire scan region of 8 × 9 mm (44 × 19 data points) was 0.050. The dominant cause of this variation was imperfect subtraction of the "dc" offset. The standard deviation of plume absorbance from one shot to the next was even higher (0.15 from integrated signals in the last scans), mainly because of variations in film thickness and morphology. Typical reproducibility of integrated plume absorbances of 5 plumes is shown in Fig. 6.

Several combinations of detectors and different circuits were tested in order to find the acquisition system which offered the lowest detection limit. The electronic noise canceller,[132] which was previously used to improve the detection limits in capillary electrophoresis[133] and liquid chromatography,[134] is worth mentioning.

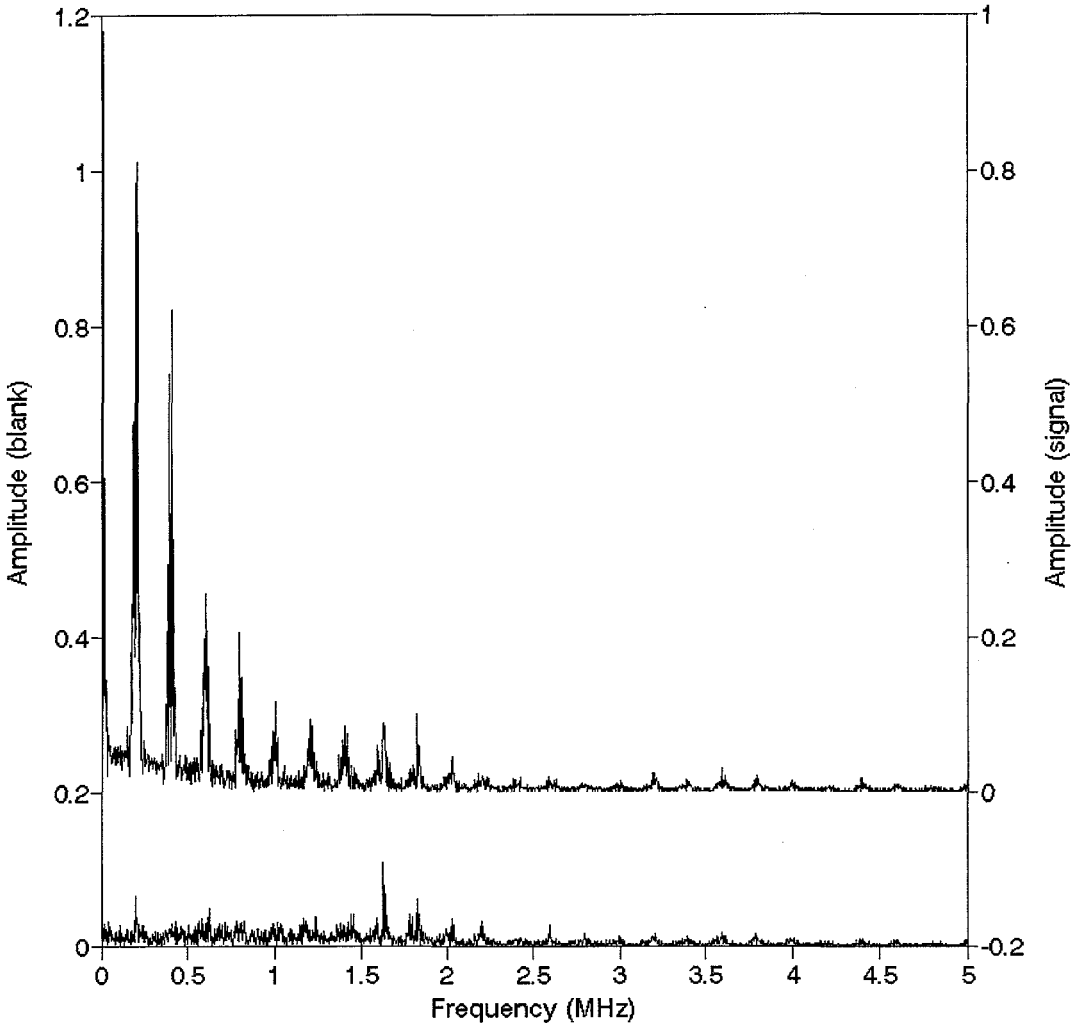

Figure 5. FTT spectra of raw absorbance data generated by a plume desorption (upper trace) and from blank measurement (lower trace).

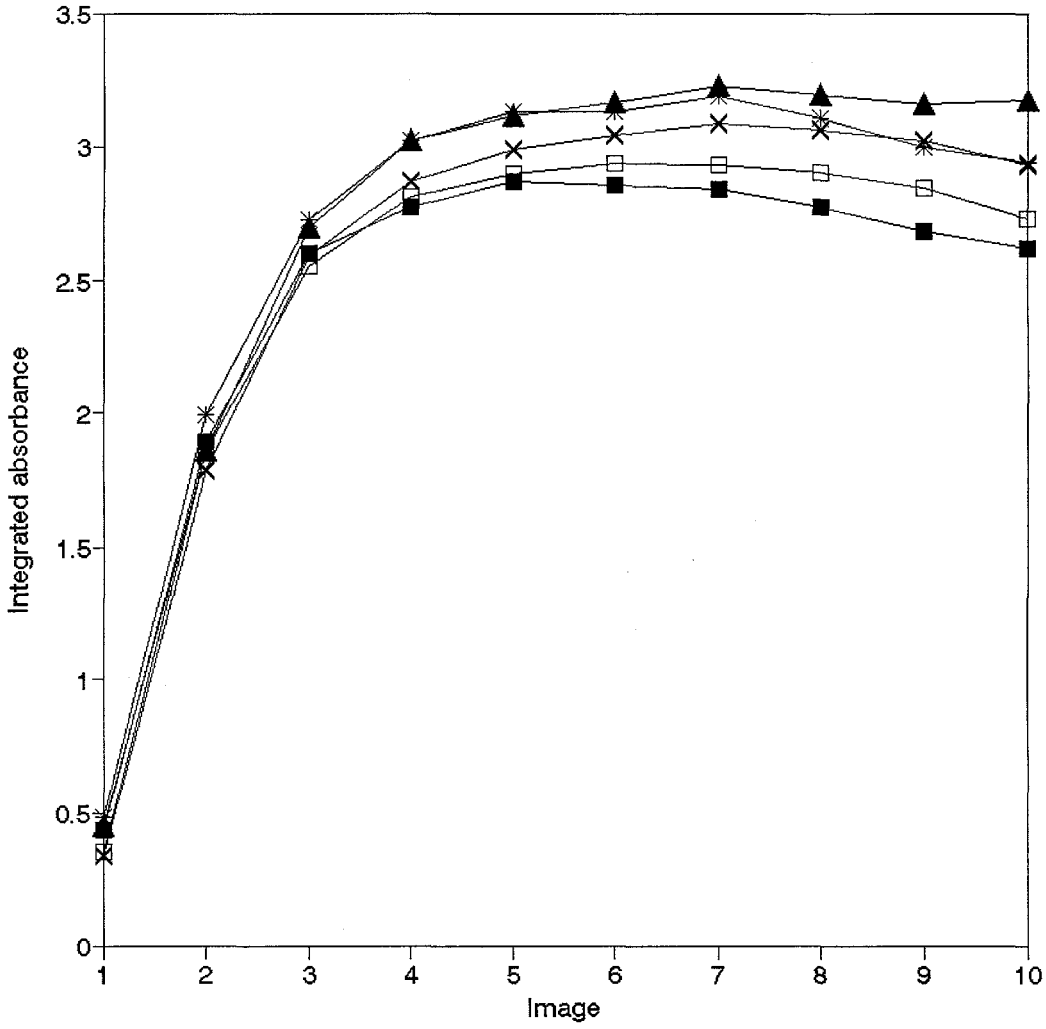

Figure 6. Temporal development of the integrated absorbance of 5 initial-shot plumes. All conditions are the same as in Fig. 9.

Unfortunately, the proper function of the circuit is based on the assumption of very similar signals in the both absorbance channels, which is not true in case of the 2D-imaging setup.

Matrix-to-analyte Ratio

A set of experiments were done to find the optimal matrix-to-analyte ratio within the range 75 to 300. The power densities at the desorption spot were of the order of 10^7 W/cm^2. The films with the ratio of 150 produced plumes of the largest size (absorbance integrated over the entire scan region). Plumes usually reached their maximum integrated absorbances towards one of the last scans.

No absorption of the probe beam was observed from a film of only ferulic acid, although a considerable amount of the ferulic acid was removed and the entire spot was cleaned by several laser pulses. Ferulic acid does not absorb at 488 nm and light scattering was not large enough to produce an observable absorption signal. Likewise, a film of BSA did not give any absorption signal either. This is because a very small amount of BSA was removed; the film was virtually intact after several laser pulses. This means that the absorbance signal (in all modes of measurements below) corresponds only to a plume of dye-labeled BSA, its fragments, and possibly released dye molecules created by MALD.

Power Density

The intensity of the desorption laser beam was adjusted by inserting quartz or glass plate(s) into the beam path while the focus of the nitrogen laser was not changed. The plumes started to appear above a certain threshold level (Fig. 7). Plume absorbance integrated over the entire scan region increased approximately linearly with increasing energy of the desorption pulse except at the highest energy level. The threshold levels and the slopes depended on matrix-to-analyte ratios but without any particular trend. The film with a ratio of 150 produced the largest integrated absorbance and showed the lowest threshold.

The occurrence of an energy threshold is mentioned in all papers dealing with MALD; threshold power densities are usually close to 10^6 W/cm^2. The threshold power density in our case seems to be somewhat higher, about 10^7 W/cm^2. This may be related to the relative sensitivity of absorption vs. MS detection. At low power densities, only several monolayers of material are removed per pulse,[62] which is well below the detection limit for absorption measurements. More interestingly, the increase of the signal with pulse energy was less steep than reported,[54] where it was found to be proportional to E^n with n ranging from 4 to 6. Those studies, however, relied on the MS as the analyzer, whereas all species, including neutral molecules, are detected by our method. Since only a tiny fraction of the desorbed molecules is supposed to undergo ionization, the rapid increase of ion signal[54] implies a higher efficiency of ionization at higher energy levels.

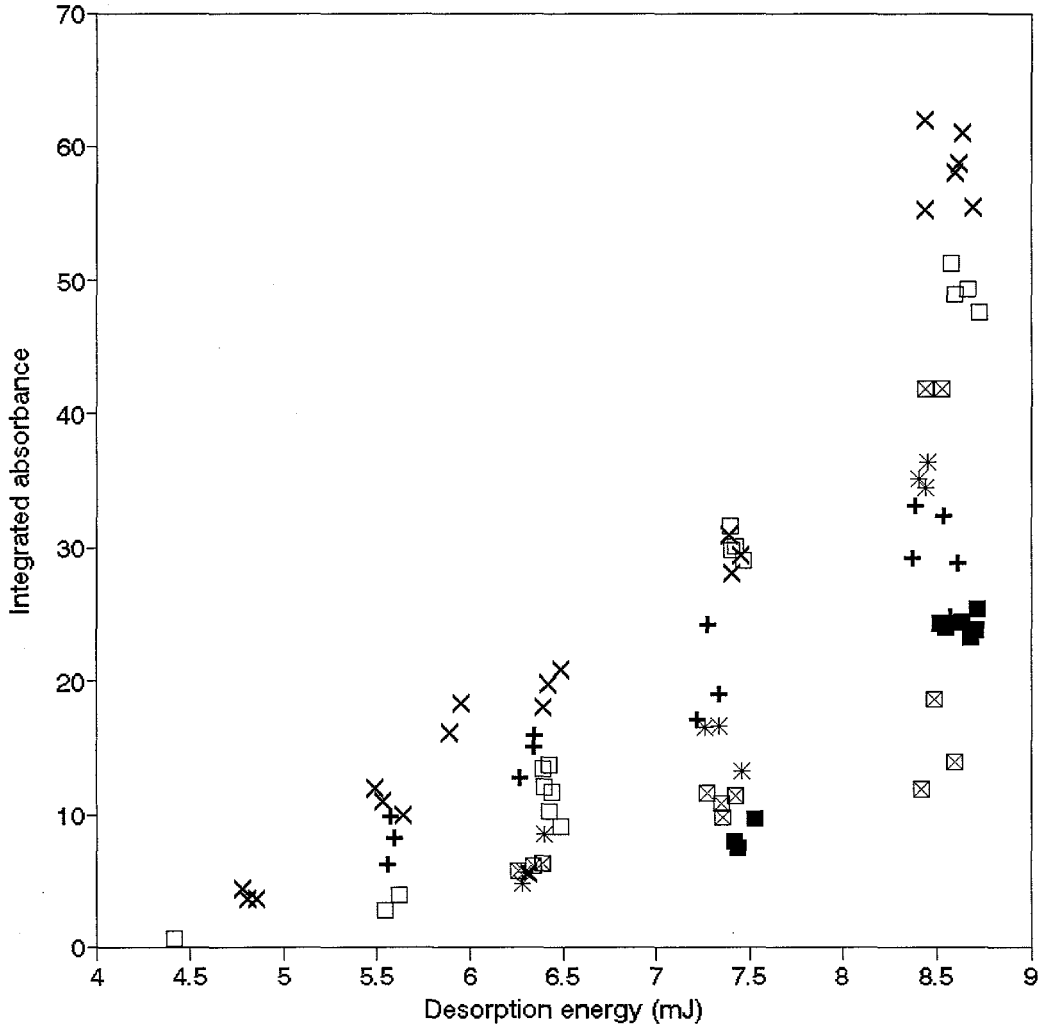

Figure 7. Total plume absorbance as a function of the pulse energy of the desorption laser for sample films of six different matrix/analyte ratios: ■, 75; □, 100; **X**, 150; ✶, 200; ⊠, 250; and +, 300. Spot size: 0.4 mm^2.

Acoustic Signal

The magnitude of the acoustic signal was determined as the height of the first positive wave (Fig.4). The correlation of plume size (integrated absorbance) with the acoustic signal is shown in Fig. 8. Previous work from our group has shown that this signal correlates well with the amount of material vaporized.[135, 136] The plumes from the first three shots at a given spot were studied for films that have different matrix-to-analyte ratios (in the range from 100 to 300) and different thickness (approximately from 1 to 10 μm). Despite the wide variety of sample character and the far-from-optimal desorption-laser spot, two main groups of the plumes are evident: the plumes generated by the first shot and the group from the second and third shots. A rough linear correlation was found for each group. The acoustic signal was not zero (intercept on y-axis) even if there was no observable absorption. This signal was due to the photoacoustic (heating) effect. There was an increase of the y-intercept of the second group; the surface was probably rougher and gave a larger photoacoustic signal. The acoustic signal increased faster as a function of the integrated absorbance in the case of the second and third shots. This may be due to a larger number of molecules formed (higher acoustic signal) for the same number of desorbed dye molecules (absorption), that is, due to fragmentation of e.g. the matrix molecules. Another possible explanation of the higher acoustic signal is the faster initial velocity of the plumes generated from the second and subsequent shots. The linear dependence between the acoustic signal and the

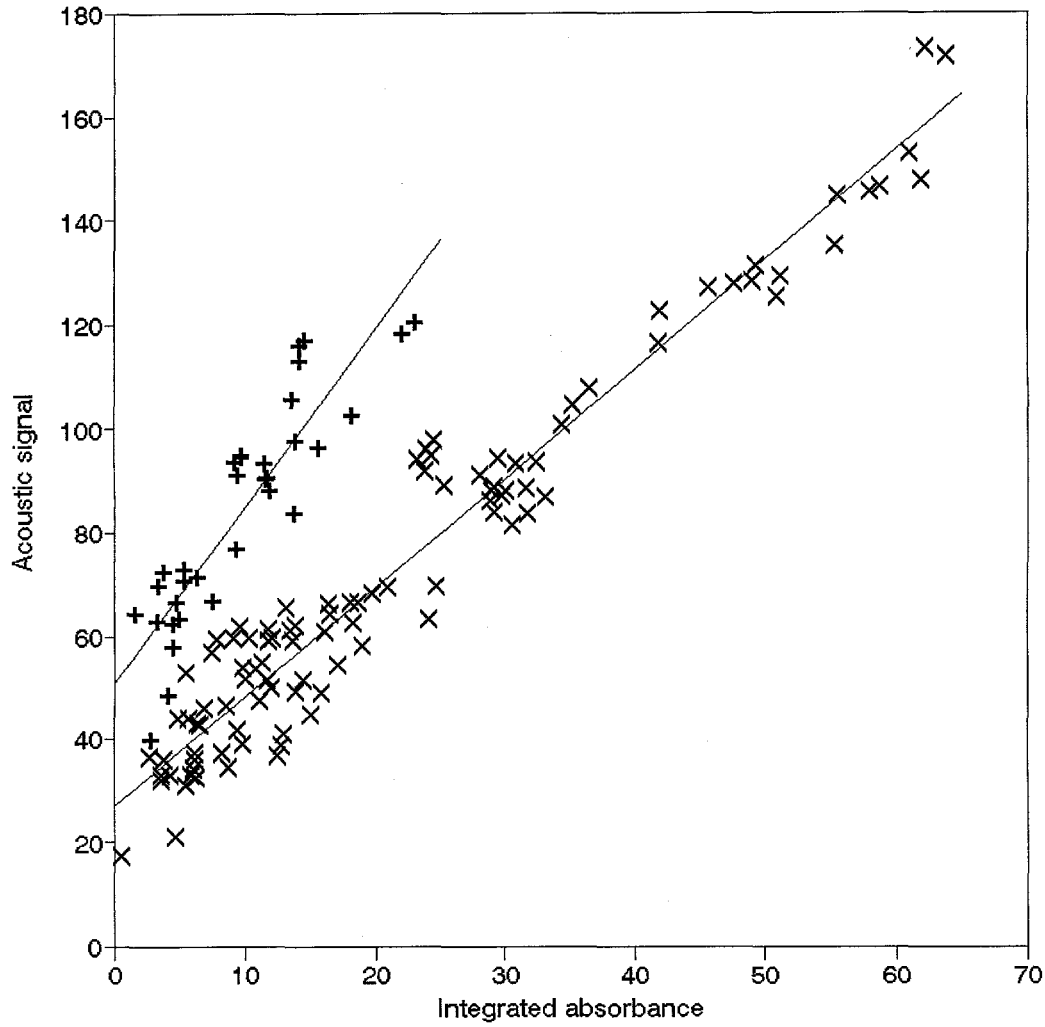

Figure 8. Correlation of the integrated plume absorbance with the acoustic signal generated during desorption over a range of experimental conditions. Correlation coefficients are 0.946 for plumes from the initial laser shots, **x**, and 0.796 for the plumes from the second and third laser shots, **+**.

integrated absorbance suggest that the acoustic signal may be used for simple independent monitoring of the amount desorbed per pulse in MALD.

Plume Characteristics

Spatial and temporal dependence of the absorption signals are shown in Figs. 9 and 10. Very good signal-to-noise ratios were achieved, allowing closely spaced contours to be plotted. The plumes produced by the initial shot appear different in comparison with the plumes desorbed in subsequent shots; they had different sizes, different vertical velocities and different spatial distributions. The plumes from the second and subsequent shots looked qualitatively the same as one another until the film was consumed. At atmospheric pressure, the first shot produced one plume the velocity of which dropped gradually within the 1-ms observation period (Fig. 9). Sometimes tailing or even a smaller second plume appeared behind the first plume. Subsequent shots produced plumes in which the velocity was also gradually reduced, but in many cases (Fig. 10), two plumes could be observed: a larger, slow one and a smaller, fast one.

There was significant difference between the two plumes produced by the initial shot and those produced by subsequent shots. The formation of the second plume in the first case was slow; it could be the result of thermal vaporization after equilibration at the surface. On the other hand, two plumes were present from the very beginning in the case of the other shots (Fig. 10). The slow plume resembled

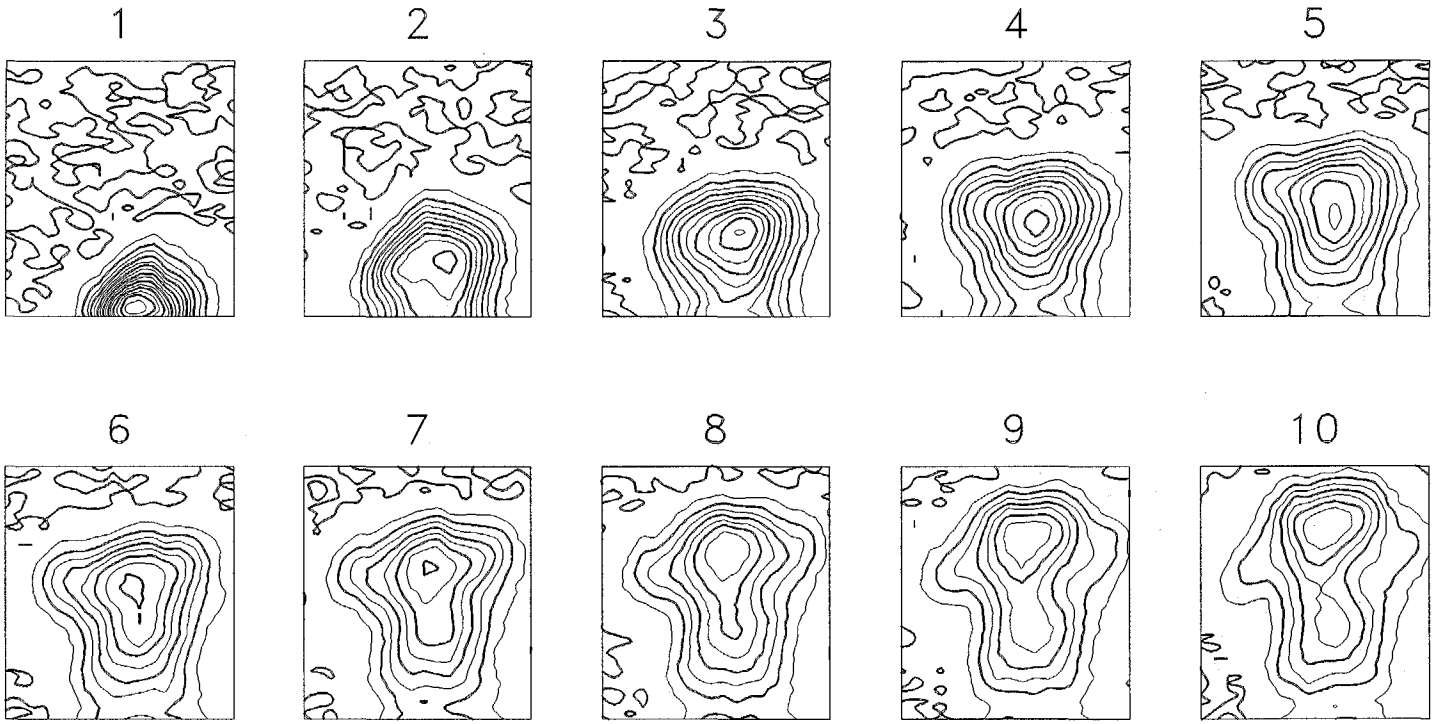

Figure 9. Temporal development of an initial-shot plume. The desorption spot is at the center of the lower edges of the frames. Matrix/analyte ratio, 150; film thickness, approx. 5 μm; desorption laser spot, 0.50 × 2.5 mm; power density, 62 MW/cm^2; scan width, 8.0 mm; scan height, 9.0 mm; scan rate, every 100 μs; and contour levels, 0.005 a.u. per step.

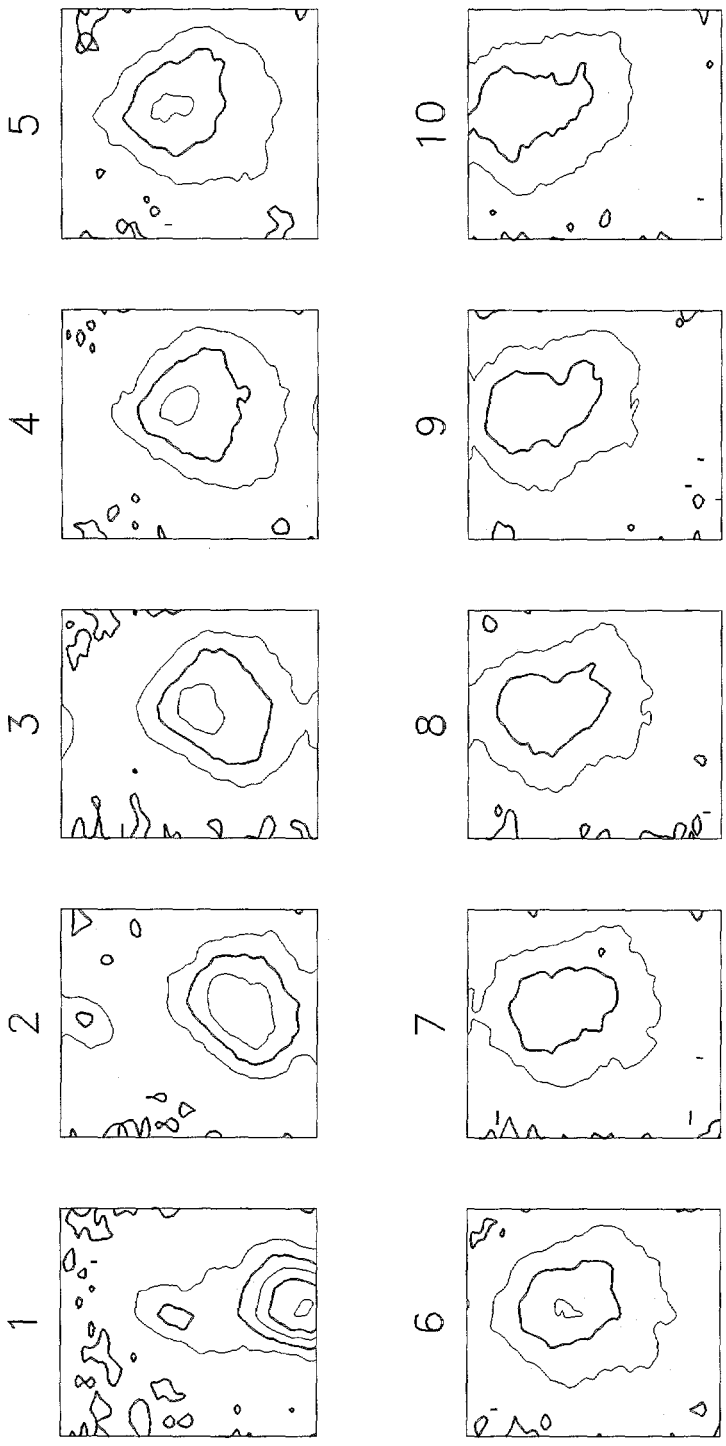

Figure 10. Temporal development of a second-shot plume (the same sample spot as that in Fig. 9). All conditions are the same as in Fig. 9.

the major plume produced by the initial shots, but the fast plume was never observed in case of the initial shots. The fast one may come from desorption of BSA redeposited from the previous event or from released dye molecules. Another explanation of the formation of two plumes could be sample inhomogeneities or having two spots in the desorption laser. However, two plumes were observed even from well-shaped laser spots and visually homogenous films.

The velocities of the larger, slow plumes from the second and subsequent shots were comparable with the velocities of the primary plumes from the first shot. They ranged from 5 to 20 m/s (Fig. 11). The velocities of the smaller, fast plumes were several times faster; they ranged between 30 and 60 m/s. It is important to mention that these velocities were estimated from the positions of the top of the plumes in the second scan (at 150 μs). The instantaneous velocity of the plume drops nonlinearly especially within the first few scans. So, the average velocity can give only a rough idea about the initial velocity.

Laser Spot Characteristics

The plume size is a complex function of all the factors mentioned above. It was very difficult to repeat the experiments under absolutely the same conditions. It was especially difficult to control the spot dimensions of the desorption laser. The simple description of the laser spot in terms of width and length is not sufficiently accurate. No simple correlation was found between the integrated plume

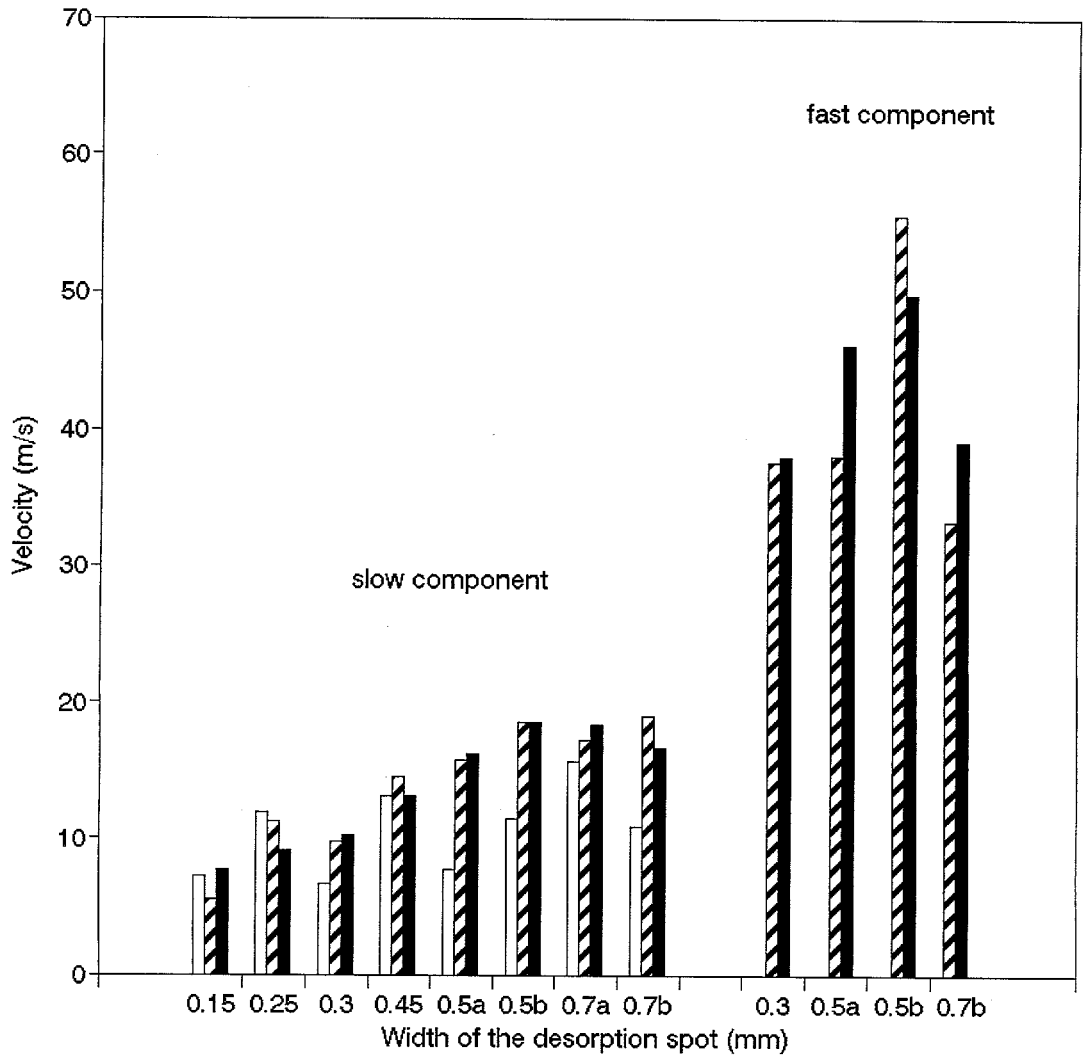

Figure 11. Average velocities 150 μs after desorption produced from several sizes of laser beams. Matrix/analyte ratio, 150; and film thickness, approx. 5 μm. The parameters of the beam spot are given in Table I. Open bars, first laser shots; shaded bars, second laser shots; and solid bars, third laser shots.

absorbance and the desorption spot parameters. The size of the plumes produced for a given laser-beam shape and size, but from different spots on the sample film, showed large fluctuations, especially in the case of the initial shots.

The shape of the desorption-laser spot was changed by insertion of a cylindrical lens. Laser energy was kept constant, but the power density changed because of the different focus. Eight different foci were adjusted (Table I). In order to

Table I. Characteristics of the desorption-laser spots used in Fig. 11

Width (mm)	Length (mm)	Area (mm^2)	Power density (MW/cm^2)
0.15	5.0	0.75	73
0.25	3.0	0.75	73
0.30	6.5	1.95	36
0.45	2.9	1.30	53
0.50 a	2.5	1.25	62
0.50 b	2.3	1.15	53
0.70 a	2.5	1.75	40
0.70 b	1.3	0.91	60

compensate for sample inhomogeneities, plumes from three consecutive shots were measured two to five times for each spot type.

A weak correlation was found between the velocity of the plumes from the second and third shots and the laser-spot width: the wider the spot, the faster the

plume (Fig. 11). One needs to remember that the power density was not kept constant and the entries in Table I are only approximate values estimated from the spot dimensions and the total laser power. The focusing of the nitrogen laser was the least reproducible parameter of the entire experiment. The laser beam profile was far from ideal; even fork-like spots or double spots could be formed at certain focal planes. The description of the nitrogen laser spot in terms of its width and length is therefore only approximate.

Plume Velocities

It is possible to model the development of the plumes in terms of its velocity as a function of time. We can use the centroids of each plume feature from Fig.s 9 and 10 or from 1-D (vertical) scans to determine the group locations of each plume for a given time delay. We make one assumption: the plume velocity will be reduced by a constant factor of C over a distance λ due to collisions with the surrounding gas. The solution for the distance x traveled by the plume with initial velocity v_0 as a function of time t is:

$$x = A \ln(Bt + 1), \qquad (1)$$

where

$$A = -\frac{\lambda}{\ln C} \qquad (2)$$

and

$$B = -\frac{v_o \ln C}{\lambda}. \qquad (3)$$

The instantaneous velocity v may then be calculated according to:

$$v = \frac{dx}{dt} = \frac{AB}{Bt + 1}. \qquad (4)$$

The initial velocity is expressed by $v_o = AB$. It is necessary to keep in mind that both λ and C cannot be determined from the relationships (3) and (4) at the same time; one can determine λ for a specific C (e.g. $C = 0.5$) or C for a specific λ.

The results of the fitting for three separate plumes from the first two laser shots are very good (Table II), although more experiments would have to be performed to confirm the model. Correlation is higher than $r^2 = 0.96$ for all the plumes. There is no systematic deviation between the measured and fitted data. The velocity of the fast plume from the second shot (estimated from the well-defined top edge of the plume) is characterized by a correlation coefficient of 0.999 (Fig. 12).

Extrapolation to determine the initial velocity involves large uncertainties because of the high negative slope at the beginning of the instantaneous velocity vs.

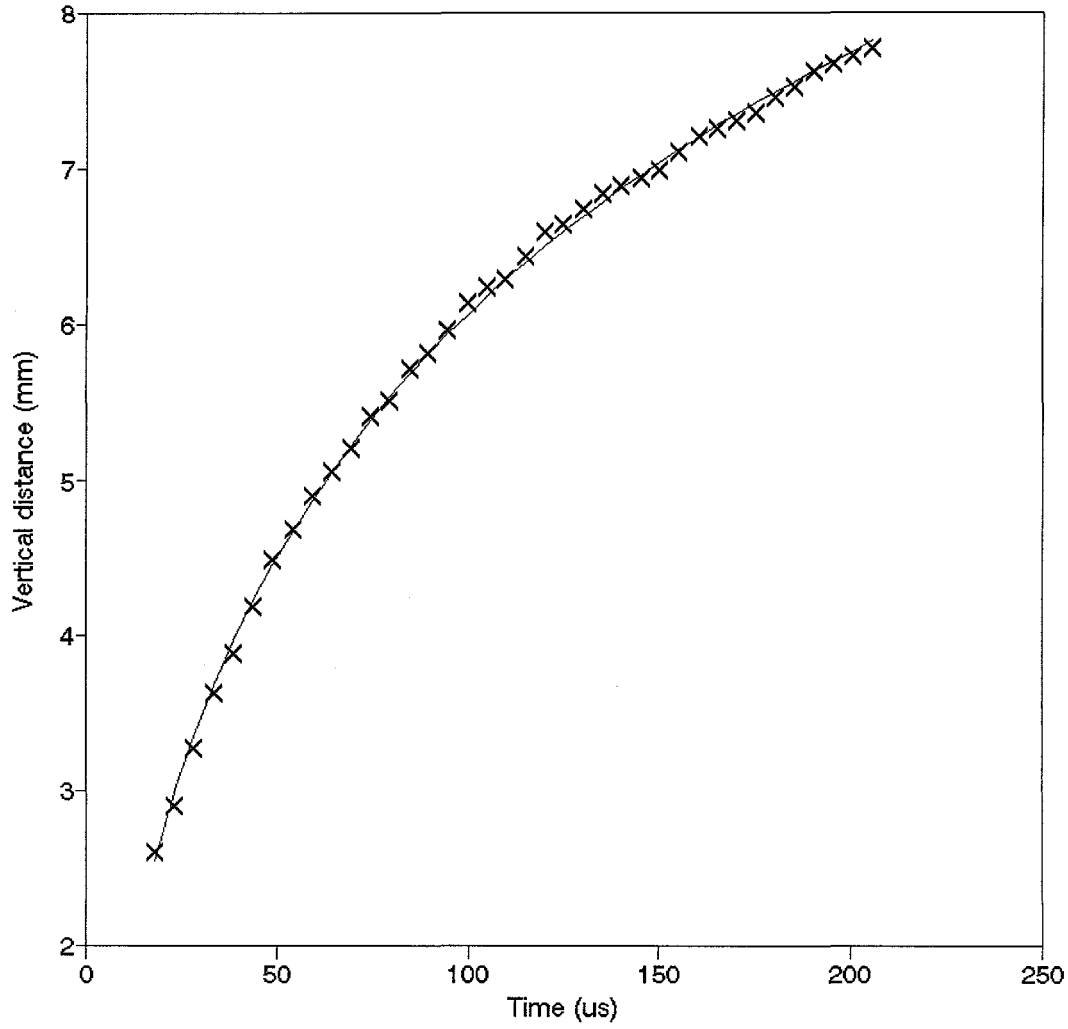

Figure 12. Curve fit of the positions of the fast component of a second-shot plume. Matrix/analyte ratio, 150; film thickness, approx. 5 μm; desorption laser spot, 0.60 × 2.5 mm; power density, 51 MW/cm^2; 1-D scan height, 9.0 mm; and scan rate, every 5 μs. **x**, experimental data, and —, best-fit curve.

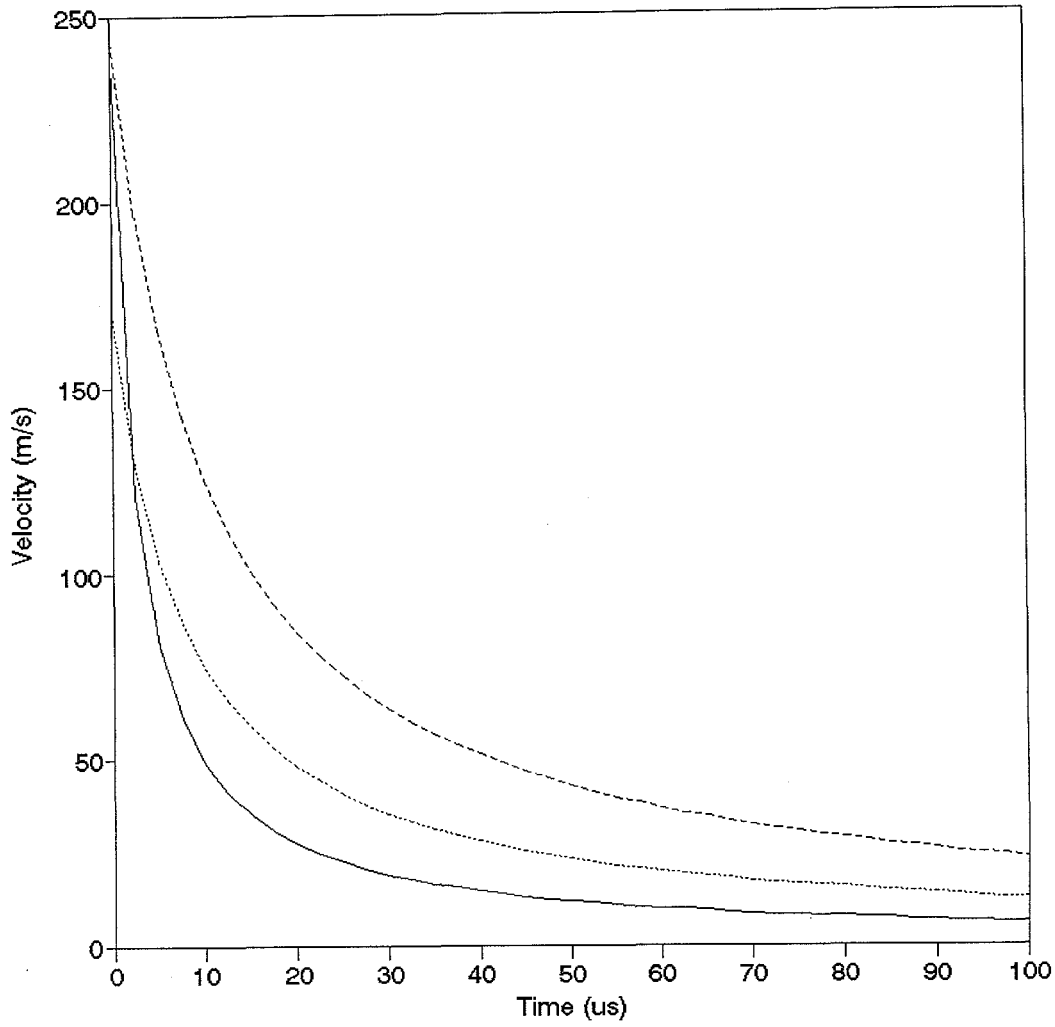

Figure 13. Calculated instantaneous plume velocities for three plume features produced from the first two laser shots. Bottom, first laser shot; middle, second laser shot (slow component); and top, second laser shot (fast component).

time curve (Fig. 13). Even though the fitting parameters in Table II may be determined with satisfactory precision, they are based on the positions of the plume after 10 μs. Therefore, they may not describe other mechanisms contributing to velocity changes of the plume in the very beginning. The accuracy of the initial velocity determination is also highly dependent on the location of the bottom of the scan region from the sample plate, which is difficult to determine exactly. The rough estimates in Table II and Fig. 13 show that the initial velocities of the three plumes do not differ much. These all correspond roughly to the speed of sound.

Table II. The results of fitting the velocities of three plumes to Eq. (1): one from the first shot and two from the second shot

shot (plume)	A (mm)	B (10^6 s^{-1})	r^2	v_o (ms^{-1})	$\lambda_{C=0.5}$ (mm)
1st	0.62 ± 0.01	0.38 ± 0.03	0.996	240 ± 16	0.43 ± 0.01
2nd (slow)	1.3 ± 0.1	0.12 ± 0.02	0.961	170 ± 34	0.93 ± 0.06
2nd (fast)	2.6 ± 0.2	0.094 ± 0.002	0.999	240 ± 5.5	1.80 ± 0.14

Larger differences exist among the calculated values of λ. The fast plume feature from the second shot, which was the smallest of the three plumes, is characterized by the largest value of λ. On the other hand, the plume from the first shot needed the shortest path (λ) to reduce its velocity by 50%. In Table II, the

value of λ appears to depend on plume size. The larger and denser the plume is, the more quickly it slows down as it travels. It reflects group movement of the plume against the friction in air rather than velocity drop of individual molecules colliding with the surrounding gas.

CHAPTER 4. LOW-PRESSURE STUDIES

Instrumental

Stationary beam monitoring. No AODs were used to scan the probe laser beam for measurements in vacuum. The first experiments with absorbance detection were done in a vacuum cell, all other experiments were done in a chamber of TOF MS, which is described below. The sample plate was placed in a cubic vacuum cell with two glass side windows for the probe beam and a top quartz window for the desorption laser beam. The third side window could be used for fluorescence detection in the direction perpendicular to both the probe and desorption laser beams. Two 90-degree prisms were used to vary the vertical position of the probe beam (Fig. 14). The lower prism was fixed to the table while the upper prism was placed on a translational stage together with a lens (330 mm f.l.). A photodiode was placed behind the sample plate and the zero-offset point of the beam to the sample plate was determined as the position at which the measured intensity was reduced (due to blockage) to one half of the original intensity. The maximum (positive) inaccuracy was estimated to be 50 μm, since the beamwaist at the vicinity of the sample plate was 100 μm. This resulted in higher sensitivity and better spatial resolution than in the scanning mode. The optical and electrical setups of the two absorbance channels were the same as in the case of the scanning experiment. Light scattered from the desorption laser pulse followed by

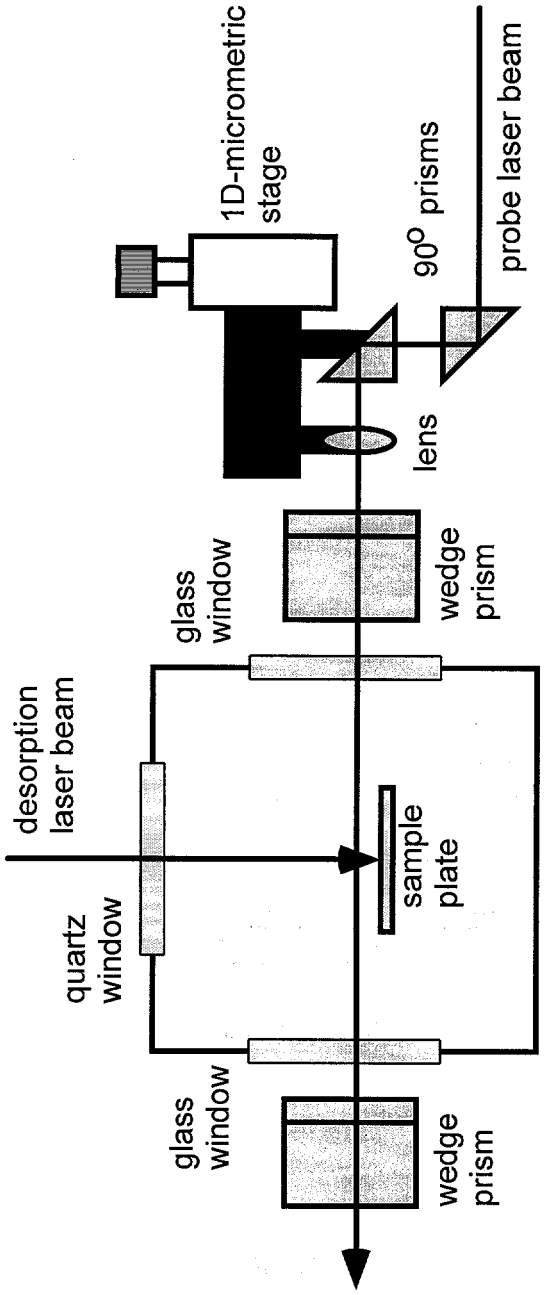

Figure 14. Experimental setup for stationary beam monitoring.

the fluorescence of the sample film caused a false signal during the first 1 μs. This, together with the dc shift discussed earlier, was reduced by digital subtraction of a blank measurement. Alignment of the nitrogen desorption laser was described in the previous chapter.

The time delay caused by the electronic circuits was determined by comparison with the response of a photodiode (Hamamatsu, Model 3399) with low-resistance termination. Because the delay of the amplifier circuit depends somewhat on the magnitude of the amplified signal, the precision of the delay is ± 100 ns. The bandwidth of the data acquisition system was about 1 MHz; the amplitude of the fastest plumes may thus be somewhat reduced.

Mass spectrometer. The TOF MS was a linear Wiley-McLaren type. Probe load mechanism, acceleration optics, flight tube and detector were purchased from R. M. Jordan Co., Grass Valley, CA. The distances between the acceleration plates/grids were 12.7 mm. Both the repeller plate and the extraction grid were powered by two independent power supplies (Spellman, Hauppauge, NY, Model CZE1000R/X2263) which allowed one to optimize the extraction grid potential V_a independently on the repeller plate potential V_b and to detect either positive or negative ions. The maximum accelerating voltage was 15 kV, (V_a of 15.0 kV and V_b of 7.0 - 14 kV was used during the experiments). Higher extraction fields may cause arcing in the case of larger desorbed amount. Lowering the extraction field

decreased resolution. The length of the drift tube was 502.2 mm. 40-mm dual MCP with extended dynamic range offered both excellent ion collection and sensitivity. The distance between the input grid of the detector and the dual MCP element was 15.9 mm. The input MCP had a potential of up to -2.2 kV increasing further kinetic energy of arriving cations or reducing the energy of anions. The instrument was evacuated by a diffusion pump (Varian, Lexington, MA, Model VHS-6) with a maximum pumping speed of 2 400 l/s. The oil contamination of the mass spectrometer was prevented by a cryotrap (Varian, Model 326-6) and a safety electropneumatic gate valve (MDC, Hayward, CA, Model GV-8000V-ASA-P). The ultimate pressure of the system was 1×10^{-8} Torr. A vacuum controller with two thermocouple gauges and one ion gauge was purchased from Granville-Phillips, Boulder, CO, Model 307. A six-way cross with five interchangeable flanges used as the source chamber of the mass spectrometer allowed number of different setups, such as simultaneous optical monitoring and mass spectrometry or implementation of photoionization. A 15-cm S1-UV window served as an entrance for desorption laser beam, probe laser beam or photoionization laser beam. All the beams transmitted through the horizontal plane.

Simultaneous optical monitoring and mass spectroscopy. The nitrogen desorption laser was focused on the probe tip in the MS chamber at an incident angle of 30^{O}. The dimensions of the desorption spot were 0.25 x 1.25 mm. For

absorbance detection, a smaller quartz window positioned off axis on a flange is placed opposite to the large window (Fig. 15). Two wedge prisms were used to reflect a fraction of the light before and after the chamber. A S1-UV lens (25 cm f.l.) was used to focus the probe beam in the plume region. A similar setup of the chamber is used for photoionization; it will be discussed in the next chapter.

For fluorescence and scattering detection, the flange with the small window was placed on the top of the source chamber with its axis perpendicular to both the probe laser beam and the flight tube (Fig. 16). A quartz lens (40 mm diameter, 50 mm f. l.) was positioned between the plume region and the small window to collect light in the extraction region. The distance of the lens from the plume region was 90 mm. The image was loosely focused on the PMT (Hamamatsu, Bridgewater, NJ, Model R980) via the small windows and optical filters. A 488-nm interference filter was used for the detection of scattering. The combination of a 525-nm long pass filter and interference filters transmitting in the region from 500 to 600 nm was used for fluorescence detection. A mirror was placed into the chamber to reflect the probe laser beam out of the chamber and prevent scattering and multiple reflection of the beam. The PMT was equipped with a gating circuit (Hamamatsu, Model C1392-05) to reverse the bias between the photocathode and the first dynode. Thus, the response of the PMT is significantly reduced within 5 μs after the desorption laser pulse. The timing of the experiment (repetition rate, nitrogen laser pulse, gating pulse and oscilloscope trigger) was controlled by a four channel digital delay generator (EG&G PARC, Princeton, NJ, Model 9650).

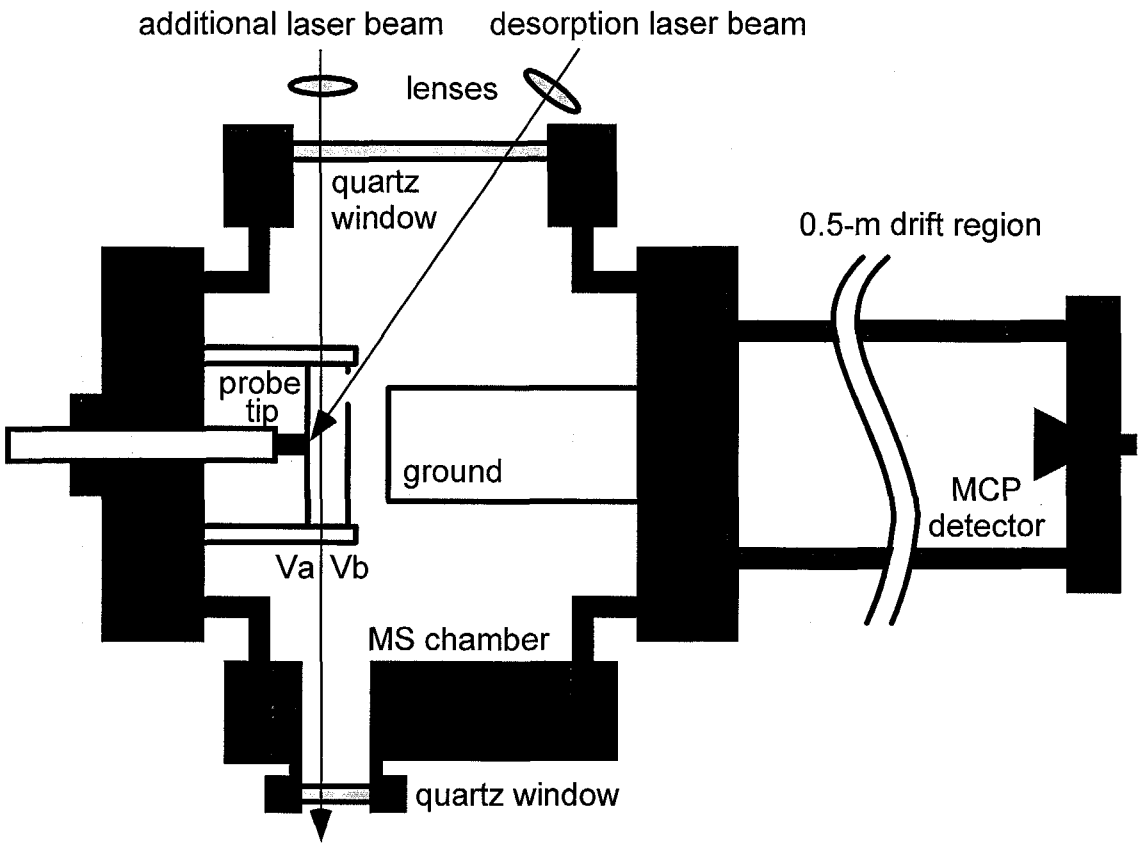

Figure 15. Experimental setup for simoultaneous mass spectrometry and absorbance monitoring (additional laser beam: 488 nm) or photoionization (additional laser beam: 193 nm). Desorption laser beam: 337 nm.

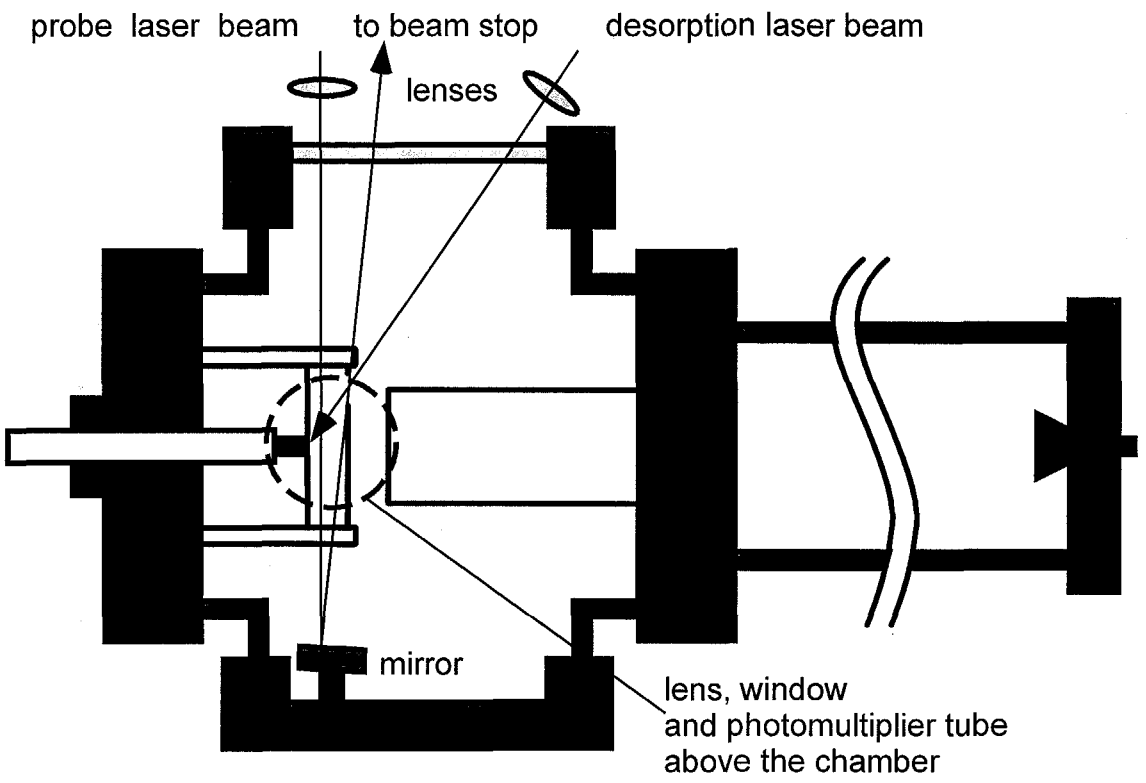

Figure 16. Experimental setup for simoultaneous mass spectrosmetry and fluorescence or scattering monitoring. Probe laser beam: 488 nm, desorption laser beam: 337 nm.

The experiments in this chapter were carried out with a 488-nm, 50 mW argon-ion laser (Cyonics-Uniphase, San Jose, CA, Model 2211-30SL) as a probe laser and nitrogen laser as the desorption laser. Both optical and mass spectrometric data were recorded by a digital oscilloscope (LeCroy, Chestnut Ridge, NY, Model 9350AM) and processed on a computer.

Absorbance Monitoring

As expected, plume evolution at low pressures (which relates more closely to MS) was much faster than that at atmospheric pressure. 1-D or 2-D scanning with our apparatus becomes progressively more difficult, since the plumes typically traveled past a 1-cm distance (scan region) in less than 10 μs. However, a stationary beam can be used to monitor plume evolution. Beam attenuation ΔI is shown in the Figs. instead of absorbance A because of qualitative nature of all experiments in this section.

The temporal evolution of plumes from the first and second laser shots at a distance of 1 mm from the sample plate is shown in Fig. 17 and 18 for several operating pressures. The first laser shot did not produce significant absorption at pressures below 50 mTorr (Fig. 17). A slight response was sometimes observed only when the beam was very close to the plate. This is in contrast to observations at atmospheric pressure (Fig. 9). The second (Fig. 18) and subsequent laser shots produced plumes in which the temporal profiles were comparable; the time delay to

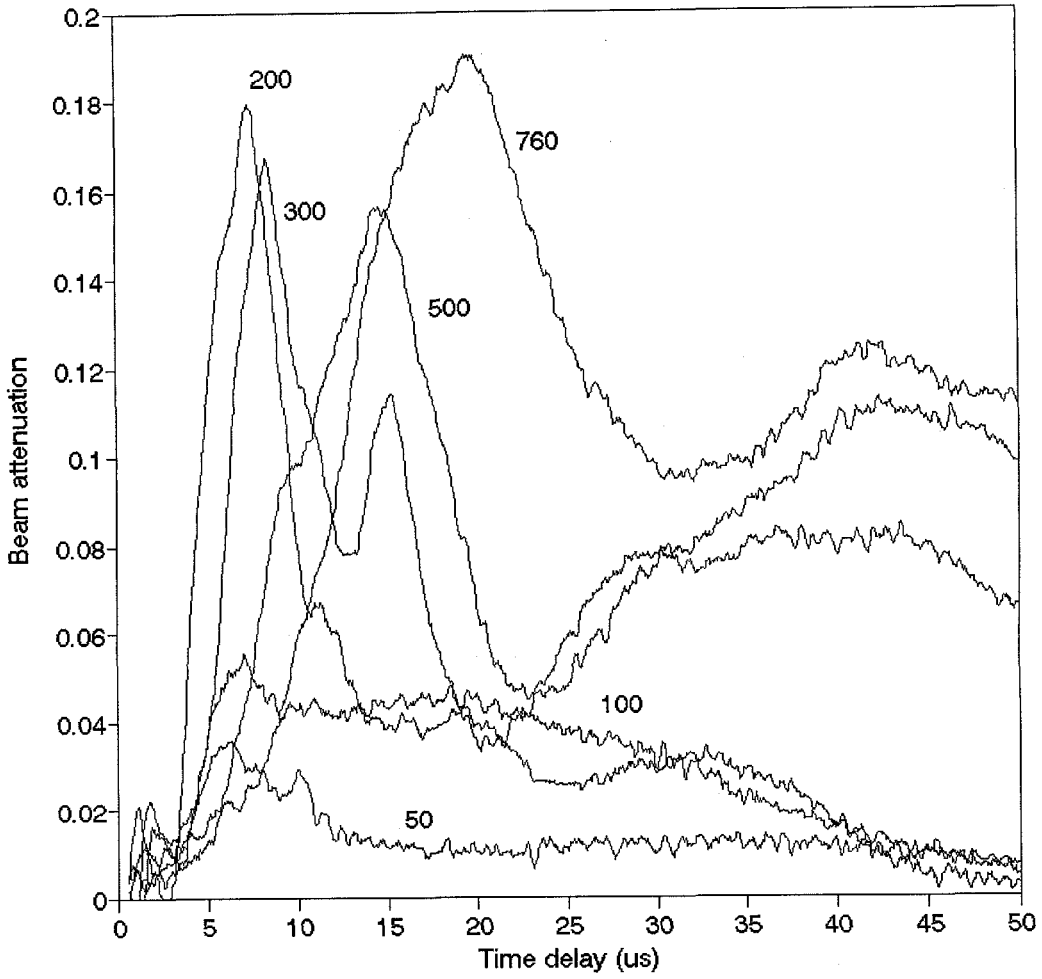

Figure 17. Time evolution of first-shot plumes at several pressures (Torr). Matrix/analyte ratio is 150, and the distance of the probe beam from the sample plate is fixed at 1.0 mm.

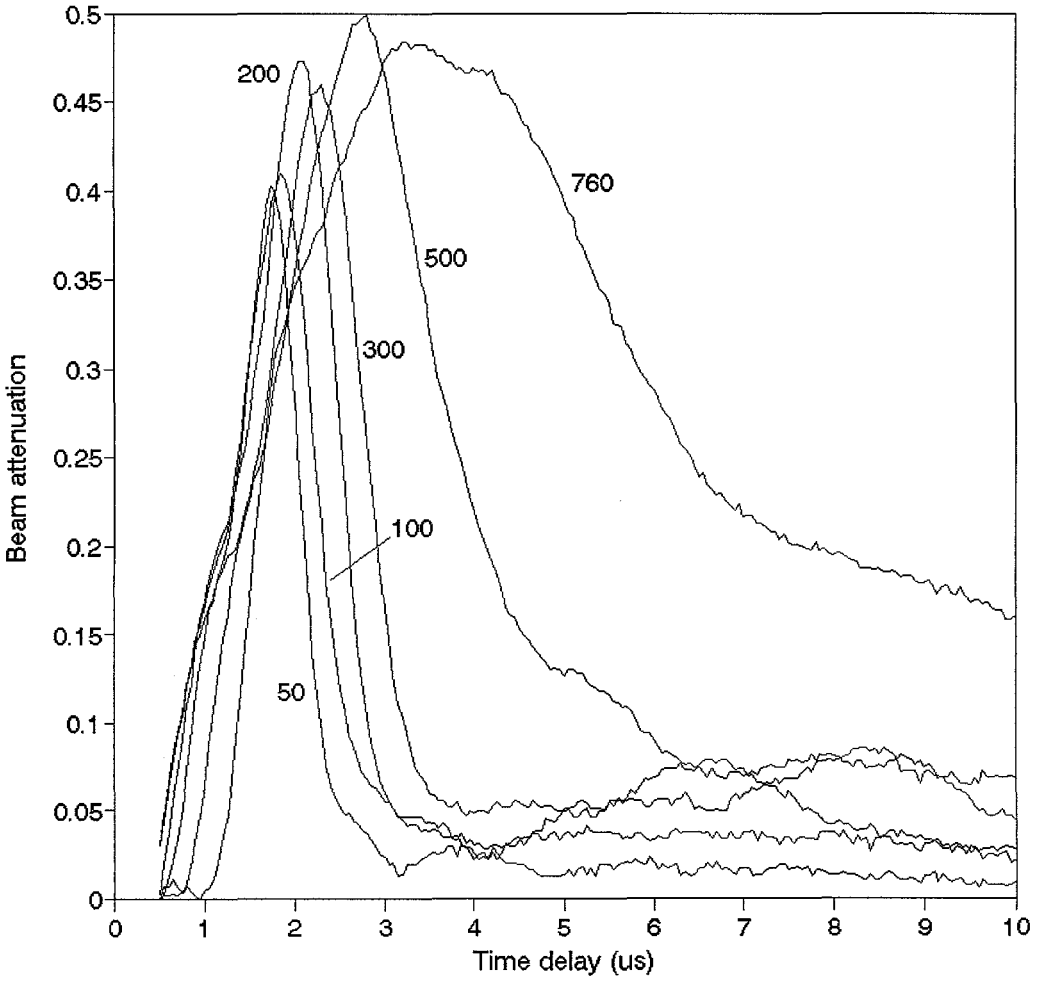

Figure 18. Time evolution of second-shot plumes at several pressures (Torr). Conditions are the same as in Fig. 17.

the peak maximum increased slightly with an increasing number of shots until the film was removed. The removal of the film eventually resulted in the production of several smaller plumes with longer delays. These were probably due to desorption of the film remnants at various locations formed because of the uneven film thickness and nonuniform intensity profile of the desorption laser.

One also notices that the shape of the peaks produced by the first laser shots gave more complex responses (e.g., two peaks) compared to subsequent shots, although scanning at atmospheric pressure showed only one plume at longer time delays. In the case of the second and the subsequent plumes, a simple response was generally observed at low pressures even if the response at atmospheric pressure was complex. Some second and subsequent shots could produce more features in each plume, but those complex responses occurred only at higher pressures (hundreds of Torrs). Further, only if the desorption spot was far from ideal or if the sample film was inhomogeneous could multiple plume features be produced at low pressures.

As expected from radial diffusion (Fig. 9 and 10), the largest absorption response was observed at the beam position closest to the sample plate (at 0.50 mm). With increasing distance the plume expands and the absorption signal becomes smaller and changes more slowly (Fig 19). The plume velocity of the plumes produced by the second laser shots was determined from the plot of the vertical distance versus the time delay for reaching the peak maximum (Fig. 20).

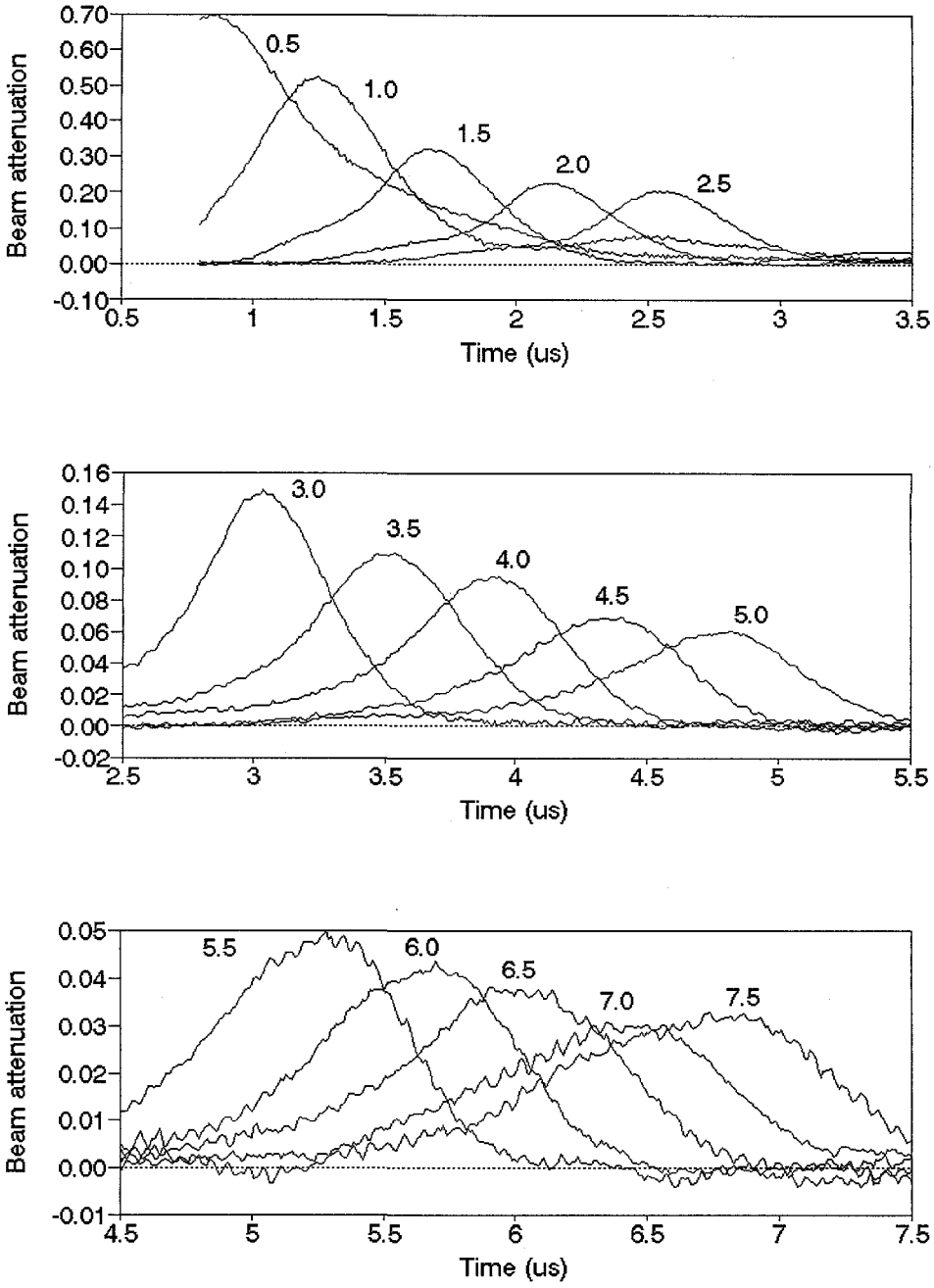

Figure 19. Time evolution of second-shot plumes of BA at the pressure of 20 mTorr. The distance of the probe beam from the sample plate (mm) is given in the graph.

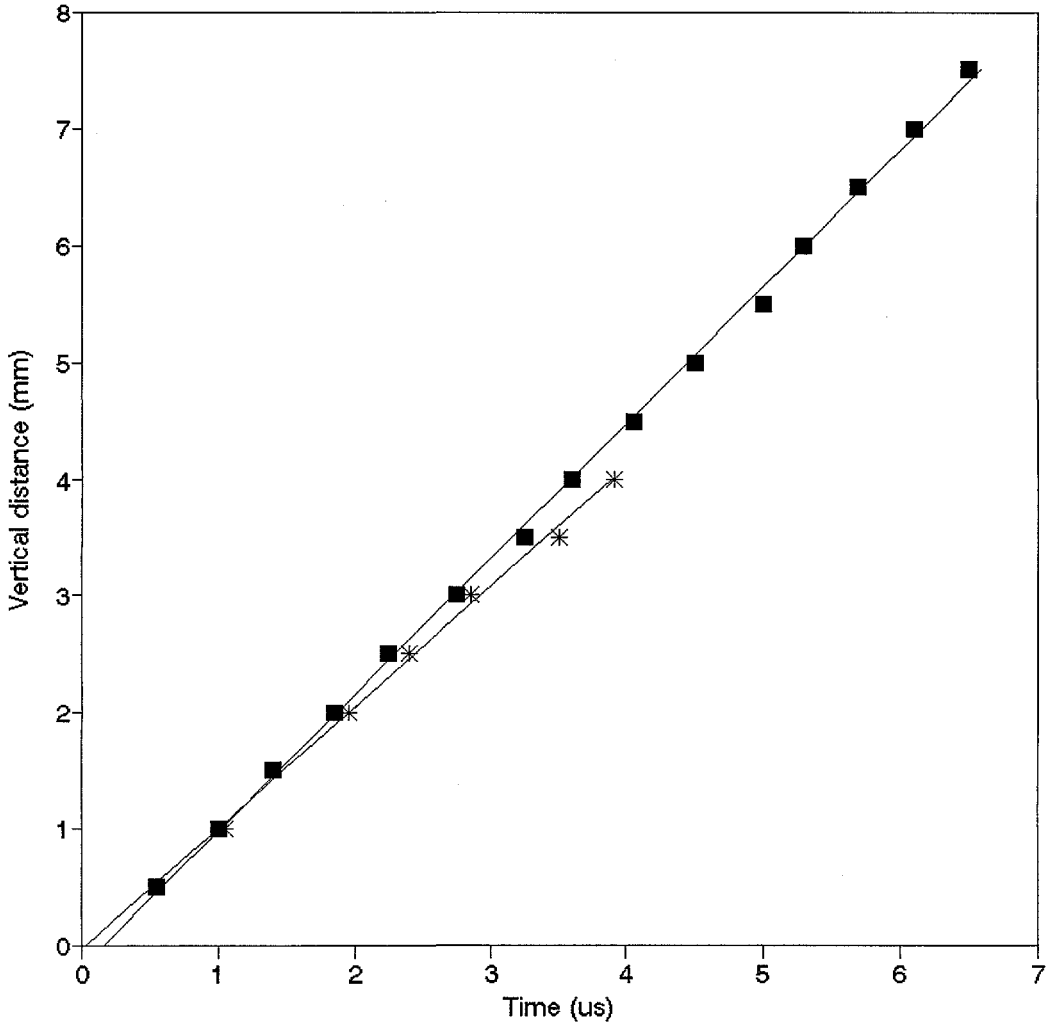

Figure 20. Distances traveled by second-shot plumes versus time at 50 mTorr for 2 different sample films. Matrix/analyte ratio, 150; film thickness, approx. 5 μm; and desorption beam size, 2.5 × 0.25 mm.

The graph is linear, which means that the plumes moved at constant velocity within the range of distances studied. This is in contrast to motion in air (Fig. 12). The small nonzero intercept is indicative of a small error in determining the zero distance or time delay. The velocity may be determined with very good precision, i.e., a very high correlation between observation height and time delay is evident in Fig. 20, despite the fact that data from several different spots had to be combined to create the plot. The two experiments were done on different areas of the film, with the spot shape and laser energy almost unchanged. The resulting difference in plume velocities was only slightly larger in comparison with the individual standard deviations. The second-shot plume velocities were 1165 ± 10 m/s and 1034 ± 22 m/s (correlation of $r^2 = 0.999$ and 0.997, respectively), which were towards the high range of those reported in the literature. The discrepancies between our measured velocities and the literature results may stem from different conditions (higher power density, larger desorption spot in our case) or from the fact that the earlier measurements of velocities were with mass spectrometers, which might be easily influenced by local electric fields, high-voltage pulse generation delays, etc.

Fluorescence Monitoring

Some of the experiments with the absorbance detection mode were carried out in the source chamber of the mass spectrometer. There were two major expectations from this experimental design. First, optical information would be

supported by the additional mass spectrum acquired from the same laser shot. Second, the ratio of ionized to neutral analyte would be estimated from the absorbance signal. None of those aims was achieved. A large amount of analyte had to be desorbed because of the low sensitivity of absorbance measurements. This often led to arcing and space charge effects which prevented us from recording useful mass spectra. It was already mentioned that the fraction of ionized analyte molecules may represent only about 0.01 % of all desorbed molecules. Low sensitivity of absorbance detection did not allow detection of any splitting of original desorbed plume into two plumes in the presence of an extraction electrical field.

Detection of fluorescence instead of absorbance might be the answer to the difficulties associated with low sensitivity. Fluorescence is characterized by 3 to 6 orders lower detection limits than absorbance. Disadvantages of fluorescence detection are necessity of elimination of background light and worse reproducibility. In our case, the high background was the main drawback of this detection scheme. Several sources contributed to the background light:

1. 337-nm desorption laser pulse,
2. 488-nm scattered light and
3. fluorescence of the sample film excited by the desorption laser pulse.

The first two sources of the background light were efficiently filtered out by a 525-nm long pass filter. Gating of the photomultiplier also prevented its saturation by the 337-nm light and strong fluorescence from the sample film during first 5 μs. The

main source of the background light was identified as the slow decay of the fluorescence of the sample film excited by the desorption laser pulse. The highly reflective environment (of the source chamber) reduced the effectiveness of a shielding cone and an aperture which were used to eliminate the direct fluorescence from the sample film. Emission spectra of the analyte in condensed and gaseous states are probably very similar, so the use of optical filters to eliminate this source of background light is not a solution.

Scattering Monitoring

The monitoring of scattering was already used in the study of laser desorption. Scattering detection was the only fruitful approach because the detection bandwidth might be limited to a single wavelength. A single 488-nm interference filter reduced the background light sufficiently; the contribution of 488-nm light scattered from the chamber walls and the contribution of fluorescence were diminished. Yet, the background subtraction had to be made.

All experiments were done with thick films of a mixture of insulin and ferulic acid (matrix-to-analyte ratio 1:100). Typical scattering from 488-nm probe beam positioned at the distance of 1 mm from the probe tip is shown on Fig. 21. The major response occurred within 40 μs after the desorption pulse, followed by infrequent isolated peaks. One can calculate the size of the particles responsible for some well-defined peaks; the diameters of the particles may be as large as 100 μm. 50

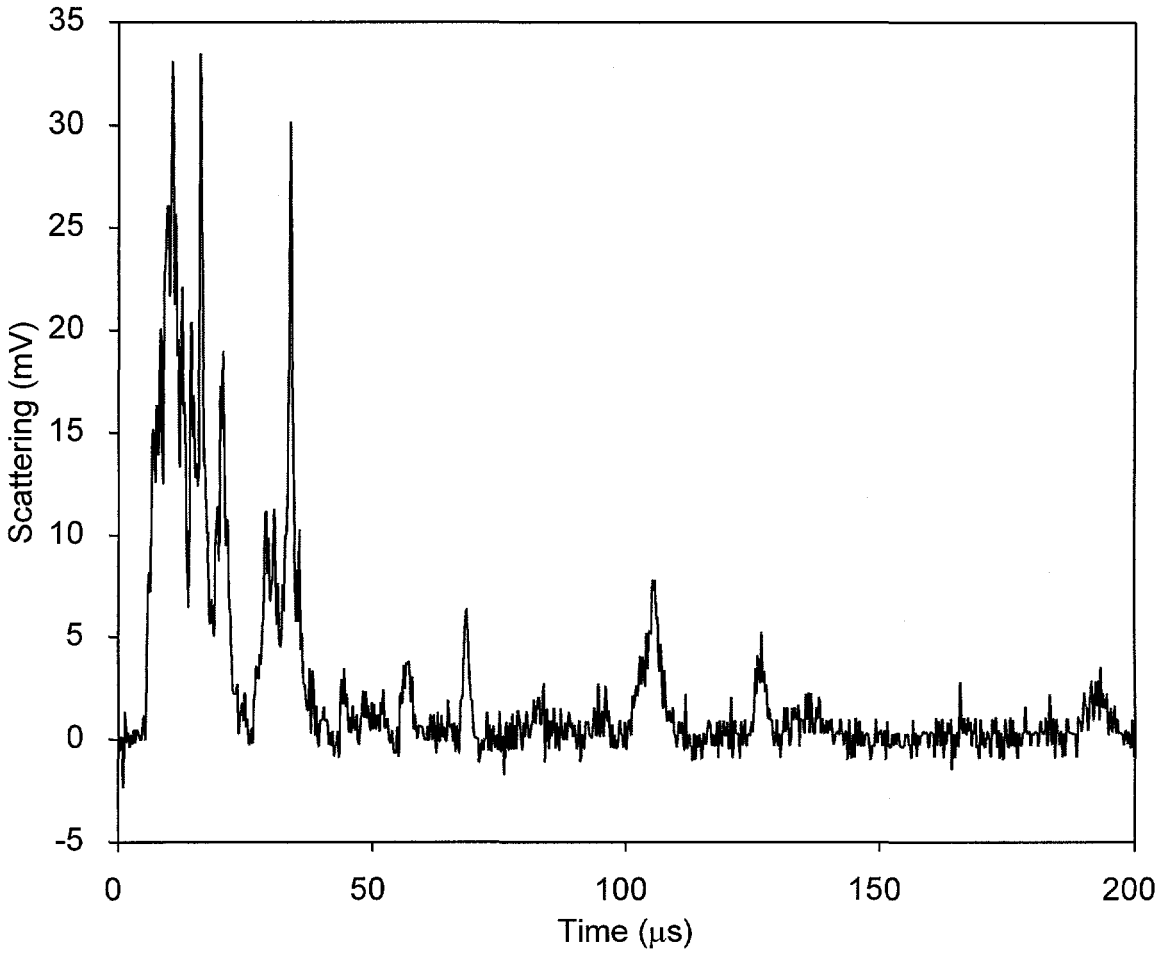

Figure 21. Scattering signal produced by a single-shot desorption of insulin-ferulic acid film. Matrix/analyte ratio, 100; desorption beam size, 1.5 × 0.25 mm, power density, 58.1 MW/cm^2, distance of the probe beam from the probe tip, 1.0 mm, background subtracted.

desorption laser shots were applied to a single spot and the scattering response from each shot was integrated over 200-μs interval. Most particles were ablated by the first 30 laser shots. The decrease of scattering was not unambiguously related to the total film removal from the spot. At low power densities of the desorption laser the scattering signal could disappear although there was still remaining material on the desorption laser spot. Only loosely bound crystals were probably disconnected from the probe surface. The total scattering from a spot (sum of integrated scattering signals of 50 shots) is related to the desorption laser power density (Fig. 22). In order to reduce the effect of possible film variation over the surface of the probe tip, three experiments were done for each power density. As expected, higher power density resulted in a linear (r^2 = 0.987) increase of scattering.

It is interesting to compare the scattering data with mass spectra from the same sample. The insulin peak appeared in the mass spectrum at the first shot at low desorption power density (the two upper traces in Fig. 23). The repetition rate was 6 Hz; peak area was calculated from an average of 30 spectra. Maximum response, however, was reached after a certain time. With increasing power density, the insulin peak was absent at the beginning and emerged after approximately one hundred shots (other traces). It is important to mention that the peak shape and the time of the flight of insulin changed during time. The peak became narrower and the time of the flight shifted to lower values. These effects can be caused by uneven light power density over the desorption spot. The total

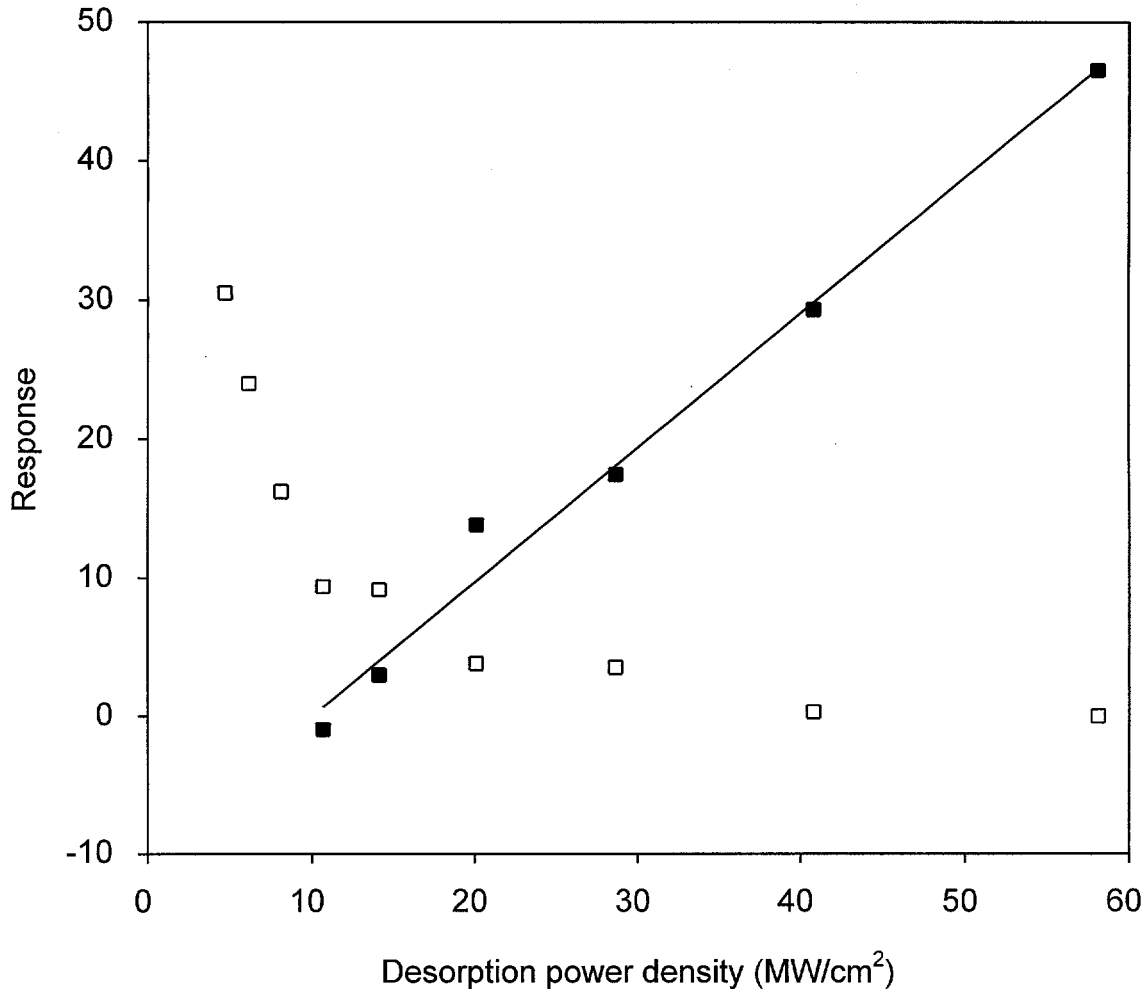

Figure 22. Correlation of total scattering (■) and total detected insulin (□) with desorption power density. All conditions are the same as in Fig. 21.

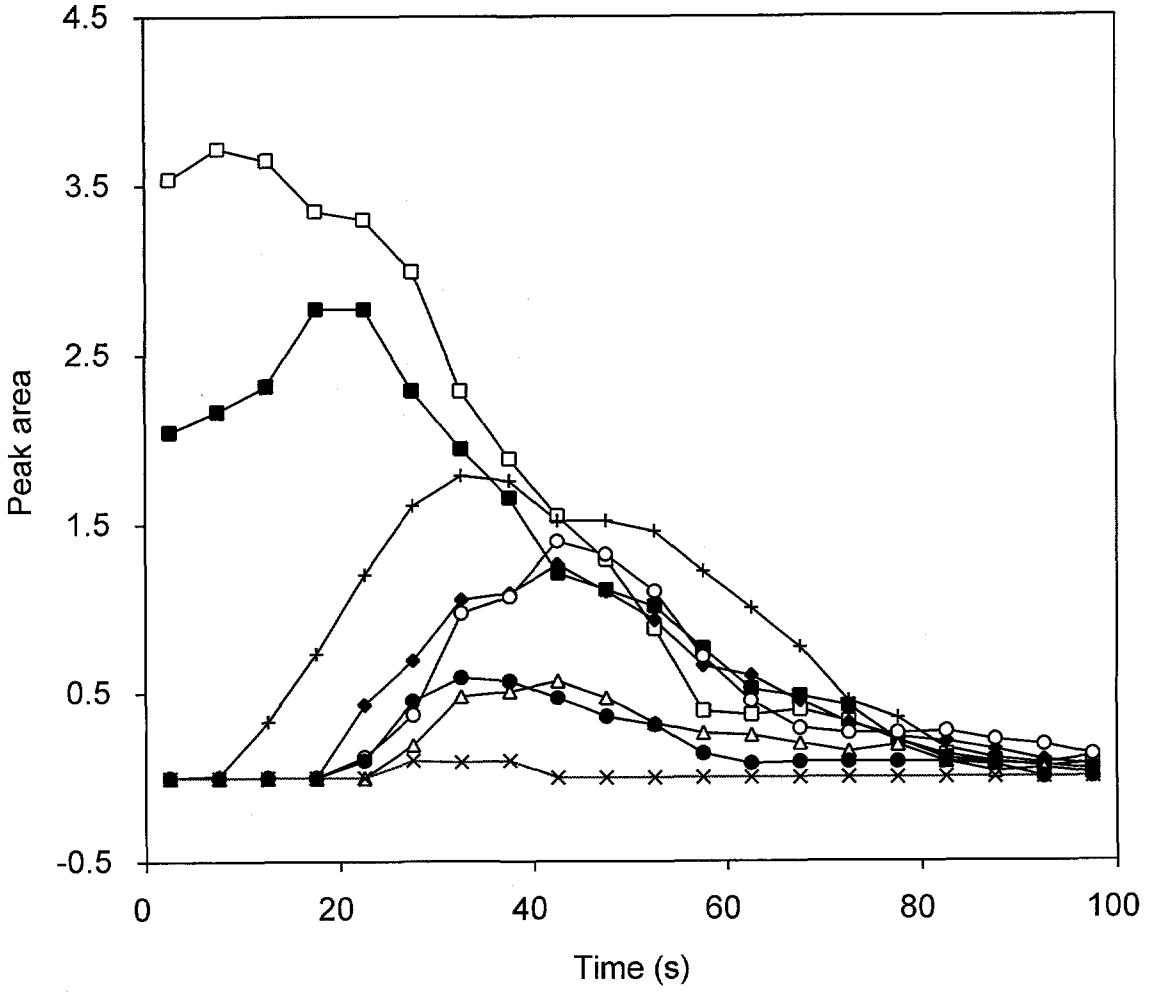

Figure 23. Time evolution of insulin peak area at 8 different desorption power densities: □, 4.71; ■, 6.16; +, 8.13; ◆, 10.6; ○, 14.1; ●, 20.1; Δ, 28.6 and **x**, 40.1 MW/cm^2. Each point corresponds to an area of insulin peak determined from an average of 30 mass spectra. Repetition rate, 6 Hz.

insulin detected during 100 s is shown in Fig. 22 as a function of the desorption power density.

The effects of the desorption power density on the MALDI-MS were often discussed in literature. The best results are obtained at the power density just above threshold for the desorption. Larger power densities lead to higher deposition of energy into analytes, causing their fragmentation, which results in occurrence of more peaks and peak broadening. Applying too high energy to a spot may also result in the desorption and ionization of a large number of molecules and hence space charge effects.

Spallation, ablation of a bulk material, may be another reason why the high power densities are harmful for MALDI. Released particles may distort the extraction electric field or cause pressure gradients (evaporation from particle surface) and hence deflect the analyte molecules from the path to the detector. There are several reasons why we think the production of particles and quality of mass spectra are related. First, the use of high energy favors the production of particles but not the total amount of detected analyte. Second, the insulin peak appeared after tens or hundreds of shots. The spallation was most apparent during first 30 shots or so. Our probe could only detect a fraction of the particles and might not be sensitive enough to detect smaller particles. Some particles were probably released even at power densities below 10 MW/cm^2 giving good explanations for the low initial increase of the insulin peak. Third, desorption of large amount of material

and space charge effects cannot explain all these effects. 600 desorption pulses at the power density between 10 and 30 MW/cm^2 did not remove all the sample from the spot.

This theory does not offer a remedy to overcome the difficulty; the proper sample preparation is already known to be one of the key problems of MALDI. However, the scattering detection could be used for independent evaluation of the sample film quality.

CHAPTER 5. PHOTOIONIZATION EXPERIMENTS

Instrumental

All photoionization experiments were done with a 337 nm N_2 laser as the desorption laser and 193 nm excimer laser (Lumonics Inc., Kanata, Ontario, Canada, Model HyperEx-460-HR-A) as the photoionization laser. All experiments were done in the chamber of a mass spectrometer. The geometry is similar to that of absorbance experiments (Fig. 15). The distance of the desorption spot from the ionization spot was larger than 0.5 mm, exact values are given in the text. In order to reduce the laser irradiances, quartz plate was used instead of a mirror and a variable number of quartz plates were inserted into the beam paths. The rectangular beam of the excimer laser offered better focus in the vertical dimension. The combination of two mirrors or a mirror and a quartz plate was used for 90^{O}-rotation of the laser beam and better focus in the horizontal dimension. This geometry was used for measurement of time delays to minimize the overlap of the desorbed plume with the excimer beam on the desorption axis. Simple geometry (no rotation) and loose focus (1 x 4 mm) was used in the most sensitive measurements.

The voltage on the repeller plate (V_a) was kept at 15 kV, the voltage on the extraction grid was 13.25 kV unless otherwise noted in text. The delay between the desorption and photoionization pulses, oscilloscope (LeCroy 9350AM), trigger and

repetition rate were precisely controlled by a four channel digital delay generator. One channel of the oscilloscope was used to record the MS signal (2 ns-resolution), the other was used to record the signal of a fast photodiode to verify the time delay between the pulses of the two lasers. If maximal resolution or detection was needed, the oscilloscope was triggered directly by a photoionization pulse by the photodiode. Other experimental conditions were the same as in the previous chapter.

Photoionization of Aminoacids and Small Peptides

A typical LD-RMPI spectrum of an aminoacid valine is shown in Fig. 24. Only one major peak is produced according to the reaction

$$(NH_2)RCH - COOH \rightarrow (NH_2) = CH - R + HCOO^{\bullet} + e^{-}$$

in agreement with previous work.[74, 76, 91] Formation of small nonspecific fragments was not observed at the photoionization power density of ~1 MW/cm^2. The lower-mass peak corresponds to Al^+ from the probe tip. Desorption power density was 4.7 MW/cm^2.

Infrared LD combined with 266-nm photoionization may serve for analysis of PTH-aminoacids from Edman degradation.[68] If other aminoacids showed similar sensitivity and simplicity of its MS signal, a new, alternative way could be used for the analysis. Terhorst et al. examined 20 aminoacids by 193-nm PD SNMS. They

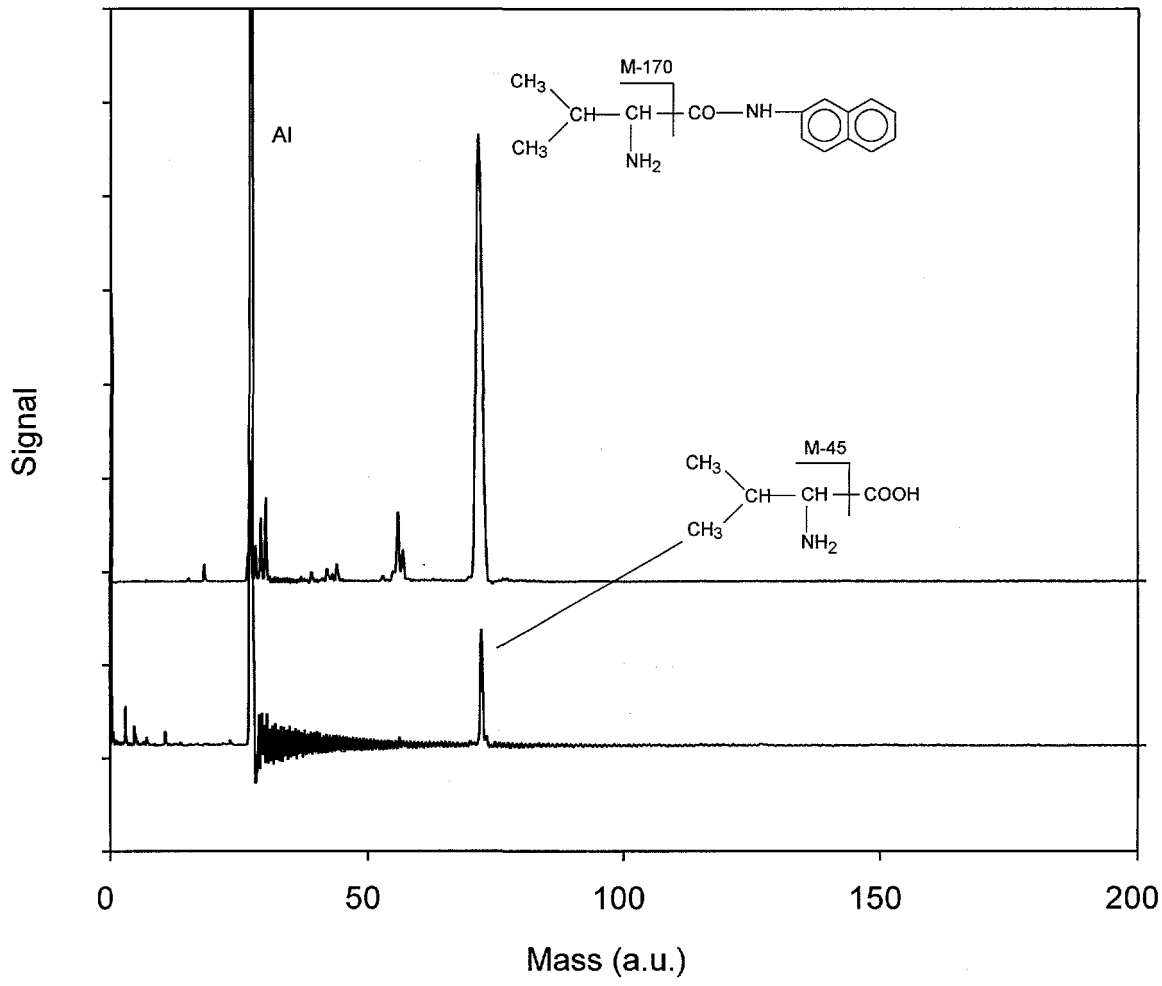

Figure 24. LD-RMPI mass spectra of valine (lower trace) and valine naphtylamide (upper trace) desorbed from aluminum tip. Desorption power density, 4.7 MW/cm^2, photoionization power density, ~10MW/cm^2, spot-spot distance, 1.0 mm, shot-shot delay, 2 μs.

found tremendous differences in relative signals from different aminoacids.[74, 76] It cannot be estimated, however, what differences will be introduced by substitution of SNMS by LD. Unfortunately, the occurrence of the $(M-45)^+$ fragment was found to depend strongly on the type of aminoacid. For some aminoacids another fragment can be used, such as $(M-74)^+$ for of tryptophan; several aminoacids, however, do not dissociate to any useful fragment ion. Moreover, the PTH-derivative of valine does not photodissociate to the $(M-45)^+$ fragment ion.

Three peptides were selected in order to test the fragmentation patterns of the ionization. Val-Leu as an aliphatic dipeptide, Val-Phe and Phe-Val as dipeptides with an aromatic center. The most pronounced fragment ion is the ion from the N-terminal group. Thus, the signal of the valine fragment ion is stronger than the signal of phenylalanine in case of Val-Phe and the opposite is true for the peptide Phe-Val. The signal of the valine fragment ion from Val-Phe is also stronger than the one from Val-Leu ion. This is probably related to better coupling of 337-nm desorption via phenylalanine. All these results are in accordance with previous work except one important difference: no formation of adducts, such as $(M+H)^+$ or $(M-Na)^+$ was observed.

Enhancement of Sensitivity and Resolution

The formation of ions is exclusively based on the photoionization. A highly efficient photoionization step makes up for nonresonant LD. There are two approaches towards sensitivity increase (without changing any wavelength).

First, we made the desorption procedure more efficient. An obvious way is to incorporate a matrix, which would turn LD into more efficient MALD. There is a hidden trap in this approach. Since we want to detect ions with masses on the order of hundreds a.u., a strong signal of matrix and its fragments will significantly complicate the region of mass spectra of our interest. Even with the reduction of matrix-to-analyte ratio to ~10 or regulation of photoionization power density did not improve the quality of the spectra. Matrices, like ferulic acid, undergo more efficient ionization and photodissociation than aliphatic aminoacids. Another enhancement of the desorption step can be realized by direct labeling of the aminoacid with an aromatic label. We compared efficiency of LD-MPI of several common labels (Fig. 25). Both C-terminal labels (valin-nitroanilide and VNA) and N-terminal labels (dansyl-valine) show at least a 10-fold increase in sensitivity. In all cases, the $(M-45)^+$ remained the prevalent ion in the spectra. Finally, a relatively large desorption spot (~0.4 mm^2) increased the desorbed amount of analyte.

Second, we optimized the photoionization step. This means not only proper adjustment of the photoionization power density but also irradiance of as many neutral ions as possible. Satisfactory overlap of the photoionization beam with the

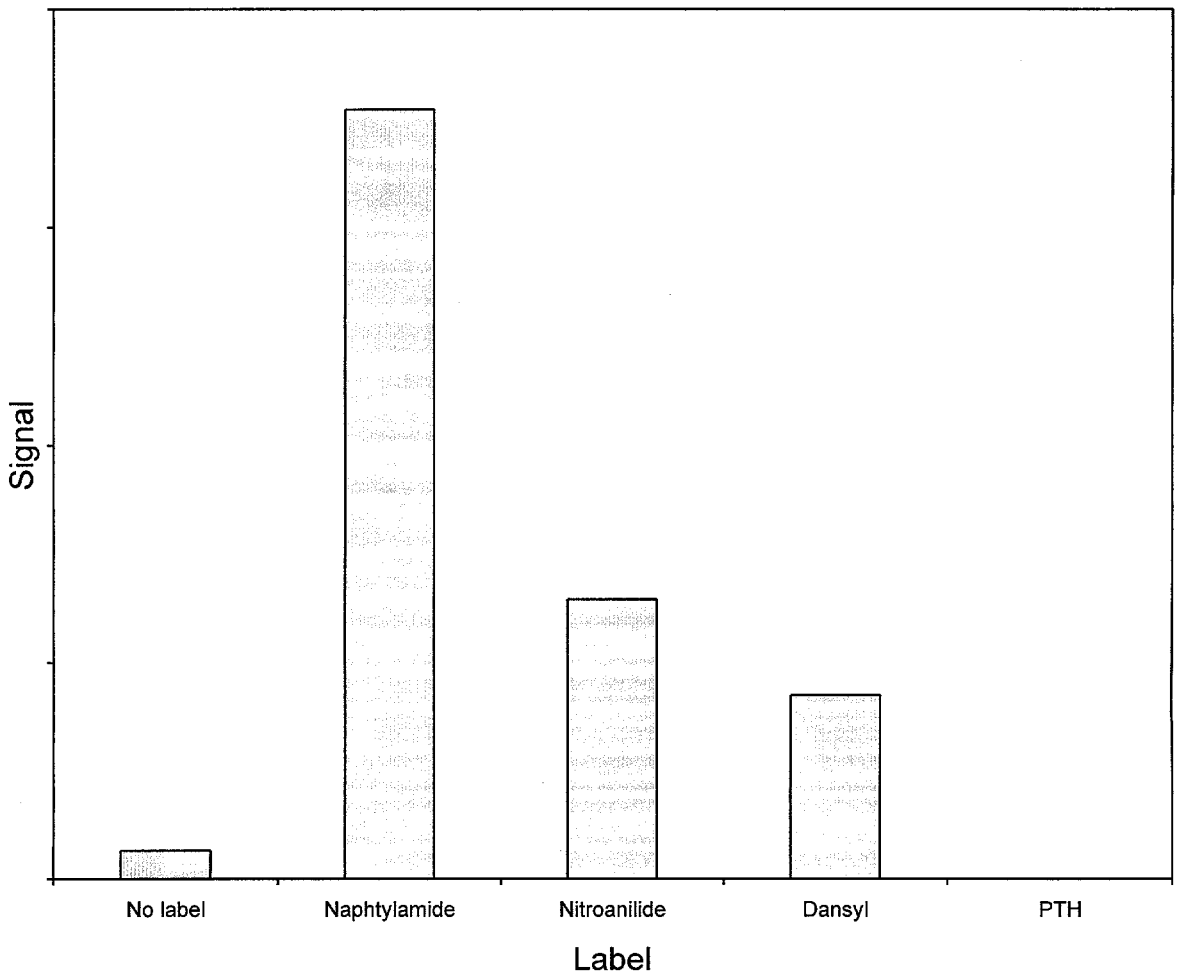

Figure 25. Height of valine daughter peak (M = 71.1 a.u.) for several label types. Conditions as in Fig. 24.

plume of neutrals could not be usually accomplished or it is neglected. Resolution has to be as high as possible at the same time because of its direct relation to sensitivity. We want to demonstrate that the optimization of the sensitivity (function of power density and spatial overlap) and resolution may be achieved simultaneously.

In order to measure the temporal development of the plumes, the beam was focused to a ~100 μm wide spot at a distance of 1.2 mm from the desorption spot. Temporal evolution of three plumes is described in Fig. 26. As expected, the time delay is dependent on the energy absorbed from the desorption pulse. Decrease of the desorption power density leads to a shift in temporal distribution towards longer times (curves ■ vs. □). The same result was obtained if valine is used instead of VNA (curves ■ vs. ●). The long tailing is a result of an increase in the velocity interval related to the finite focus with time. The temporal distribution may be transformed into a normal spatial distribution. Under usual conditions only a narrow "slice" of the entire plume is excited. It can be estimated to ~10 % in our case. Specific time delay is also optimal only for a specific compound. On the other hand, the photoionization volume limited by a tight focus in the direction TOF substantially eliminates the velocity spread by selection of molecules with a narrow velocity distribution. Since the spatial spread is reduced by the desorption from a plane and the temporal spread is assumed to be determined by the pulsewidth of the desorption laser this geometry is characterized by a high resolution.

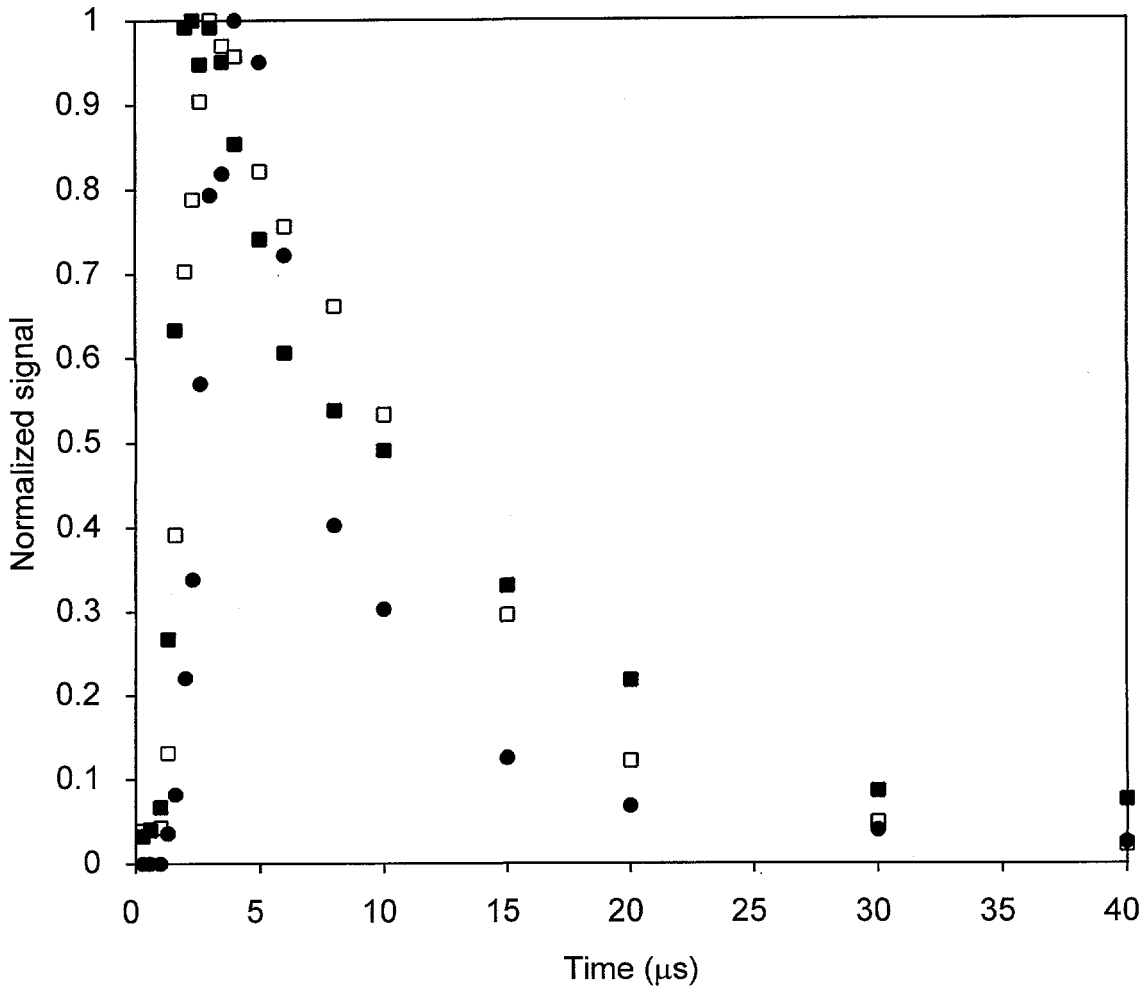

Figure 26. Arrival profiles at spot-spot distance 1.2 mm. Compounds and desorption power densities: valine naphtylamide, 4.7 MW/cm^2 (■) or 1.8 MW/cm^2 (□) and valine, 4.7 MW/cm^2 (●). Photoionization power density, ~10MW/cm^2, photionization spot width ~0.1 mm.

The halfwidth of the spatial spread is approximately 2 mm. Thus, we can ionize absolutely the majority of the plume with a loose focus (1 x 4 mm) at time of 5 μs. The combination of photoionization with desorption is analogous to the popular time-lag focusing method. Instead of a delay between the desorption and extraction of existing ions with an electrical field, the ions are *formed* at a certain time after the desorption of neutrals. Presumably, the photoions are characterized by the same velocity distribution as their precursors. Ideally, all neutral species are irradiated by the photoionizing light. The velocity and the position of the ions are correlated as in the case of LD/I. There are some differences between the two delayed extractions. A certain minimal distance between the photoionization beam and the sample, say 0.5 mm, must be maintained to prevent its interaction with the condensed sample. The time delay between the two laser pulses cannot be shorter than 1 μs to achieve satisfactory overlap of the plume and the photoionization beam. Also, the intensity of the excimer laser is not constant over the ionization region. The biggest advantage, however, is the instant ionization depending on the laser pulsewidth. Application of a voltage pulse is complicated by the limited response of the electronic circuit, ringing, limited voltage of the pulse and technical difficulties like the isolation of the generator from ground.

In order to verify this concept, the voltage on the extraction grid, V_b was varied at constant repeller voltage, V_a = 15.0 kV. The optimal range of V_b was between 13.0 and 13.5 kV. In our case, peakwidth (full width at half maximum) of

the VNA peak was limited by the pulsewidth of the excimer laser. The minimum pulsewidth of VNA peak of 10 ns was in agreement with specified and measured value for excimer peak. The detection limit of VNA was in the subfemtomole region (concentration below 0.1 μM).

LD-RMPI of VNA from PA Gel

VNA was chosen for preliminary studies of LD-MPRI because of its excellent response. Linear PA was used as a model matrix due to easy sample preparation. We assume the substitution of linear PA with cross-linked PA will not have significant effect on the desorption and may be done in our future practical experiments. Two types of samples were tested. First, we let the deposited volume dry at room temperature and atmospheric pressure ("dry" sample). The sample appeared to be homogenous and did not shrink. Second, we put the sample into the vacuum chamber immediately after the preparation ("wet" sample). We were able to obtain mass spectra 1 minute within the sample exposition to vacuum. The pressure climbed up to 10^{-5}-Torr region due to water evaporation and then slowly returned to normal $1x10^{-7}$ Torr. Under low pressure, all water was removed from the sample within several minutes and an uneven crust of gel was formed. We did not find major differences between spectra obtained from dry and wet samples. Spectra of 50 μM VNA in 5% PA gel and 5% PA gel alone (both dry) are shown on Fig. 27. For comparison, spectra obtained without gel are also shown. Clearly, the strong signal of the VNA daughter ion dominates the spectra. The strong signal of Al^+

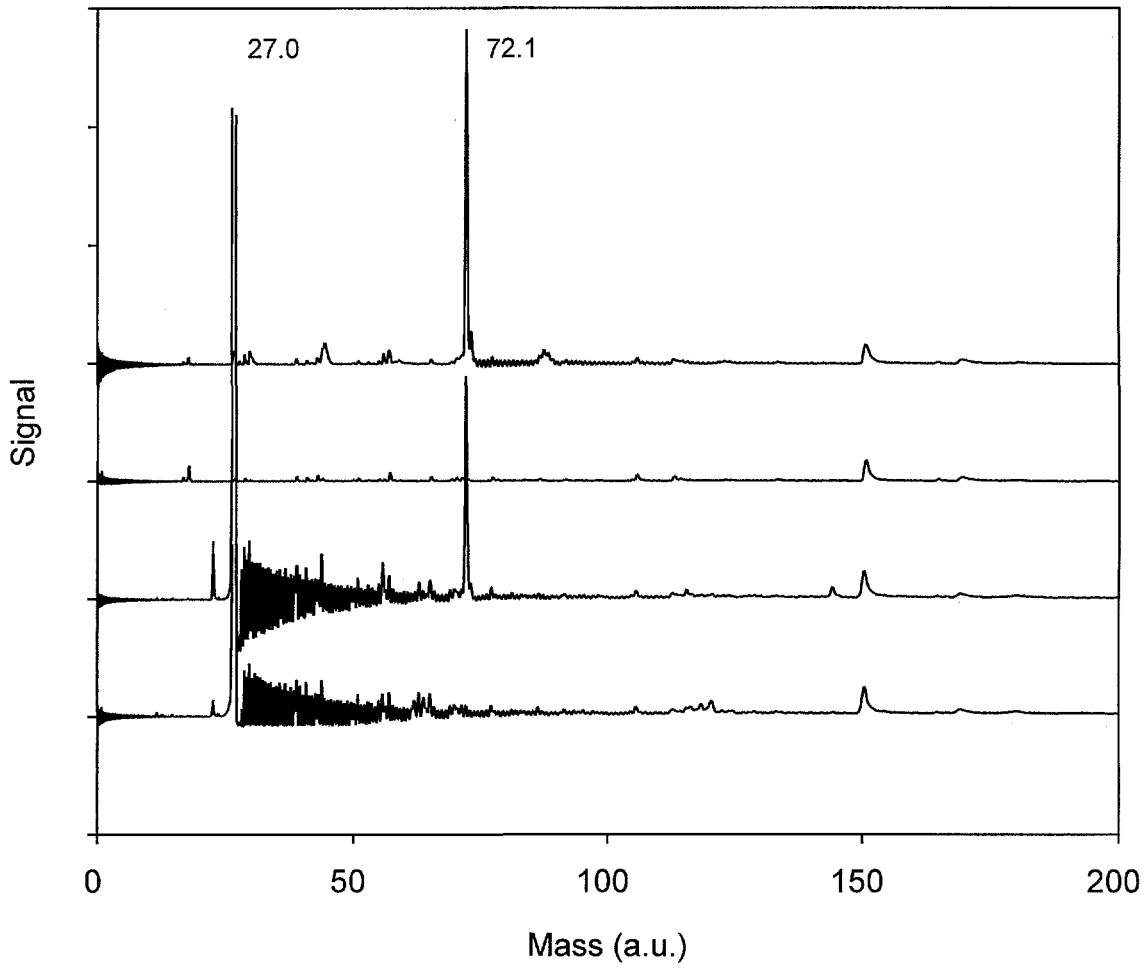

Figure 27. LD-RMPI from PA gel and Al. From bottom to top: Al, VNA on Al, PA gel (dry), VNA in PA gel (dry). Shot-shot delay, 5 μs, spot-spot distance, 0.5 mm, photoionization spot: height,1 mm, width, 4 mm, other conditions as in Fig. 24.

which ringing usually interferes with analyte peaks does not appear in spectra of gel samples. Other interfering peaks (impurity with mass ~ 209 a.u.) are missing too. Some peaks can be assigned to other products of ionization of VNA. Most interfering ions, however, are formed because of direct photoionization of PA gel by 193-nm light and refinement of the optical setup should reduce this background. The detection limits are in the femtomole region for VNA.

The method was also used for sensitive detection of valin and several dipeptides in PA gels. However, the extension of the method on larger peptides and proteins was not successful. The 337-nm desorption step does not generate molecular ions or characteristic fragment ions of proteins like insulin. Also, the photodissociation of larger peptides or proteins may result in more different products and hence lower sensitivity. A 193-nm laser cannot be used as the desorption laser for MALDI because of extensive fragmentation of analyte.

193-nm Photodissociation of Insulin as a Tool for MALDI Investigation

Interaction of 193-nm light with insulin desorbed by MALDI does not yield analytically useful signals. MS peaks of fragment ions, such as decarboxylated aminoacids overlap with intense peaks of ions of the matrix and its fragments. Yet, the 193-nm photodissociation (PD) of insulin is highly efficient. Interaction of loosely focused 193-nm beam (power density ~ 10 MW/cm^2, beam dimensions, 1 x 4 mm, distance of the beam from sample, 1 mm, pulse-to-pulse delay 5 μs) with MALDI-generated plume of insulin resulted in virtually complete absence of insulin in the

mass spectrum. The elimination of the insulin peak from the spectra may also be attributed to space charge effects due to a large number of fragment ions generated by the photoionization of matrix and insulin. The phenomenon may be used to characterize plume properties. In this experiment, we focused the 193-nm laser beam to achieve minimal focal width in the direction of the plume movement (along the flight axis). It is essential to dissociate only a thin slice of plume to avoid space charge effects. Assuming energy distribution as the major contribution to the plume broadening, we increased the spot-to-spot distance to 5 mm and focused the beam to the width of ~ 100 μm. Intensity of extraction field was reduced to $8x10^4$ V/m (V_a=15.0 kV, V_b=14.0 kV) in order to minimize the overall axial velocity. Insulin ions produced at the probe surface were accelerated to the velocity of approximately $3.7x10^3$ m/s at the location of the 193-nm laser focal point. At this velocity, 10-ns pulsewidth of the 193-nm pulse resulted in an additional 37-μm spatial broadening. Nevertheless, we were able to observe a photodissociation of a fraction of insulin plume generated from its mixture with ferulic acid (1:1000). The upper trace in Fig. 28 shows insulin peak (M=5735 a.u., average of 20 traces) from mass spectra obtained by simple MALDI. Poor resolution (~20) originates mainly from an uneven power density over the desorption laser spot and from the low intensity of the extraction field. Unresolved adducts of higher mass represent less than 10 % of the peak area and neglecting them should not introduce serious error to our

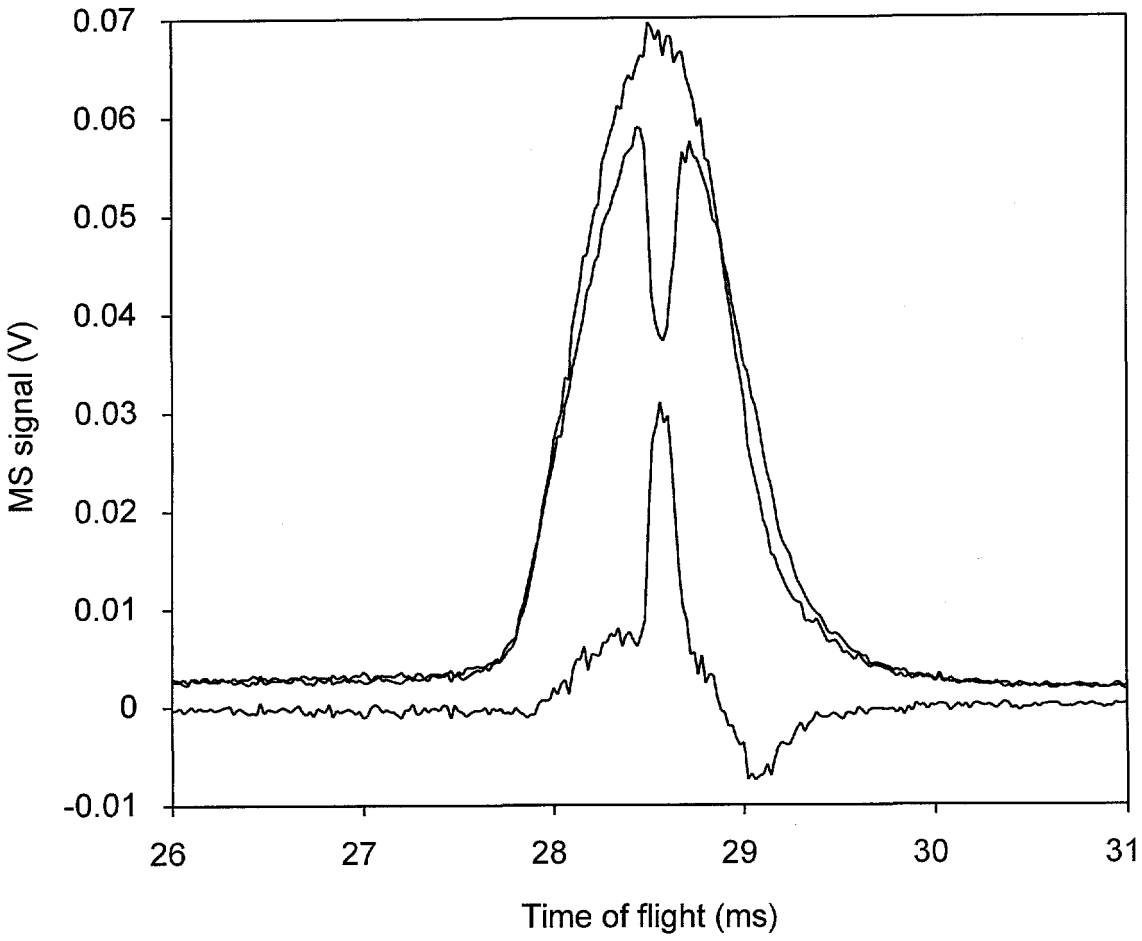

Figure 28. A portion of MALDI -TOF spectrum of insulin ion (5735 a.u.). Simple MALDI (top), MALDI/PD (middle), difference spectrum (bottom). The pulse-to-pulse delay was 2.8 μs. Other details in the text.

estimations. The middle trace in Fig. 28 shows the insulin peak generated from the same spot, but with 193-nm laser turned on. The negative "spike" represents the photodissociated portion of the insulin plume at the pulse-to-pulse delay of 2.8 μs. Not all insulin within the slice had to be decomposed. 193-nm laser energy fluctuated tremendously (±30 %) which resulted in the incomplete decomposition of the insulin within the focal boundaries. The axial dimension of the plume could be larger than the height of the focal region with sufficient power density. Spatial distribution and heavier adducts of insulin might also contribute to the fact the spike does not reach the baseline. The bottom trace in Fig. 28 was calculated as the difference of the two upper traces and it expresses the net photodissociated insulin. The strong variations in its baseline are due to gradual changes in the peak shape with an increasing number of pulses. In spite of these baseline variations, the difference spectrum gives better estimation of the spike position on the time-of-flight axis than the spiked mass spectrum. The observation of the narrow spike cannot be explained if we assume the velocity distribution as the only source of the broadening. In that case, the insulin ions with initial velocities between 1000 and 0 m/s would arrive at the 193-nm focal point at times from 2.1 to 2.7 μs and to the detector at the times from 27.5 to 28.2 μs. In our experiment, however, most insulin ions arrived at the 193-nm laser spot in 2.8 μs and at the detector in 28.5 μs. A series of experiments with variable pulse-to-pulse delay was carried out to examine this phenomenon in detail. A spike position on the time-of-flight axis was

determined from the difference spectra for each delay. The linear relationship between the spike time-of-flight and the pulse-to-pulse delay is characterized by the slope 1.04 ± 0.2 and r^2 0.995 (Fig. 29). This means the temporal profile of the plume was essentially the same at a distance of 5 mm from the desorption spot as at the detector. The temporal and spatial distribution of the insulin ions has to be considered. We expect the ions to be formed at several hundreds nanoseconds after the desorption shot above the surface. The value of the slope is slightly larger than 1 due to velocity or spatial broadening.

Knowledge of spatial, temporal and velocity profiles of ions generated by MALDI is important for ion-focusing and explanations of the reactions in gas. The design of most experiments cannot distinguish between the contribution of various broadening mechanisms. Energy broadening is commonly considered the dominant source of the peak width. The effects of the temporal spread in ion formation may also be reduced by time-lag extraction. The design of our experiment enables us to spike the plume shortly after its formation. Work is under progress to answer the questions about the location and the delay of ion formation.

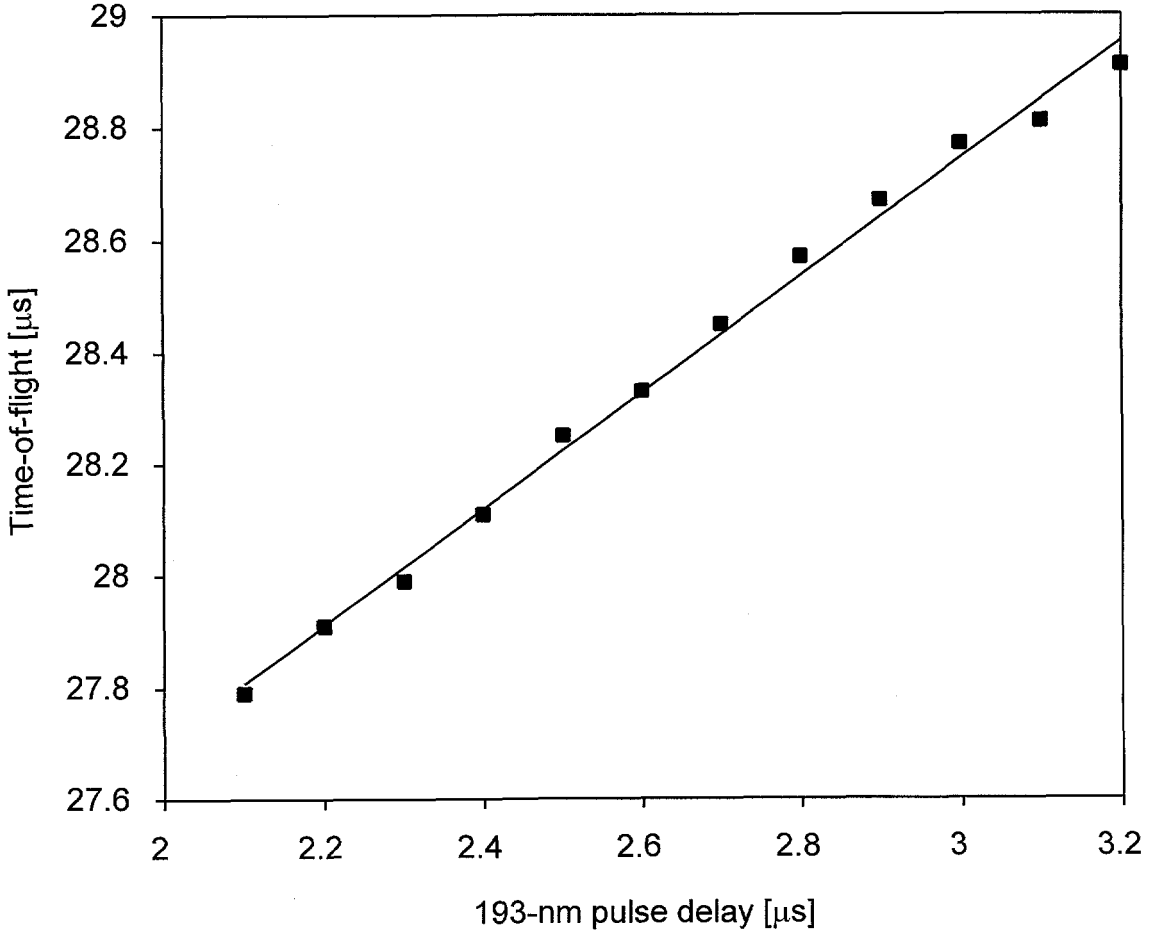

Figure 29. Position of the spike on the time-of-flight axis as a function of the pulse-to-pulse delay. The conditions are the same as in Fig. 28.

CHAPTER 6. SUMMARY

The conditions used in MALD experiments are different from the typical conditions employed in MALDI. The matrix-to-analyte ratio is at least an order lower than common ratios and the power levels at the desorption spot are approximately one order higher in comparison with usual power levels. These results defined the optimal conditions for desorbing analytes from matrices, as opposed to achieving a compromise between efficient desorption and efficient ionization as is practiced in mass spectrometry. The experiments were also carried out under atmospheric pressure. Although our experimental conditions are not standard for mass spectrometry, we believe the information is useful for further improvement of MALDI-MS, especially if one can implement post ionization to allow independent optimization of the vaporization and ionization steps. In addition, MALD may provide a means for observing unique optical spectra in large molecules.

In the absorbance imaging mode several interesting features were observed, e.g. differences between the initial plume and subsequent plumes desorbed from the same spot, or the formation of two plumes from one laser shot. A satisfactory correlation of the total plume absorbance with the acoustic signal generated by the desorption event was found. A model equation for the plume velocity as a function of time is proposed. The use of a static laser beam for observation enabled reliable

determination of plume velocities even when they were very high. Static scattering detection revealed negative influence of particle spallation on the MS signal.

Large enhancement of detection sensitivity and selectivity was shown on an example of 193 nm-photoionization combined with laser desorption of small molecules containing aminoacids. On the other hand, 193-nm light causes efficient photodissociation of proteins. The photodissociation of plumes of insulin ions enabled us to characterize the ion formation during MALDI. The position and the width of the insulin peak could not be explained by the initial velocity distribution of the ions. In addition to the velocity distribution of insulin ion, temporal and spatial spreads in ion formation were found to contribute to the broadening of MS peaks significantly.

PART 2.

CAPILLARY ELECTROPHORESIS

Portions of this dissertation part are reprinted with permission from:

Preisler, J., Yeung, E. S. *Anal. Chem.* 1996, 68, 2885-2889

CHAPTER 7. INTRODUCTION

Capillary electrophoresis (CE) in fused silica capillaries is now a popular separation method. The silica surface of the capillary shows numerous types of interactions with the solvent and the solutes, which may have a disastrous effect on the reproducibility and performance of CE. These may cause adsorption of analytes and hence peak broadening. The presence of acidic silanol groups and other charged species on the capillary walls is responsible for the phenomenon of electroosmotic flow (EOF) in silica capillaries.[137] EOF is often desirable because it enables the determination of cationic, neutral and anionic species in a single run and the nearly flat flow profile does not hinder separation efficiency. On the other hand, acid-base equilibration on the silica surface is very slow and exhibits pH hysteresis.[138] This, together with changes of the surface due to adsorption of species from the running buffer and the sample, results in reduced reproducibility. The presence of EOF is not always necessary and may even make some separations impossible. The undesirable effects of EOF may be overcome by coating the inner capillary wall. Examples of a number of coating materials and coating procedures have been reviewed in ref. 139.

In our group, PEO was successfully employed as a sieving matrix for DNA separation in a coated capillary,[140] and later in an uncoated capillary.[141] This inspired the use of PEO as a coating material for protein separation by CE.[139] The

coating seems to greatly reduce EOF due to surface charge on the silica surface and prevents adsorption of proteins on the capillary walls. The PEO molecules are held to the capillary walls only by weak interactions, such as van der Waals forces and hydrogen bonds. Hence, the coating may be easily removed to regenerate the original column surface in between runs. However, stability of the coating during electrophoresis is important for it to be functional.

One way to examine changes in the PEO coating is to monitor EOF in the capillary. The most common method is to calculate the EOF velocity from the migration time of an uncharged compound and the capillary length.[142] The disadvantage of this method is that it gives only a value of EOF averaged over a period of time. Running electrophoresis between two buffer solutions with somewhat different concentrations can also be used for EOF determination.[143] During the run, one of the buffer solutions replaces the other one in the capillary column and the time necessary to fill the entire capillary of known length is found from a change in the current (conductivity). Direct weighing of the electrolyte collected from the capillary outlet[144-146] can in principle be used for continuous EOF monitoring, but in practice the approach is limited by the sensitivity of the balance. A successful approach for real-time measurement of EOF is based on fluorescence detection of a dye which continuously adds to the solution in a buffer vial as the dye exits the separation column.[147] Utilization of a neutral marker and fluorescent imaging of a long portion of the capillary column[148, 149] forms the basis of this work. Simple excitation geometry

using lenses was preferred to utilization of fiber optic.[149] A CCD camera is used to monitor the movement of a fluorescent neutral marker zone in real time. This static imaging setup is more convenient than a spatially scanned fluorescence detection system.[150-153] The usefulness of EOF monitoring will be demonstrated as applied to the optimization of the coating procedure and to the investigation of the experimental conditions necessary for coating stability.

CHAPTER 8. EXPERIMENTAL

Chemicals

The chemicals for solution preparation and capillary conditioning were obtained from several sources: hydrochloric acid, sodium hydroxide and sodium phosphate monobasic from Fisher Scientific (Fair Lawn, NJ); tris-(hydroxymethyl)-aminomethane (TRIS) and ethylenediaminetetraacetic acid (EDTA) from ICN Biomedicals (Aurora, OH); boric acid from Sigma Chemical (St. Louis, MO); and PEO with MW = 8,000,000 from Aldrich Chemical (Milwaukee, WI). The phosphate buffer solutions were prepared by dissolving sodium phosphate monobasic in approximately 470 mL water, adjusting the pH by adding HCl or NaOH, and adding water to 500 mL. The ionic strength of all phosphate buffers was 50 mM. The TBE buffer (1×) was prepared by simple addition of TRIS, boric acid and EDTA in water without any pH adjustment. The concentrations of the first two components in the buffer were 89 mM, the concentration of EDTA was 2 mM, and the measured pH was 8.2. Coumarin 334 from Eastman Kodak (Rochester, NY) was dissolved initially in methanol; the concentration of the stock solution was 2×10^{-3} M. Sample solutions of coumarin 334 were prepared by 100-fold dilution of the stock solution with the desired running buffer. A stock solution of PEO was prepared by gradual addition (in less than 1 min) of 0.1 g of the polymer to 45 mL water in an Erlenmeyer flask. The water was vigorously mixed by stirring and heated to 40-50 ^{o}C. After the

addition of PEO, the flask was sealed and heated at approximately 80 ^{o}C for at least 15 min. This solution was used for up to two weeks. Neutral or acidified 0.2% PEO solutions were prepared by the addition of 0.5 mL of water or 1 M HCl to 4.5 mL of PEO stock solution. The acidified gel was used for at most two days after the addition of acid. Although no change in analytical performance was observed within two weeks, the acidified gel became less viscous over that period. This is probably a result of formation of shorter-chain polymers due to the acid hydrolysis of PEO.

Electrophoresis Setup

A high-voltage power supply (Spellman, Model UHR50PN150/CR/MTP) was used to drive the electrophoresis at 10.5 kV. A fused silica capillary obtained from Polymicro Technologies (Phoenix, AZ) was placed into an aluminum holder. Two pieces of Teflon tube were used for electrical isolation. The outer protective coating of the entire capillary was burnt off in a flame and remnants of the coating were removed with a paper tissue soaked in methanol. The coating was removed with a slack capillary in the holder; it was tightened after coating removal. No capillary (350 μm o.d., 75 μm i.d.) was damaged during the process. The total length of the capillary was 55 cm. 0.5-mL and 1.5-mL microvials served as the cathodic (detection-end) and anodic (injection-end) buffer reservoirs, respectively. The small dimensions of the injection-end vial allowed us to reduce the distance of the injection end from the imaged portion of the capillary to 2.0 cm. The distance

between the cathodic end and the capillary holder was long enough to allow lowering of the cathodic reservoir for hydrodynamic injection at a 10-cm height difference. For the verification of coumarin 334 as a neutral marker, a commercial instrument with an absorption detector was used (SPECTRAPHORESIS 100, Spectra Physics, San Jose, CA).

Optical Setup

A 488-nm, 200-mW argon-ion laser beam (Laser Ionics, Orlando, FL, Model 554A) was expanded in the horizontal direction by cylindrical planoconvex lenses (25 mm f.l.) to excite a 232-mm portion of the capillary (Fig. 30). A CCD camera (Spectra Source Instruments, Westlake Village, CA, Model MCD 1000) in connection with a 19-mm f.l. camera lens (Vivitar, Japan, f/3.8) and a 525-nm long-pass filter was used to image the excited portion of the capillary (Fig. 31). The dimensions of the image of the excited capillary portion filled with a fluorescing compound were 578 × 1 pixel. A mechanical shutter (Melles Griot, Boulder, CO, Model 04 IES 003) was synchronized with the internal (CCD) shutter using a modified signal from the camera controller. The excitation time was approximately 0.8 s and the exposure time (limited by the inner shutter) was 1.0 s. The external shutter prevented photodissociation of the dye molecules under continuous laser irradiation because intervals between exposures ranged from 1 to 5 min. The optical system was not optimized for the best detection sensitivity. Because a laser

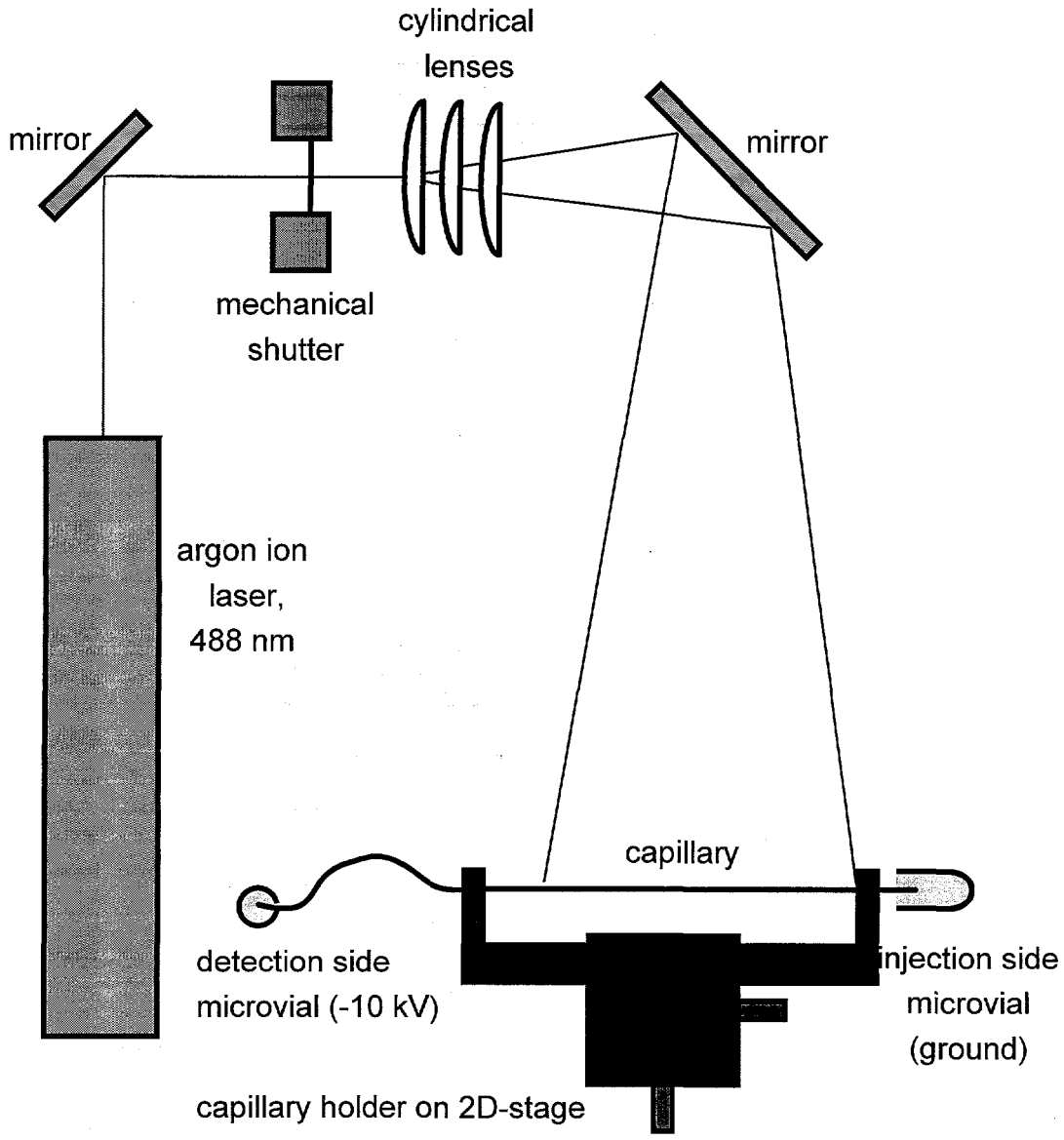

Figure 30. Experimental setup for continuous monitoring of EOF (top view).

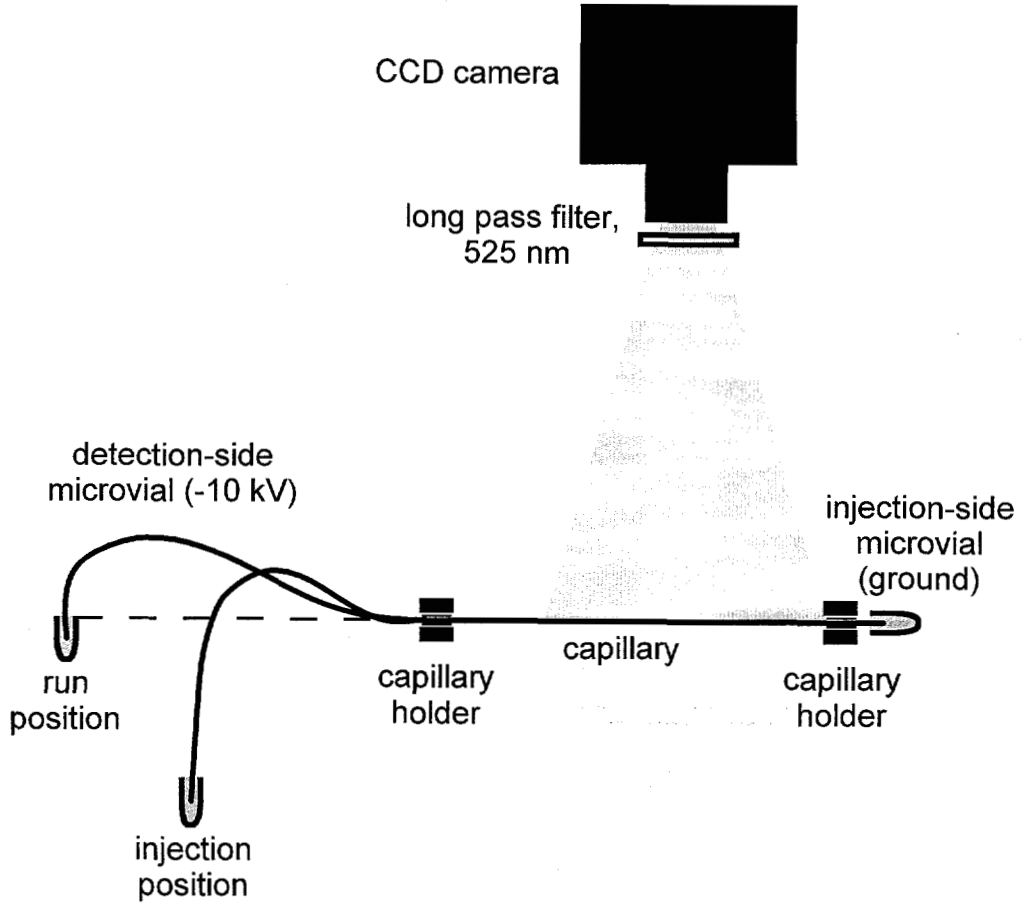

Figure 31. Experimental setup for continuous monitoring of EOF (side view)

with relatively high power was available, the power density at the capillary was high enough without further focusing in the vertical dimension by another cylindrical lens.

Capillary Wall Treatment

If one capillary is to be used for many experiments, we have to restore the column surface to its original state after every run.[139, 141] First, the PEO coating from the preceding experiment was removed by flushing (if not mentioned otherwise, pressure flushing is employed) the capillary with 1 M HCl for at least 30 min and 0.1 M NaOH for at least 15 min. These rather long reaction times with both acidic and alkaline solutions were used because treatment with only one of the solutions or for shorter periods did not yield reproducible results. Then, the column was flushed with the running buffer for 2 min and the extent of regeneration of the column surface can be verified by the determination of EOF.

Second, the wall of the capillary was coated by flushing with 0.2% PEO solution for 5 min. Alternatively, this step could be preceded by column pretreatment with 1 M HCl for 5 min. After the coating step, the capillary was flushed with running buffer for 2 min. A zone of 2×10^{-5} M coumarin 334 solution was injected (5-s hydrodynamic injection at 10-cm height difference) and transported (90 s at 10-cm height difference) to the edge of the imaged region. High voltage was then applied and the location of the zone inside the capillary as a function of time was followed by the CCD camera.

Velocity Determination

The first image was taken 5 min after the initial contact with the running buffer. The capillary was imaged at intervals of 1 to 5 min while the zone was in the imaged region. More frequent exposures could have introduced problems due to photobleaching of the dye. The average velocity was calculated from the consecutive positions of the zone over the time interval between two exposures. The interaction time in the figures was determined from the first contact of the running buffer with the capillary.

CHAPTER 9. RESULTS AND DISCUSSION

Neutral Marker Selection

We can assume the utility of a PEO coating on the reduction of EOF lies at high pH values, where the magnitude of EOF in a bare fused-silica capillary is relatively high. Also, the typical buffer used for DNA sequencing by CE[141] has a pH value of 8.2. In order to carry out experiments at these pH of interest, we chose coumarin 334 as a neutral marker. This selection was verified by comparison of electropherograms (absorption detection) of coumarin 334 itself, its mixture with mesityl oxide, and mesityl oxide alone in phosphate buffers with pH = 7.0 and pH = 8.2. Coumarin 334 is sufficiently soluble, its adsorption on the capillary wall is negligible, and its fluorescence is easily excited by 488-nm radiation from an Ar-ion laser.

Coating Protocols

Before flushing the capillary with a PEO solution, the capillary walls can be left untreated or can be pretreated with 1 M HCl solution for 5 min. PEO itself can be used as prepared (neutral solution) or acidified (in 0.1 M HCl). This results in four different coating procedures. The various coating protocols were evaluated by monitoring EOF in phosphate buffers with pH of 7.0, 7.7 and 8.2. Differences between these were most apparent at pH 7.7 (Fig. 32). Direct coating with acidified

PEO solution without any pretreatment (Fig. 32c) gave the best results, i.e., the smallest electroosmotic mobility, μ_{EO}, and the best temporal stability. Direct coating with neutral PEO solution (Fig. 32d) was not as effective in reducing EOF. Even there, the EOF was reduced to approximately 30% of its value in an untreated silica capillary. For acidic pretreatment followed by coating with acidified PEO solution (Fig. 32a), the EOF was also suppressed effectively, but there was a gradual deterioration of the coating with time. Apparently, a highly protonated silica surface is less favorable for forming strong bonds with PEO molecules. In the last case (Fig. 32b), coating with neutral PEO solution after acidic pretreatment did not produce a stable coating. Those three independent experiments showed large variations in both the initial magnitude of EOF and its temporal stability. This probably reflects different extents of hydration and protonation of the silica surface after the pretreatment step. All four coating protocols were also tested at pH = 7.0 and 8.2. At those pH, differences among the initial magnitude of EOF and its temporary stability as a result of the coating protocols were less evident. However, we found that flushing with acidified PEO solution always created a better coating.

pH Dependence

Fig. 33 shows the temporal development of EOF at different buffer pH. Each of the curves is the average from three experiments. The coating was prepared using the best protocol as determined above, i.e., flushing with an acidified solution

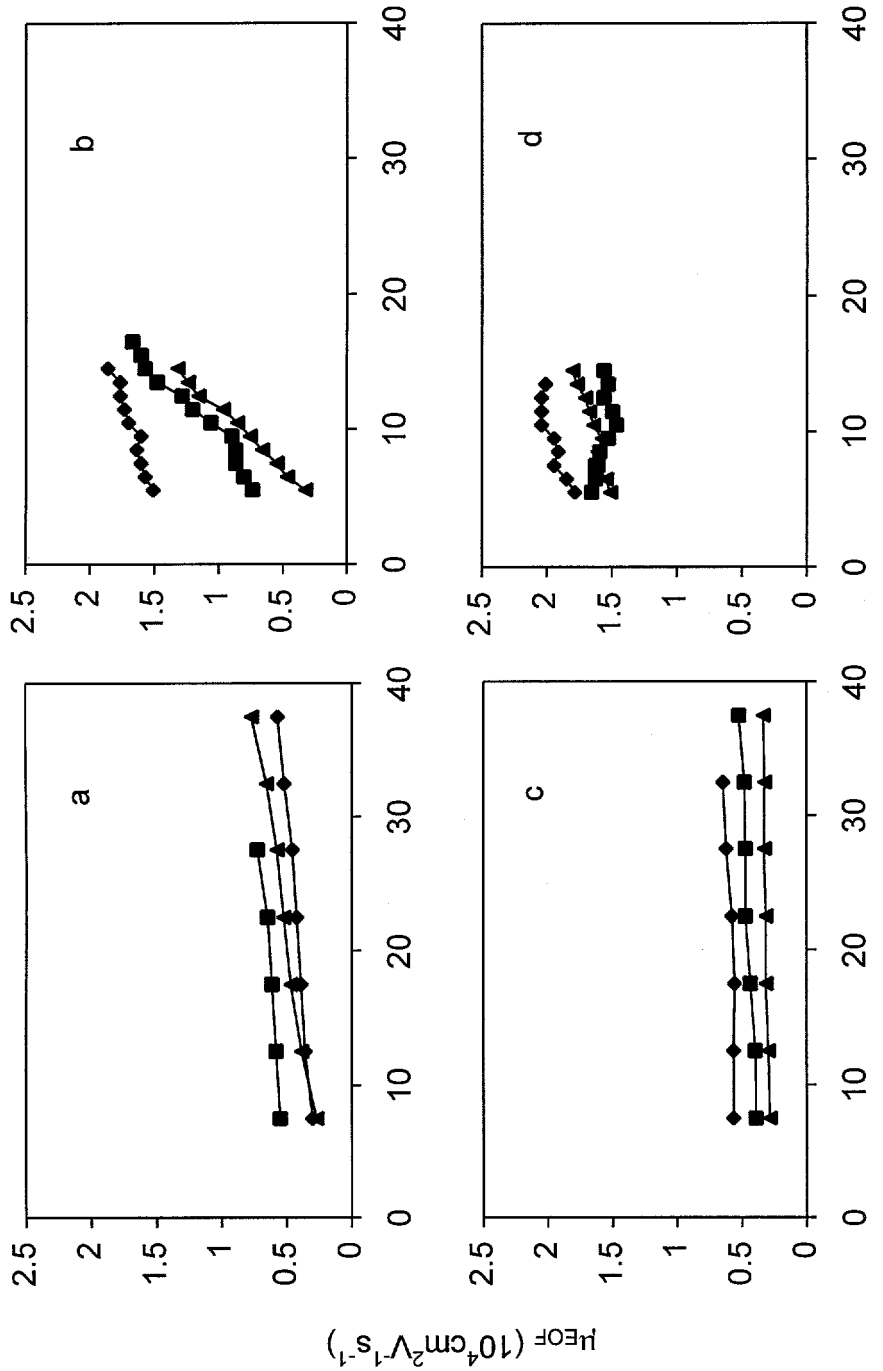

Figure 32. Comparison of coating protocols at pH = 7.7: acidified PEO solution with acidified column pretreatment (a), neutral PEO solution with acidified column pretreatment (b), acidified PEO solution with no column pretreatment (c), and neutral PEO solution with no column pretreatment (d).

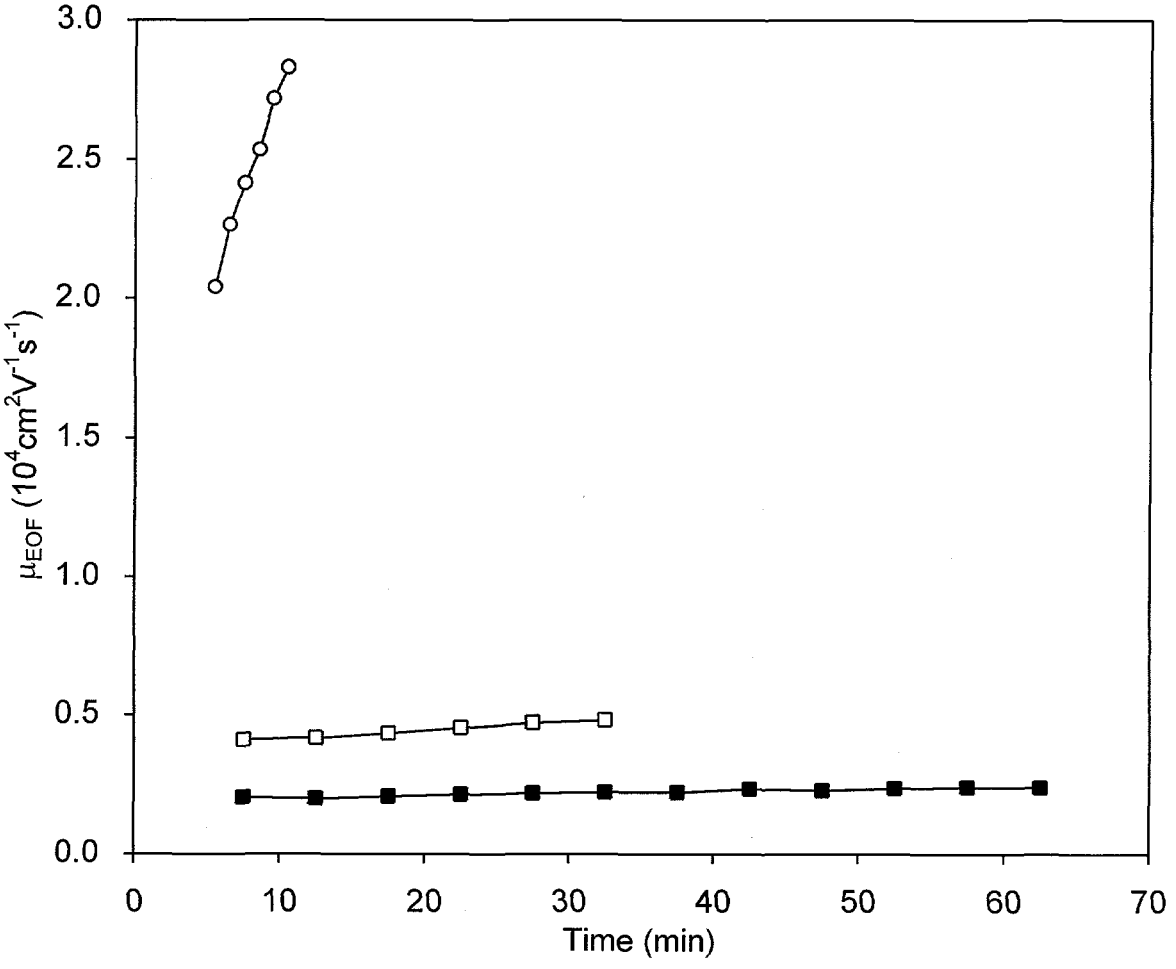

Figure 33. Temporal development of electroosmotic mobility at pH 7.0 ■, 7.7 □, and 8.2 O. For comparison, μ_{EO} in a bare capillary are (4.3 ± 0.3) × 10^{-4} cm^2 V^{-1} s^{-1}, (5.4 ± 0.2) × 10^{-4} cm^2 V^{-1} s^{-1}, and (6.4 ± 0.3) × 10^{-4} cm^2 V^{-1} s^{-1}, respectively. Each graph represents an average of three experiments. The coating was prepared by pressure flush with acidified PEO solution without any column pretreatment (c in Fig. 32).

of PEO without any column pretreatment. The values of electroosmotic mobilities in bare silica capillaries at each pH value are given in the figure caption. At pH = 7.0, the PEO coating resulted in a decrease of EOF by more than one order of magnitude, regardless of which protocol was used for its preparation. The extent of reduction of the EOF by PEO coating at pH 7.7 strongly depends on the way the coating was prepared, as mentioned above. At pH 8.2, EOF was reduced to only 30-50% of that in a bare silica capillary, which is not analytically useful. When the PEO coating was exposed to phosphate buffer at pH 8.2, the EOF increased immediately and continued to increase. Consecutive flush with 1 M HCl for 30 min and then with phosphate buffer at pH = 7.0 did not reduce the EOF noticeably. This means that the running buffer at pH > 8 causes instant removal of the PEO coating. Similar behavior was observed when borate instead of phosphate was used as the buffer ion, confirming that this is purely a pH effect. The pH of typical DNA sequencing buffer is 8.2. Although one has to have in mind that PEO was used only as a coating and not as a matrix in our case, our findings suggest that the commonly used pH value may not be optimal for PEO utilization and that a change in buffer pH may be considered. The viscous sieving matrix slows down the degradation of the "coating" in sequencing applications.[5]

Long Term Stability

The volume of the running buffer in both the cathodic and the anodic reservoirs was increased to 50 mL to prevent major changes of pH during this experiment. The PEO coating showed excellent long-term stability if a critical pH was not exceeded. The magnitude of EOF at pH 7.7 (phosphate buffer) increased by only 10% after 24 h of continuous electrophoresis. This slight increase might also be due to temperature, because the current showed a similar increase during the course of the experiment. So a non-bonded PEO coating at pH 7.7 can suppress EOF in CE by almost an order of magnitude over an extended period. This indicates the probable reason of the PEO coating removal from the silica surface of the capillary is competitive hydrogen bond formation among silanol group, hydroxide anion and PEO.

Critical pH.

When the capacity of the buffer solutions is not sufficient, there occurs an abrupt increase of EOF as a result of pH increase. Fig. 34 depicts the stability of the PEO coating for three different volumes of running buffer present at the detection end (cathodic). During these experiments, a new neutral marker zone had to be reinjected occasionally in order to enable measurement of EOF for an extended period of time. Change of pH in the anodic reservoir was minimized by making the injection-end reservoir large (50 mL of running buffer). Hydroxide anions

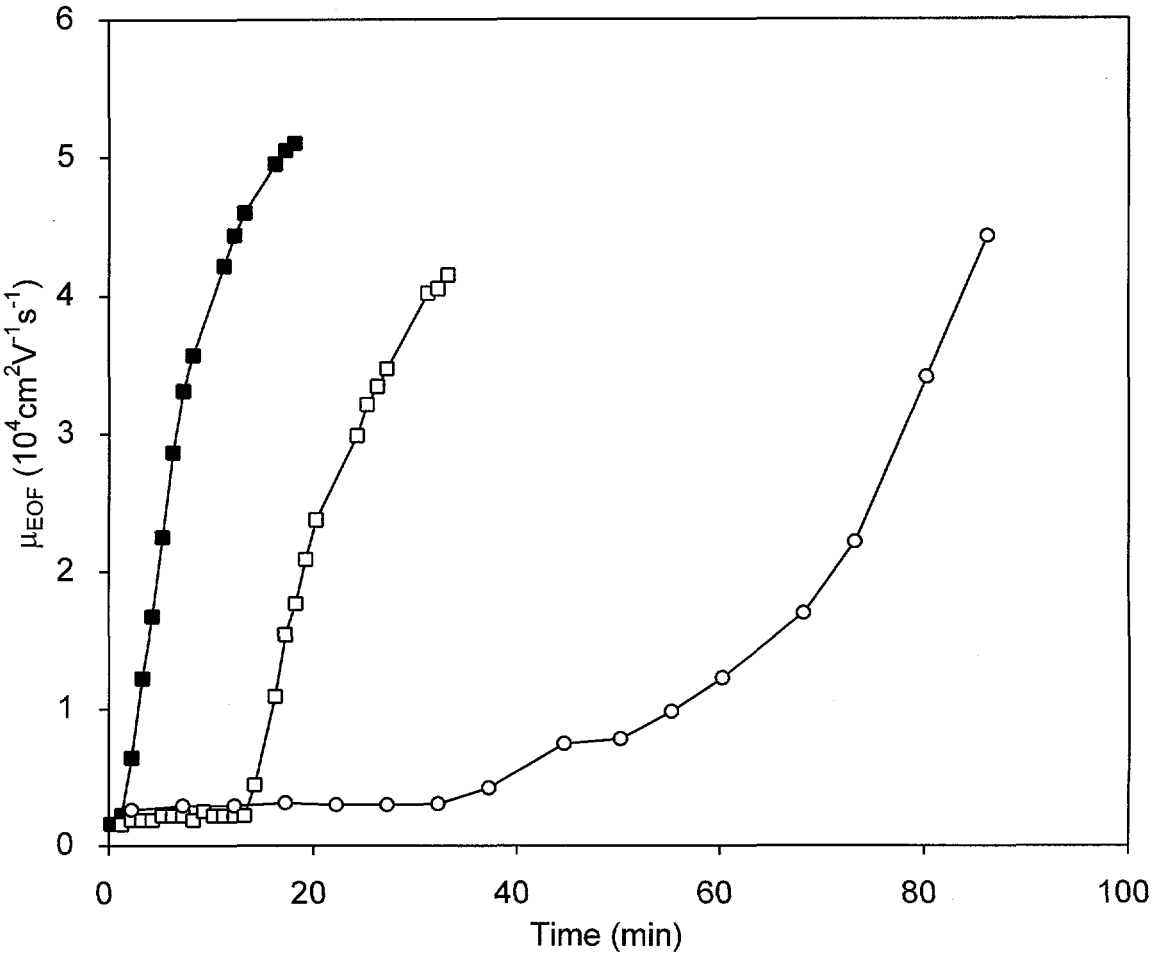

Figure 34. Temporal development of electroosmotic mobility as a result of electrolysis in the cathodic buffer reservoir. Original pH of the running buffer, 7.7. Volume of the buffer solution in the cathodic reservoir: 0.1 mL, ■; 0.2 mL,□; and 0.5 mL, O. The coating was prepared by pressure flush with acidified PEO solution without any column pretreatment (c in Fig. 32).

produced at the cathode during an electrophoresis run are responsible for the pH increase in the buffer vial at the detection end. The phosphate and hydroxide anions then migrate into the capillary, causing a gradual increase of pH inside the capillary. Once a critical value of pH is passed, the coating will be removed and EOF will increase. For a small volume of running buffer, the critical pH change is achieved in a short time. One can calculate from the buffer capacity and Faraday's constant that the steep increase in EOF corresponds to pH 8.0 in the detection-end reservoir in each case in Fig. 34.

Hydroxide anions are produced on the entire immersed surface of the cathode, causing an increase in HPO_4^{2-} at the expense of $H_2PO_4^-$. Because the phosphate anions are the main current carriers and because HPO_4^{2-} moves faster, the pH inside the capillary can become higher than the average pH in the cathodic reservoir. The fast increase of pH inside the capillary is especially prominent if the capillary inlet is close to the electrode, i.e., the capillary inlet reaches into the diffusion layer around the electrode. The diffusion layer (0.5 mm thick) is formed within several minutes and the migration of anions into the capillary is further enhanced by the electric field. In our experiments, we did not fix the distance of the capillary inlet from the cathode and the cathodic solution was not stirred. The calculations of the critical pH are therefore only approximate, as it is not common to do so in routine capillary electrophoresis. The relation between the buffer capacity and the time EOF begins to increase is clear. So is the importance of better control

over the position of the electrode and cathodic end of the capillary. More precise study of the phenomena was not done since the removal of PEO coating is a very complex procedure. It may vary considerably as a result of the original capillary condition, coating technique, and gel quality. Change of pH inside the capillary as a result of cathodic reaction can in principle be monitored directly from the shift in fluorescence wavelength of a probe ion.[154]

Electrophoretic Coating Removal

Although early on we found that a pressure flush for 5 min with only NaOH solution is sufficient for PEO coating removal, we flushed the separation capillary with 1 M HCl and then 0.1 M NaOH solutions throughout the entire work. The reason was we did not achieve reproducible results after the single washing step with NaOH solution. As we found out later, the reason was insufficient flow rate during the flush. An alternative way to remove the PEO coating after a run is to replace the running buffer at the detection end with 0.1 M NaOH solution and apply high voltage. Within 5 min of electrophoresis, the pH inside the capillary increases above the critical value and the PEO coating is removed completely. The electrical current increased from 30-35 to 100-120 μA during this cleaning step. This procedure for electrophoretic column regeneration was followed by a 2-min flush with the running buffer. The restoration of EOF can be verified. The electrophoretic regeneration procedure was found to be more reliable and easier to carry out. The

movement of a solution during pressure flush follows the well-known parabolic velocity profile across the capillary, while the movement during electrophoretic flush is characterized by an essentially flat profile. The migration of hydroxide ions and other charged species next to the column surface is therefore faster, leading to rapid restoration of the original fused-silica surface.

CHAPTER 10. SUMMARY

Temporal changes in EOF in CE are related to the stability of the column surface over the course of electrophoresis. On-column fluorescence imaging provides a direct measurement of the instantaneous EOF velocity in a non-intrusive manner. This approach was used successfully to characterize poly(ethylene oxide) as a non-bonded coating in CE. With the correct protocol, PEO can reduce EOF by more than an order of magnitude at pH = 7.7 over an extended period of time. Rapid regeneration of the column surface was possible by electrophoretic removal of the coating after each run.

GENERAL CONCLUSIONS

This work demonstrated numerous applications of lasers in analytical chemistry. Lasers are used for desorption, photoionization or as the light sources for absorbance, fluorescence and scattering detection. The ability of pulse lasers to generate high power within a short interval is essential for desorption and photoionization methods. Monochromaticity of the laser beam is the key to selectivity of RMPI. Or, in case of the system for continuous imaging of a capillary, it simplifies the optical setup substantially. All methods take advantage of the coherent nature of lasers. A laser beam can be focused to a desired shape in a convenient distance from the laser. The quality of laser beams is of the same importance as their power.

This work also deals with different ways of imaging. Imaging is based on scanning the laser beam with acousto-optic deflector(s) or using a CCD camera. Determination of temporal plume evolution or evaluation of time delay in LD-MPRI are in fact imaging methods too.

The advancement of laser techniques is fast and continual. Further escalation may be expected especially with improving the laser beam quality and development of tunable (especially in VUV region) or ultrashort-pulse lasers.

APPENDIX A. ELECTRONIC CONTROLLER CIRCUIT

FOR TIMING OF SINGLE SHOT EXPERIMENT

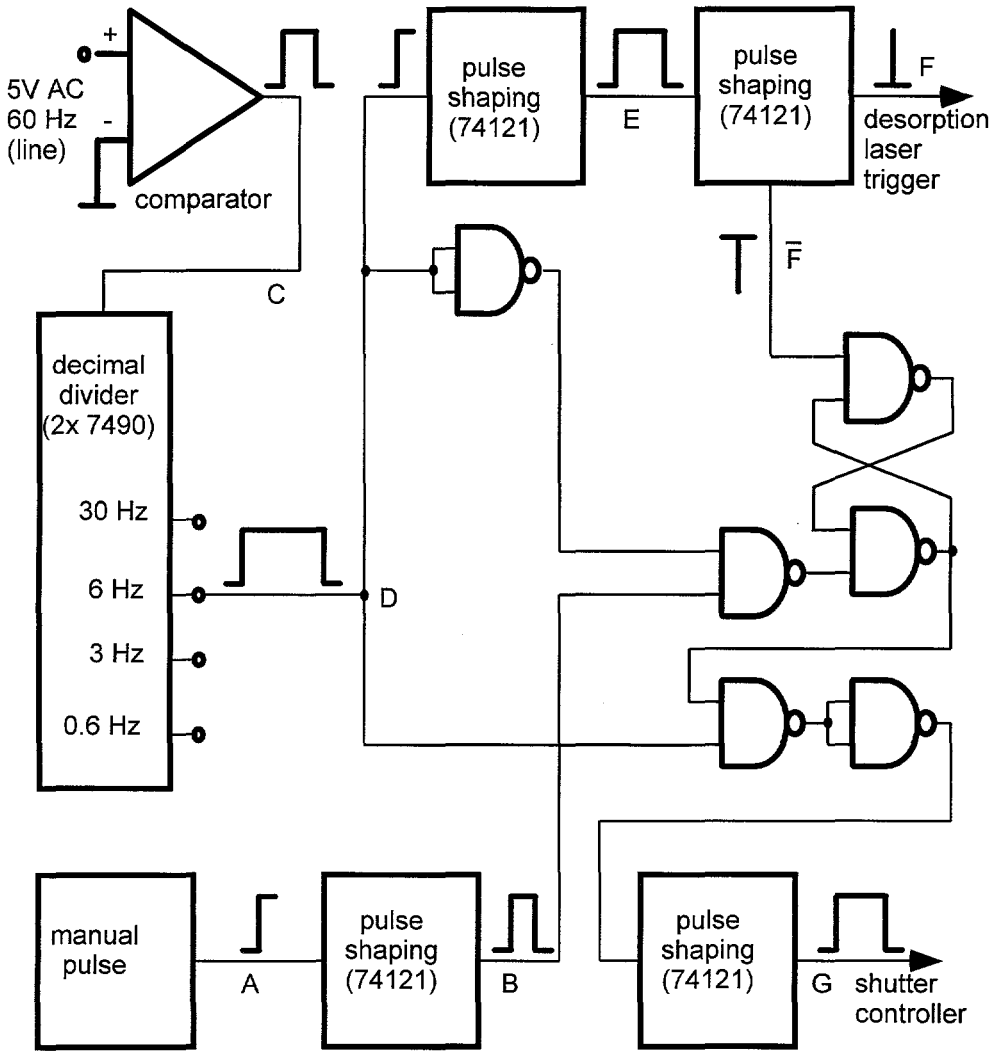

Block diagram of the circuit for triggering of the desorption laser.

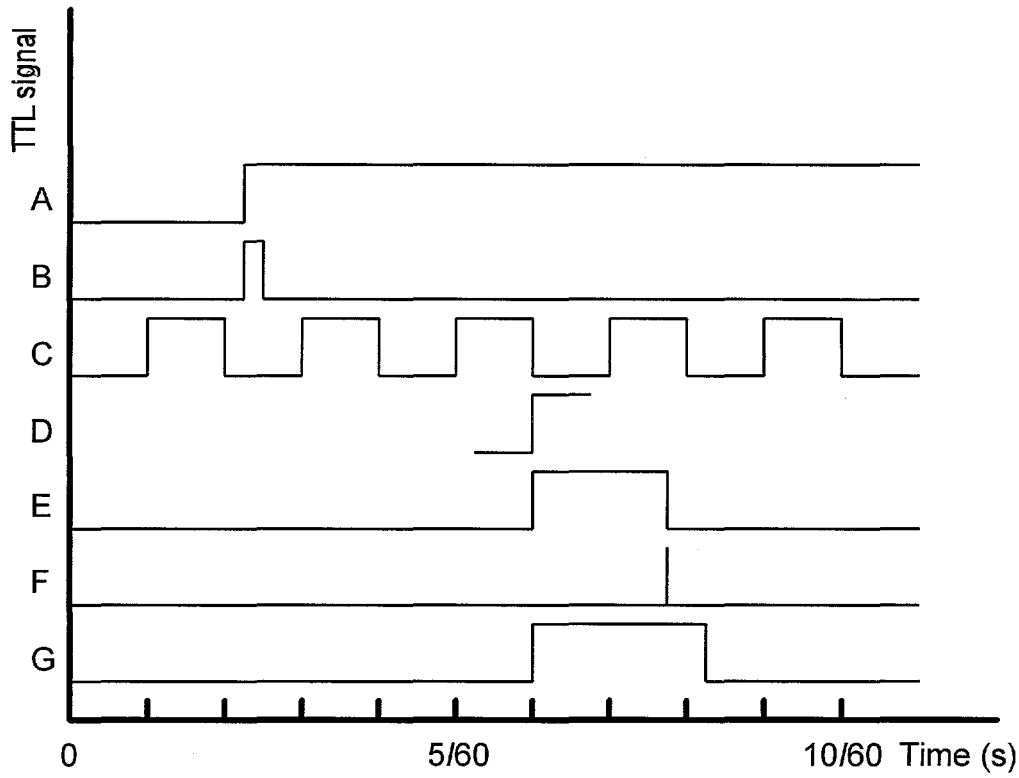

Timing diagram for the desorption laser trigger. The letters at the traces correspond to specifics point in the circuit on the previous page.

APPENDIX B. DATA PROCESSING FOR 2D-IMAGING

In order to handle large amounts of data, a batch file ONEPLUME.BAT was written to carry out multiple operations from the translation of the original binary file to displaying or printing of a topographic 10-image picture. This appendix contains explanation of filename convention, a batch file ONEPLUME.BAT and its explanation, and the Turbo Pascal source code of the key program FASTCUT.EXE.

Filename Convention

Three files are recorded for one desorption event:

MMDD##E contains up to 10,000 values of photocurrent difference, ΔI

MMDD##F contains up to 10,000 values of reference photocurrent, I_o

MMDD##R contains up to 10,000 values from referent photodiode; maxima correspond to scanning beam in the top position

MMDD stands for date, ## for the number of run. The original files from LeCroy (e.g. SC1.###) are easily renamed by program NEWNAME.EXE. File extensions are used to specify the type of data file:

no extension binary data file from LeCroy

PRN one-column ASCII data file

DAT three-column (x,y, absorbance) ASCII data file of one image

GRD grid file of SURFER GRID program

PLT plot file of SURFER TOPO program

The file MMDD##V.PRN contains up to 10,000 values of absorbance calculated from MMDD##E.PRN and MMDD##F.PRN files. The last figure (#) in MMDD### files (*.DAT, *GRD, *.PLT) means the number of image taken (1-10).

ONEPLUME.BAT

```
cls
@echo off
echo This file makes *.grd and topo-picture files (10 frames,
single desorption).
echo Uses SURFER configuration files g.cmd and t.cmd.
echo.
c:
cd \jan\bin

rem BINAS3.EXE translates binary files (*)into ASCII files
rem (*.PRN)
Translating binary file %1R to ASCII file %1R.PRN
binas3 %1R
echo Translating binary file %1E to ASCII file %1E.PRN
binas3 %1E
echo Translating binary file %1F to ASCII file %1F.PRN
binas3 %1F
copy %1?.PRN \jan\data\%1?.PRN
del %1?.PRN
cd \jan\data
cls

rem ABSCALC3.EXE calculate absorbance from %1E.PRN and %1F.PRN
rem files and store it as %1V.PRN file.
abscalc %1

rem FASTCUT.EXE cuts the data file %1V.PRN to 10 "xyz" single-
rem frame files %1#for SURFER.
fastcut %1
del %1?.PRN
```

```
rem SURFER's GRID makes grid files %1#.GRD from %1#.DAT.
\surfer\grid /cmd=papg /action=randomgrid %11
\surfer\grid /cmd=papg /action=randomgrid %12
\surfer\grid /cmd=papg /action=randomgrid %13
\surfer\grid /cmd=papg /action=randomgrid %14
\surfer\grid /cmd=papg /action=randomgrid %15
\surfer\grid /cmd=papg /action=randomgrid %16
\surfer\grid /cmd=papg /action=randomgrid %17
\surfer\grid /cmd=papg /action=randomgrid %18
\surfer\grid /cmd=papg /action=randomgrid %19
\surfer\grid /cmd=papg /action=randomgrid %110
del %1*.dat

rem SURFER's TOPO makes a 10-frame topographic image of a
plume rem desorption.
\surfer\topo /cmd=papt /inname=%11 /titstr=1 /outname=%1.plt
/pagepos=0.7,4.5 /action=plot
\surfer\topo /cmd=papt /inname=%12 /titstr=2 /outname=%1.plt
/pagepos=3.3,4.5 /outmode=a /action=plot
\surfer\topo /cmd=papt /inname=%13 /titstr=3 /outname=%1.plt
/pagepos=5.9,4.5 /outmode=a /action=plot
\surfer\topo /cmd=papt /inname=%14 /titstr=4 /outname=%1.plt
/pagepos=8.5,4.5 /outmode=a /action=plot
\surfer\topo /cmd=papt /inname=%15 /titstr=5 /outname=%1.plt
/pagepos=11.1,4.5 /outmode=a /action=plot
\surfer\topo /cmd=papt /inname=%16 /titstr=6 /outname=%1.plt
/pagepos=0.7,1 /outmode=a /action=plot
\surfer\topo /cmd=papt /inname=%17 /titstr=7 /outname=%1.plt
/pagepos=3.3,1 /outmode=a /action=plot
\surfer\topo /cmd=papt /inname=%18 /titstr=8 /outname=%1.plt
/pagepos=5.9,1 /outmode=a /action=plot
\surfer\topo /cmd=papt /inname=%19 /titstr=9 /outname=%1.plt
/pagepos=8.5,1 /outmode=a /action=plot
\surfer\topo /cmd=papt /inname=%110 /titstr=10 /outname=%1.plt
/pagepos=11.1,1 /outmode=a /action=plot
del %1*.grd

rem SURFER's VIEW displays the image on screen.
\surfer\view %1
```

Source Program FASTCUT.PAS

```
Program FASTCUT;

USES CRT;

Var
  INFILE,OUTFILE: Text;
{Files}
  FBASE,FINFILE,FILEOUT: String[25];
{Filenames}
  V,W,X,Y,Z,TR,TRMV,MAX,MIN: Real;
{Consecutive data points, treashold, max, min}
  ARR: Array [1..10010] Of Real;
{Array of file data points}
  I,J,K,L,M,N,Q,R,TOTPEAK,NUMBER,TOTFRAM,POINTS,DIST: Integer;
{Variables for loops and arrays}
  SHIFT: Integer;
  PEAK: Array [1..1000] Of Integer;
{Position of peak max in ref file}
  FRAME: Array [1..300] Of Integer;
{Position of the first frame-peak in PEAK array}
  FLAG, FFF: Boolean;
{Parameters}
  SUFFIX: String[2];
{The number of output file}
  TRPASLIK: Char;
{Parameters}

Procedure Filename; {Read files, finds minimum and maximum}

Begin
Writeln;
Writeln('Reading file ',FINFILE);
Writeln;
Assign(INFILE,FINFILE);
Reset(INFILE);
NUMBER:=0;
While Not Eof(INFILE) Do
  Begin
  NUMBER:=NUMBER+1;
  Readln(INFILE,ARR[NUMBER]);
  If Pos('V.PRN',FINFILE)=0 Then
```

```
    Begin
    If NUMBER=1 Then
      Begin                    {Find max and min values of files}
      MAX:=ARR[1];
      MIN:=ARR[1];
      End;
    If (ARR[NUMBER]>=MAX) And (NUMBER>100) Then     {Peak top}
      MAX:=ARR[NUMBER];{beginning due to vaporiz. laser pulse}
    If ARR[NUMBER]<=MIN Then
      MIN:=ARR[NUMBER];
    End;
  End;
ClrScr;
End;

{Main program}
Begin
{Read the base of filenames from thecommand line}
FBASE:=ParamStr(1);
ClrScr;
WriteLn;
WriteLn('   FAST VERSION OF CUTABS1');
WriteLn;
{Writeln('  Program cuts input data file into several output
files according to');
Writeln('   referent file. New files can be imported to SURFER
or QUATTRO.');
Writeln;
Writeln('   Referent file: *R.PRN, data file: *V.PRN, output
files: *1.DAT, *2.DAT etc.');
Writeln('   Syntax of command line: CUT7 *  , where * is the
base of input filenames');
Writeln;
Writeln('   Treashold for determination of peaks is
automatically calculated');
Writeln('   as one half between max and min data points of
referent file.');
Writeln('   "Number of points" has to be higher than the
number of data points between');
Writeln('   two peaks in one frame but lower than the number
of data points between');
Writeln('   the last peak of one frame and the first peak of
the next frame. The ');
```

```
Writeln('   default value is the average number of points
between two neighbor peaks.');
Writeln('   The first peak IS automatically first frame
too.');
Writeln;
Writeln('   The extra change: real x and y values - in mm (for
889 mm scan region).');
Writeln('   Format of output files:');
Writeln('   X-column: height, Y-column: width, Z-column:
absorbance data for [X,Y]');}

{If the base of the filenames is omitted, then ask for it.}
If FBASE='' Then
  Begin
  Writeln('   The base of input ASCII filenames may be
specified on command line !');
  WriteLn;
  Write('Input the base of filename now: ');
  ReadLn(FBASE);
  End;

FINFILE:=FBASE+'R.PRN';
Filename;
TRPASLIK:='N';
TR:=MIN+(MAX-MIN)/2;                          {Default treshold}

{Find the "number of data points".}
TOTPEAK:=0;
V:=0; W:=TR; X:=0; Y:=0; Z:=0;
  For L:=1 To NUMBER Do
    Begin
    Z:=ARR[L];
    If (X>TR) Then
{Top of peak?}
      Begin
      If ((X>V) And (X>=W) And (X>Y) And (Y>Z)) Then
        Begin
        TOTPEAK:=TOTPEAK+1;
        PEAK[TOTPEAK]:=L-2;
        I:=0;
        End;
      End;
    V:=W; W:=X; X:=Y; Y:=Z;
```

```
    End;
  POINTS:=ROUND((PEAK[TOTPEAK]-PEAK[1])/TOTPEAK+1);
{Default number of points}

  WriteLn;                          {Find the beginnings of frames.}
  FLAG:=False;
  TOTPEAK:=0; I:=0; TOTFRAM:=0;
  V:=0; W:=TR; X:=0; Y:=0; Z:=0;
  For L:=1 To NUMBER Do
    Begin
    Z:=ARR[L];
    If (X>TR) Then
{Top of peak?}
      Begin
      If ((X>V) And (X>=W) And (X>Y) And (Y>Z)) Then
        Begin
        TOTPEAK:=TOTPEAK+1;
        PEAK[TOTPEAK]:=L-2;
        If ((FLAG=True)Or(TOTPEAK=1)) Then
{...this peak is the first in frame.}
          Begin
          TOTFRAM:=TOTFRAM+1;
          FRAME[TOTFRAM]:=TOTPEAK;
          End;
        FLAG:=False;
        End;
        I:=0;           {Correct nulling after a top of peak.}
      End;
    V:=W; W:=X; X:=Y; Y:=Z;
    If Z<TR Then                    {I...points below treashold}
      Begin
      I:=I+1;
      If I=POINTS Then
      FLAG:=True;
      End;
    End;

{ Show the results of determination of frames.}
  Writeln;
  For Q:=1 To TOTFRAM Do
  Writeln('#',Q,' frame at ',PEAK[FRAME[Q]]);
  Writeln;
  Writeln('Number of frames =      ',TOTFRAM);
```

```
  Writeln('Number of peaks =       ',TOTPEAK);
  Writeln('Number of data points = ',NUMBER);

{Checking parameters, comparison with the last results}
  If TRPASLIK='Y'Then
    Begin
    Writeln;
    If (J=TOTPEAK) And (K=TOTFRAM) Then
      Writeln('O.K., change of factors has no influence on
frames.')
    Else
      Writeln('Frames have been changed since the last change
of parameters !!!');
    End;
  Writeln;
  If (POINTS>(PEAK[FRAME[1]+1]-PEAK[FRAME[1]]+1)) And
(POINTS<(PEAK[FRAME[1]+2]-PEAK[FRAME[1]]-10)) Then
    Writeln('The number of frames is reasonable.')
  Else
    Writeln('Number of frames may be determined badly!');
  Writeln;


{Number of data points between the neighbor peaks inside
frames}
Y:=0;
For Q:=2 To TOTFRAM-1 Do
{For all frames except the first & last one}
  Begin
  For R:=FRAME[Q] To (FRAME[Q+1]-2) Do
    Begin
    X:=PEAK[R+1]-PEAK[R];
    Y:=Y+X;
    End;
  End;
DIST:=ROUND(Y/(FRAME[3]-FRAME[2]-1)/(TOTFRAM-2));


{Number of data points that should be "inserted" on the
beginning of the referent file will be suggested (SHIFT)}

If TOTFRAM >=9 Then
  Begin
```

```
  WriteLn('Shift of 8 data points is proposed for file of
',TOTFRAM,' frames.');
  SHIFT := 8;
  End
Else
  Begin
  If TOTFRAM >= 4 Then
    Begin
    WriteLn('Shift of 18 data points is proposed for file of
',TOTFRAM,' frames.');
    SHIFT := 18
    End
  Else
    Begin
    WriteLn('Shift of 36 data points is proposed for file of
',TOTFRAM,' frames.');
    SHIFT := 36;
    End;
  End;
WriteLn;

{The data file will be read.}
FINFILE:=FBASE+'V.PRN';
Filename;

{Files for each frame will be formed.}
Writeln;
Q:=0; PEAK[TOTPEAK+1]:=11111; FRAME[TOTFRAM+1]:=TOTPEAK+1;
Repeat
{Frame File}
  J:=0; Q:=Q+1;
  Str(Q,SUFFIX);
  FILEOUT:=FBASE+SUFFIX+'.DAT';
  Assign(OUTFILE,FILEOUT);
  Rewrite(OUTFILE);
  While J<DIST Do
    Begin
    I:=0;
    While ((FRAME[Q]+I)<(FRAME[Q+1])) Do
{One line}
      Begin
```

```
      If (((PEAK[FRAME[Q]+I]+J-
DIST+SHIFT)<=NUMBER)And((PEAK[FRAME[Q]+I]+J-DIST+1+SHIFT)>0))
Then
        Writeln(OUTFILE,(I*8/18):5:3,' ',(J*9/49):5:3,'
',(ARR[PEAK[FRAME[Q]+I]+J-DIST+1+SHIFT]):9:7)
      Else
        Writeln(OUTFILE,(I*8/18):5:3,' ',(J*9/49):5:3);
      I:=I+1;
      End;
    J:=J+1;
    End;
  Writeln('Saving ',FILEOUT,'.');
  Close(OUTFILE);
Until Q=TOTFRAM;
End.
```

REFERENCES

1. Einstein, A. *Physikalische Zeitschrift* **1917**, *18*, 121.
2. Purcell, E. M. and Pound, R. V. *Phys. Rev.* **1951**, *81*, 279.
3. Maiman, T. H. *Nature* **1960**, *187*, 493.
4. Beckey, H. D. *Int. J. Mass Spectrom. Ion. Phys.* **1969**, *12*, 500.
5. Vastola, F. J. and Pirone, A. J. *Adv. Mass Spectrom.* **1970**, *4*, 107.
6. Torgenson, D. F., Skowronski, R. P. and Macfarlane, R. D. *Biochem. Biophys. Res. Commun.* **1974**, *60*, 616.
7. Benninghoven, A. and Sichterrmann, W. *Org. Mass Spectrom.* **1977**, *12*, 500.
8. Grade, H., Winograd, N. and Cooks, R. G. *J. Am. Chem. Soc.* **1977**, *99*, 7725.
9. Blakely, C. R., Carmody, J. J. and Vestal, M. L. *J. Am. Chem. Soc.* **1980**, *102*, 5931.
10. Barber, M., Bordoll, R. S., Sedgwick, R. D. and Tayler, A. N. *J. Chem. Soc., Chem. Commun.* **1981**, 325.
11. Yamshita, M. and Fenn, J. B. *J. Phys. Chem.* **1984**, *88*, 4451.
12. M. Karas, D. Bachmann, U. Bahr and F. Hillenkamp *Int. J. Mass Spectrom., Ion Proc.* **1987**, *78*, 53.
13. Bruce, J. E., Cheng, X., Bakhtiar, R., Wu, Q., Hofstadler, S. A., Anderson, G. A. and Smith, R. D. *J. Am. Chem. Soc.* **1994**, *116*, 7839.
14. Smith R.D., Udseth, H.R., Barinaga, C.J. and Edmonds, C.G. *J. Chromtogr.* **1991**, *559,* 197.

15. Lee, E.D., Mück, N.M., Henion, J.D. and Covey, T.R. *Biomed. Environ. Massc x Spectrom.* **1989**, *18*, 844.

16. Posthumus, M. A., Kistemaker, P. G., Meuzelaar, H. L. C., Ten Noever de Brauw, M. C., *Anal. Chem.* **1978**, *50*, 985.

17. Karas, M., Bachmann, D. and Hillenkamp, F. *Anal. Chem.* **1985**, 57, 2935.

18. Hillenkamp, F., Karas, M., Holtkamp, D. and Klusener,P. *Int. J. Mass Spectrom. Ion Process.* **1986**, *69*, 265.

19. Tanaka, K. Waki H., Ido, Y., Akita, S., Yoshikazu, Y. and Yashida, T. *Rapid Commun. Mass Spectrom.* **1988**, *8*, 151.

20. Hillenkamp, F., Karas, M., Beavis, R. and Chait, B. T. *Anal. Chem.* **1991**, *63*, 1193A.

21. Karas, M., Bahr, U. and Gieβmann, U. *Mass Spectrom. Rev.***1991**, *10*, 335.

22. Ehring, H., Karas, M. and Hillenkamp, F. *Org. Mass Spectrom.*, **1992**, *27*, 472.

23. Spengler, B. and Kaufmann, R. *Analusis* **1992**, *20*, 91.

24. Kinsel, G. R., Preston, L. M. and Russel, D. H. *Biol. Mass Spectrom.* **1994**, *23*, 205.

25. Beavis, R. C. and Chait, B. T. *Rapid Commun. Mass Spectrom.* **1989**, *3*, 233.

26. Fitzgerald, M. C., Parr, G. R. and Smith, L. M. *Anal. Chem.* **1993**, *65*, 3204.

27. Beavis, R. C. and Chait, B. T. *Rapid Commun. Mass Spectrom.* **1989**, *3*, 432.

28. Beavis, R. C. and Chait, B. T. *Rapid Commun. Mass Spectrom.* **1989**, *3*, 436.

29. Karas, M., Bahr, U, Ingendoh, A., Nordhoff, E., Stahl, B., Strupat, K. and Hillenkamp, F. *Anal. Chim. Acta* **1990**, *241*, 175.

30. Tang, K., Alman, S. L. and Chen, C. H., *Rapid Commun. Mass Spectrom.* **1993**, *7*, 943.

31. Nelson, R. W., Thomas, R. M. and Williams, P. *Rapid Commun. Mass Spectrom*. **1990**, *4*, 348.

32. Tang, K., Alman, S. L., Chen, C. H., Chang, L. Y. and Schell, M. *Rapid Commun. Mass Spectrom.* **1994**, *8*, 183.

33. Cornett, D. S., Duncan, M. A. and Amster, I. J. *Org. Mass. Spectrom.* **1992**, *27*, 831.

34. Gusev, A. I., Wilkinson, W. R., Proctor, A. and Hercules, D. M. *Anal. Chem.* **1995** *67*, 1034.

35. Preston, L. M., Murray, K. K. and Russel, D. H. *Biol. Mass Spectrom.* **1993**, *22*, 544.

36. Vorm, O., Roepstorff, P. and Mann, M. *Anal. Chem.* **1994**, *66*, 3281.

37. Cohen, S. L. and Chait, B. T. *Anal. Chem.*, **1996**, *68*, 31.

38. Beavis, R. C. and Chait, B. T. *Anal. Chem.* **1990**, *62*, 1836.

39. Juhasz, P., Roskey, m. T., Smirnov, I. P., Haff, L. A., Vestal, M. L. and Martin, S. A. *Anal. Chem.* **1996**, *68*, 941.

40. Chait, B. T., wang, R., Beavis, R. C. and Kent S. B. H. *Science* **1993**, *262*, 89.

41. Linder, B. and Seydel, U. *Anal. Chem.* **1985**, *58*, 895.

42. Fain, B. and. Lin, S. H. *J. Chem. Phys.* **1989**, *91*, 2726.

43. Johnson, R. E. and Sundquist, B. U. R. *Rapid Commun. Mass Spectrom.* **1991**, *5*, 574.

44. Sundquist, B. U. R. *Int. J. Mass Spectrom, Ion Proc.* **1992**, *118/119*, 265.

45. Westman, A., Huth-Fehre, T., Demirev, P., Bielawski, J., Medina, N. and Sundquist, B. U. R. *Rapid Commun. Mass Spectrom.* **1994**, *8*, 388.

46. Srinivasan, R. and Branen, B. *Chem. Rev.* **1989**, *89*, 1303.

47. Vertes, A., Gijbels, R. and Levine, R. D. *Rapid Commun. Mass Spectrom.* 1990, *4*, 228.

48. Vertes, A. and Levine, R. D. *Chem. Phys. Letters* **1990**, *171*, 284.

49. Vertes, A., Irinyj, G. and Gijbels, R. *Anal. Chem.* **1993**, *65*, 2389.

50. Zare, R. N. and Levine, R. D. *Chem. Phys. Letters* **1987**, *136*, 593.

51. Zhang, J.-Y., Nagra, D. S. and Li, L. *Anal. Chem.* **1993**, *65*, 2812.

52. Johnson, R. E. *Int. J. Mass Spectrom., Ion Processes* **1994**, *139*, 25.

53. Speir, J. P. and Amster, I. J. *Anal. Chem.* **1992**, *64*, 1041.

54. Beavis, R. C. and Chait, B. T. *Chem. Phys. Letters* 1991, *181*, 479.

55. Pan, Y. and Cotter, R. J. *Org. Mass Spectrom.* **1992**, *27*, 3.

56. Spengler, B. and Cotter, R. J. *Anal. Chem.* **1990**, 62, 793.

57. Ens, W., Mao, F., Mayer F. and Standing, K. G. *Rapid Commun. Mass Spectrom.* **1991**, *5*, 117.

58. Zhou, J., Ens, W., Standing, K. G. and Verentchikov, A. *Rapid Commun. Mass Spectrom.* **1992**, *6*, 671.

59. Spengler, B., Karas, M., Bahr, U. and Hillenkamp, F. *J. Phys. Chem.* **1987**, *91*, 6502.

60. Conzemius, R. J. and Capellan, J. M. *Int. J. Mass Spectro. Ion Phys.* **1980**, *34*, 197.

61. Hillenkamp, F., In *Ion Formation from Organic Solids II*, Benninghoven A., Ed., Springer-Verlag: New York, **1983**, pp. 190-205

62. Smith, C. J., Cheng, Y.-C. and Yeung, E. S. *J. Mass Spectrom* **1995**, *30*, 1765.

63. Wang., B. H., Dreisewerd, K., Bahr, U., Karas, M. and Hillenkamp, F. *J. Am. Soc. Mass Spectrom.* **1993**, *4*, 393.

64. Winograd, N. *Anal. Chem.* **1993**, *65*, 622A..

65. Benninghoven, A., Hagenhoff, B. and Niehuis, A. *Anal. Chem.* **1993**, *65*, 630A.

66. Lubman, D. *Anal. Chem.* **1987**, *59*, 31A.

67. Zhang, J.-Y., Nagra, D. and Li, L. *Anal. Chem.* **1993**, *65*, 2812.

68. Engelke, F., Hahn, J. H., Henke, W. and Zare, R. *Anal. Chem.* **1987**, *59*, 909.

69. Watson, C. H., Gokhan, B. and Eyler, J. R. *Anal. Chem.* **1987**, *59*, 1133.

70. Williams, E. R., Furlong, J. J. and McLafferty, F. W. *J. Am. Soc. Mass Spectrom.* **1990**, *1*, 288.

71. Ayre, C. R., Moro, L. and Becker, C. H. *Anal. Chem.* **1994**, *66*, 1610.

72. Hrubowchak, D. M., Ervin, M. H., Wood, M. C. and Winograd, N. *Anal. Chem.* **1991**, *63*, 1947.

73. Ervin, M. H., Wood, M. C. and Winograd, N. *Anal. Chem.* **1993**, *65*, 417.

74. Terhorst, M., Kampwerth, G., Niehuis, E. and Benninghoven, A. In *Proceedings of the Eight International Conference On Secondary Ion Mass* Spectrometry, Benninghoven, A., Janssen, K. T. F., Tunpner, J. and Werner, H. W., Ed., Wiley: New York, **1992**, pp. 567-570.

75. Mollers, E.,Terhorst, M., Niehuis, E. and Benninghoven, A. *Org. Mass Spectrom.* **1992**, *27*, 1393.

76. Terhorst, M., Kampwerth, G., Niehuis, E. and Benninghoven, A. *J. Vac. Sci. Technol. A* **1992**, *10*, 3210.

77. Pallix, J. B., Schuhle, U., Becker, C. H. and Huestis, D. L. *Anal. Chem.* **1989**, *61*, 805.

78. Grotemeyer, J., Boesl, U., Walter, K. and Schlag, E. W. *Org. Mass Spectrom.* **1986**, *21*, 595.

79. Grotemeyer, J., Boesl, U., Walter, K. and Schlag, E. W. *Org. Mass Spectrom.* **1986**, *21*, 645.

80. Tembreull, R. and Lubman, D. *Anal. Chem.* **1987**, *59*, 1082.

81. Li, L. and Lubman, D. M. *Anal. Chem.* **1988**, *60*, 1409.

82. Tembreull, R. and Lubman, D. *Anal. Chem.* **1987**, *59*, 1003.

83. Li, L. and Lubman, D. M. *Anal. Chem.* **1989**, *61*, 1911.

84. Dale, M. J., Jones, A. C., Pollard, S. J. T., Langridge-Smith, P. R. R. and Rowley, A. G. *Environ. Sci. Technol.* **1993**, *27*, 1963.

85. Dale, M. J., Jones, A. C., Langridge-Smith, P. R. R., Costello, K. F. and Cummins, P. G. *Anal. Chem.* **1993**, *65*, 793.

86. Wang, A. P. L. and Li, L. *Anal. Chem.* **1992**, *64*, 769.

87. Zare, R. N. and Levine, R. D. *Chem. Phys. Lett.* **1987**, *136*, 593.

88. Slifkin, M. A. and Allison, A. C. *Nature* **1967**, *215*, 949.

89. Nikogosyan, D. N. and Gorner, H. *J. Photochem. Photobiol. B* **1992**, *13*, 219.

90. Candeias, L. P. and Steenken, S. *J. Am. Chem. Soc.* **1992**, *114*, 699.

91. Spengler, B., Karas, M. and Hillenkamp, F. *J. Phys. Chem.* **1987**, *91*, 6502.

92. Speir, J. P., Gorman, G. S., Cornett, S. D. and Amster, J. I. *Anal. Chem.* **1991**, *63*, 65.

93. Bowers, W. D., Delbert, S.-S. and McIver, Jr., R. T. *Anal. Chem.* **1986**, *58*, 972.

94. Hunt, D. F., Shabanowitz, J. and Yates III, J. R. *J. Chem. Soc., Chem. Commun.* **1987**, 548.

95. Hunt, D. F., Shabanowitz, J., Yates III, J. R., Griffin, P. R. and Zhu, N.-Z. *Anal. Chim. Acta* **1989**, *225*, 1.

96. Dunn, J. M. In *New Directions in Electrophoretic Methods*, Jorgenson, J. W., Phillips, M., Ed., ACS Symposium Series 335, ACS: Washington, **1987**, pp. 20-32.

97. Maizel, J. V. Jr. *Science*, **1966**, *151*, 988.

98. Ogorzalek, R. R., Stevenson, T. I., Mitchell, C., Loo, J. A. and Andrews, P. C. *Anal. Chem.* **1996**, *68*, 1910.

99. Hall, S. C., Smith, D. M., Masiarz, F. R., Soo, V. M., Tran, H. M., Epstein, L. B. and Burlingame, A. L. *Proc. Natl. Ac. Sci. U.S.A.* **1993**, *90*, 1927.

100. Daga, A., Micol, V., Hess, D., Aebersold, R. and Attardi, G. *J. Biol. Chem.* **1993**, *268*, 8123.

101. Eckerskorn, C., Strupat, K., Karas, M., Hillenkamp, F. and Lottspeich, F. *Electrophoresis* **1992**, *13*, 664.

102. Castro, J. A., Koster, C. and Wilkins, C. *Rapid Commun. Masss Spectrom.* **1992**, *6*, 239.

103. Annan, R. S., Kochling, H. J., Hill, J. A. and Biemann, K. *Rapid Commun. Mass. Spectrom.* **1992**, *27*, 831.

104. Doroshenko, V. M., Cornish, T. J. and Cotter, R. J. *Rapid Commun. Mass Spectrom.* **1992**, *6*, 753.

105. Lee, H. and Lubman, D. *Anal. Chem.* **1995**, *67*, 1400.

106. Wiley, W.C. and McLaren, I.H. *Rev. Sci. Instrum.* **1955**, *26*, 1150.

107. Spengler, B., Kirsch, D., Kaufmann, R., Karas, M., Hillenkamp, F. and Giessmann, U. *Rapid Commun. Mass Spectrom.* **1990**, *4*, 301.

108. Imrie, D. C., Pentney, J. M. and Cottrell, J. S. *Rapid Commun. Mass Spectrom.* **1995**, *9*, 1293.

109. Brown, R.S. and Gilfrich, N.L. *Rapid Commun. Mass Spectrom.* **1992**, *6*, 690.

110. Nogar, N. S., Estler, R. C. and Miller, C. M. *Anal. Chem.* **1985**, *57*, 2441.

111. Hansen, S. G. *J. Appl. Phys.* **1989**, *66*, 3329.

112. Opsal, R. B., Owens, K. G. and Reilly, J. P. *Anal. Chem.* **1985**, *57*, 1884.

113. Kinsel, G., Grundwuerner, J. M. and Grotemeyer, J. *J. Am. Soc. Mass Spectrom.* **1993**, *4*, 2.

114. Mamyrin. B. A., Karataev, V. I., Shmikk, D. V. and Zagulin, V. A. *Sov. Phys. - JETP* **1973**, *37*, 45.

115. Boesl, R. B., Neusser, H. J., Weinkauff, R. and Schlag, E. W. *J. Phys. Chem.* **1982**, *86*, 4857.

116. Boesl, U., Weinkauf, R. and Schlag, E. W. *Int. J. Mass Spectrom. Ion Proc.* **1991**, *112*, 121.

117. Brown, R. S. and Lennon, J. J. *Anal. Chem.* **1995**, *67*, 1998.

118. Whittal, R. M. and Li, L. *Anal. Chem.* **1995**, *67*, 1950.

119. Colby, S. M., King, T. B. and Reilly, J. P. *Rapid Commun. Mass Spectrom.* **1994**, *6*, 865.

120. Koster, K., Lindner, J., Kinsel, G. K. andGrotemeyer, J. *Lect. Notes Phys.* 1991, *389*, 139.

121. Riahi, K., Bolbach, G., Brunot, A., Breton, F., Spiro, M. and Blais, J.-C. *Rapid Commun. Mass Spectrom.* **1994**, *8*, 242.

122. Dreisewerd, K., Schurenberg, M., Karas, M. and Hillenkamp, F. *Int. J. Mass Spectrom, Ion Proc.* **1994**, *141*, 127.

123. Steenhoek, L. E. and Yeung, E. S. *Anal. Chem.* 1981, *53*, 528.

124. Huie, C. W. and Yeung, E. S. *Spectrochim. Acta* **1985**, *40B*, 1255.

125. Kimbrell, S. and Yeung, E. S. *Appl. Spectrosc.* **1990**, *44*, 1218.

126. Heise, T. W. and Yeung, E. S. *Anal. Chem.* **1992**, *64*, 2175.

127. Heise, T. W. and Yeung, E. S. *Anal. Chem.* **1994**, *66*, 355.

128. Brillouin, L. *Ann. Phys. (Paris)* **1922**, *17*, 88.

129. Tran, C. D. *Anal. Chem.* **1992**, *64*, 971A.

130. Lekavich, J. *Lasers & Appl.* **1986**, *4*, 59.

131. Dickson, L. D. *Appl. Opt.* **1972**, *11*, 2196.

132. Haller, K. L. and Hobbs, P. C. D. In *SPIE Proceedings Vol.1435*, Fearey, B. L., Ed., SPIE, Bellingham: Washington, **1991**, pp. 298-309.

133. Rosenzweig, Z. and Yeung, E. S. *Appl. Spectrosc.* **1993**, *47*, 1175.

134. Xue, Y. and Yeung, E. S. *Anal. Chem.* **1993**, **65**, 1988.

135. Chen and E. S. Yeung, *Anal. Chem.* **1988**, *60*, 2258.

136. Heise, T. W. and Yeung, E. S. *Anal. Chim. Acta* **1995**, *299*, 377.

137. Jorgenson, J. W., Lukacs, K. D. *Anal. Chem.* **1981**, *53*, 1298.

138. Lambert, W. J., Middleton, D. L. *Anal. Chem.* **1990**, *62*, 1585.

139. Nobuhiko, I.; Yeung., E. S., *J. Chromatogr.* **1996**, *731*, 273.

140. Chang, H.-T.; Yeung, E. S. *J. Chromatogr. B* **1995**, *669*, 113.

141. Fung, E. N.; Yeung, E. S. *Anal. Chem.* **1995**, *67*, 1913.

142. Walbroehl, Y., Jorgenson, J. W. *Anal. Chem.* **1986**, *58*, 479.

143. Huang, X., Gordon, M. J., Zare, R. N. *Anal. Chem.* **1988**, *60*, 1837.

144. Altria, K. D., Simpson, *C. F. Anal. Proc.* **1986**, *23*, 453 .

145. Wanders, B. J., Van De Goor, A. A. A. M., Everaerts, F. M. *J. Chromatogr.* **1989**, *470*, 89.

146. Van De Goor, A. A. A. M., Wanders, B. J., Everaerts, F. M. *J. Chromatogr.* **1989**, 470, 95.

147. Lee, T. T., Dadoo, R., Zare, R. N. *Anal. Chem.* **1994**, 66, 2694.

148. Nilsson, S., Johansson J., Mecklenburg, M., Birnbaum, S., Svanberg, S., Wahlund, K.-G., Mosbad, K., Miyabayashi A., Larsson, P.-O. *J. Cap. Elec.* **1995**, 46.

149. Wu, X.-Z., Wu, J., Pawliszyn, J. *Electrophoresis* **1995**, 16, 1474.

150. Wu, J., Pawliszyn, J. *Am. Lab.* **1994**, 26 [15], 48.

151. Clark, B. C., Vo-Dinh, T., Sepaniak M. J. *Anal. Chem.* **1995**, 67, 680.

152. Beale, S. C., Sudmeier, S. J. *Anal. Chem.* **1995**, *67*, 3367 .

153. Clark, B. K., Sepaniak, M. J. *J. Microcol. Sep.* **1995**, 7(6), 593.

154. Timperman, A. T., Oldenburg, K. E., Sweedler, J. V., "Utilization of Fluorescence Spectral Information in CE" in 8th International Symposium on HPCE, Orlando, FL, 1996 (poster 519).

ACKNOWLEDGMENT

First of all, I would like to thank Professor Ed Yeung for his benevolent guidance through my work. I sincerely admire him for his enthusiasm, diligence and dedication to research. I have learned a lot and I am in his debt.

I am grateful to my committee members, Drs. R. S. Houk, J. S. Fritz, C.-Y. Ng, C. S. Swift and D. C. Johnson for their precious time and advice during my stay here.

All members of our group deserves thanks for their frequent help and advices. I also enjoyed this country, its natural beauties and friendly people. Special thanks to the authors of the Simpsons comics.

I would like to thank all my friends I left at home. Their humor is incredibly infectious and healing at the same time. I enjoy every moment we spend together. I also remember my relatives. And I definitely do not forget Monika, whose love made my last years in Ames much more exciting.

Finally, I want to thank my parents and my brother. They were always the first I asked for help and they have always helped me. I hope I will get a chance to repay them for all their support.

This work was performed at Ames Laboratory under Contract No. W-7405-Eng-82 with U.S. Department of Energy. The United States government has assigned the DOE Report number IS-T 1800 to this thesis.